

Chapter 3

The Deep Underground Neutrino Experiment

The Deep Underground Neutrino Experiment (DUNE) experiment [66, 88–90] is a future long-baseline neutrino experiment with a diverse physics program hosted by Fermilab, IL, U.S.. The far detector will be at the Sanford Underground Research Facility (SURF) near Lead, South Dakota, providing a baseline of 1300 km. A cartoon of the experiment is shown in Figure 3.1.

The DUNE experiment will be discussed in this present chapter. As the experiment utilises liquid argon TPCs, a brief history and description of this detector technology is provided as a basis in Section 3.1. An overview of the experiment, including its motivation, will be presented in Section 3.2 before the experimental details are discussed in Section 3.3. The sensitivities of the experiment and its potential discoveries are the subject of Section 3.4. Finally, the schedule and strategy implemented by the collaboration to ensure commencement of data taking in around ten years’ time is outlined in Section 3.5.

3.1 The LAr TPC Concept

The use of a liquid argon (LAr) Time Projection Chamber (TPC), or LArTPC, as a high-precision fine-grained detector medium holds much promise for the successful resolution of the open questions in neutrino physics. A great amount of R&D work has taken place to advance the maturity of the technology and pioneering experiments, such as ICARUS [91], have further increased the understanding of the neutrino community of the detector techniques. Past and currently running experiments at Fermilab, such as ArgoNeuT [92],

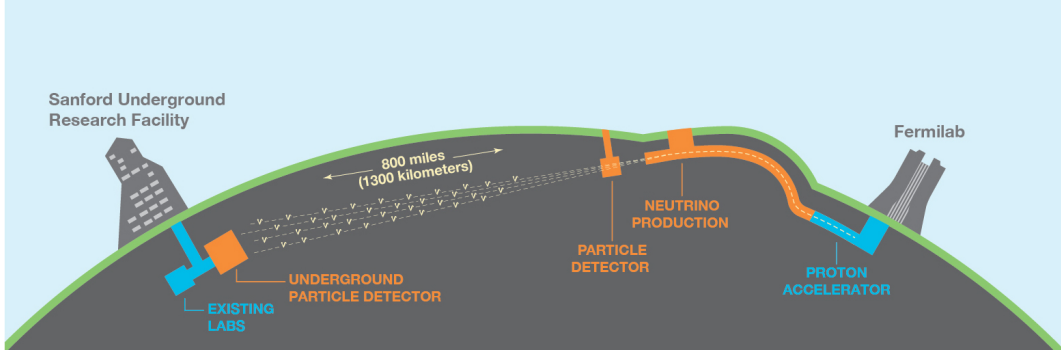


Fig. 3.1 Cartoon showing the configuration of the Deep Underground Neutrino Experiment. The experiment will be based at Fermilab, shown at the right of the figure, and will send neutrinos towards SURF, at the left hand side. The distance travelled, through the Earth's crust, will be 1300 km.

LArIAT [93] and MicroBooNE [94], are successfully using LArTPCs to take and analyse data and it seems certain to be the future of neutrino physics in the U.S. [95].

This section will provide a brief history of LArTPC technology and motivate its potential when used in a large experiment such as DUNE. The basic operation of such a detector will also be described to provide background for discussion of the DUNE and 35 ton experiments, and of reconstruction in LArTPCs, in future chapters.

3.1.1 A Brief History of Time (Projection Chambers)

The use of a time projection chamber as a potential particle detector was put forward by David Nygren in 1974 [96]. He envisioned bubble-chamber quality data but with the possibility of digital readout of the data, facilitating extremely fine spatial resolution, good timing resolution and fast recovery after triggering. The basic concept is a drift chamber containing a noble gas placed within a field to drift ionisation electrons created by a propagating particle towards a multielectron array. This setup allows full three-dimensional reconstruction by combining information from the two-dimensional readout plane with the drift time. Nygren also included a magnetic field to assist particle identification in his design, shown in Figure 3.2.

The extension of this concept to a liquid argon TPC and its potential as a high-precision fine-grained detector medium in neutrino physics was proposed by Carlo Rubbia in 1977 [97]. The use of a noble liquid rather than gas is necessary in neutrino experiments to provide a high enough target mass for increased probability of neutrino interactions. Noble liquids have high electron mobility and low diffusion, favourable properties as the detection of particles is from the ionisation and scintillation light created by the particles. Given the necessity of a high electric field in order to drift these electrons to the readout places, excellent dielectric

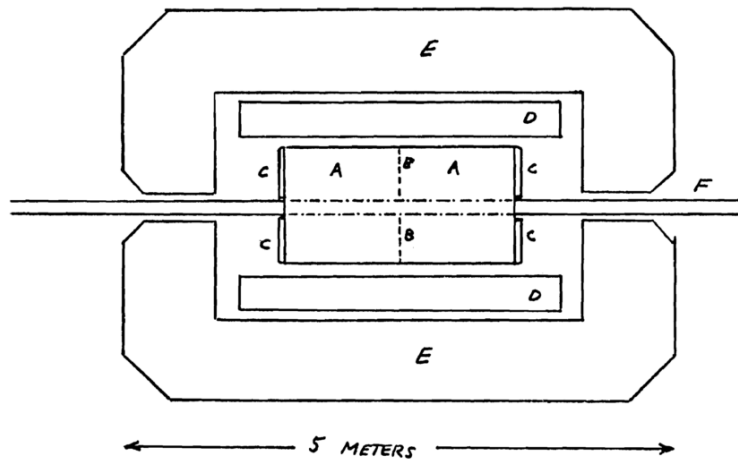


Fig. 3.2 The original concept of the time projection chamber particle detector, drawn by David Nygren in 1974 [96]. The sections are labelled as follows: methane-filled region (A), screen to establish electron field (B), end-cap detectors (C), superconducting solenoid (3.33 T) (D), iron return yoke for magnetic field (E), beam vacuum pipe (F).

properties are also required; noble liquids possess such qualities. The properties of liquid argon which make it almost perfect for this use are demonstrated in Table 3.1.

An additional advantage of this technology is the low threshold for detection; this is set by the ionisation threshold of liquid argon and is only 23.6 ± 0.5 eV [99]. Rubbia realised that a LArTPC could be the digital replacement for the high quality particle detection methods used in bubble chambers, very common in neutrino physics in the 1970s. He proposed the first LArTPC detector design, shown in Figure 3.3, which bears a striking resemblance to the LArTPCs in use today.

Table 3.1 Properties of noble liquids relevant when considering a TPC medium for a neutrino experiment [98].

	Water	He	Ne	Ar	Kr	Xe
Boiling point [K] @ 1 atm	373	4.2	27.1	87.3	120.0	165.0
Density [g/cm ³]	1	0.125	1.2	1.4	2.4	3.0
Radiation length [cm]	36.1	755.2	24.0	14.0	4.9	2.8
Scintillation [γ/MeV]	-	19 000	30 000	40 000	25 000	42 000
dE/dx [MeV/cm]	1.9	0.24	1.4	2.1	3.0	3.8
Scintillation λ [nm]	-	80	78	128	150	175
Abundance (Earth atm) [ppm]	5×10^4	5.2	18.2	9340.0	1.10	0.09
Electron mobility [cm ² /Vs]	low	low	low	400	1200	2200

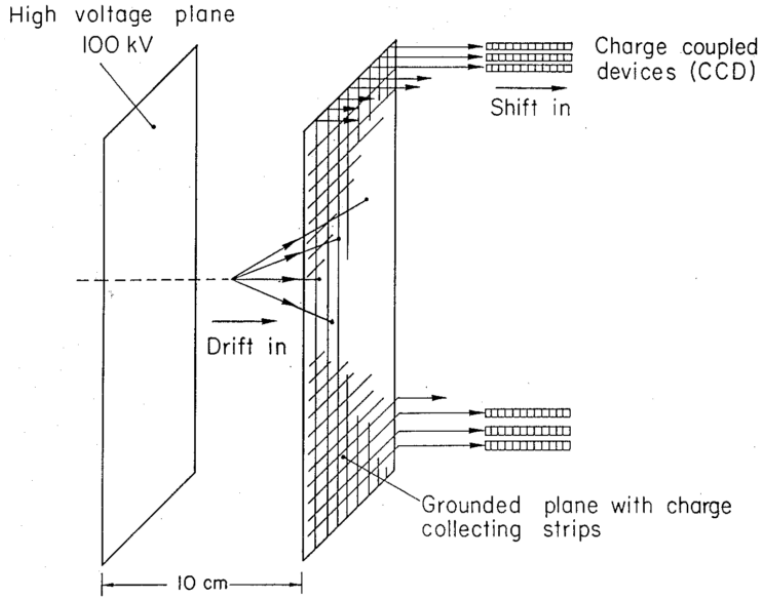


Fig. 3.3 The LArTPC detector proposed by Carlo Rubbia in 1977 [97].

Constructing and operating such a detector was beyond the technology of the time, and is still being understood today. The operation of a LArTPC detector is described in Section 3.1.2 and the associated challenges are the subject of Section 3.1.3.

3.1.2 LAr TPC Operation

A LArTPC typically consists of one or more anodes and cathodes at either end of an active drift region. An ionising particle passing through a LArTPC causes electrons to become free from argon atoms and, in the presence of a field, drift towards an anode where they are read out.

There are two differing designs of LArTPC: single-phase and dual-phase. In a single-phase design, only argon in a liquid state is utilised and the entire detector, including target medium, propagation, readout and signal processing take place within the liquid. In contrast, a dual-phase design would employ a layer of gaseous argon above the liquid, through which the drift electrons are extracted before readout. This has the primary advantage of amplification of signal due to electron avalanches in an electric field in the gas and therefore a lower detection threshold but also results in a larger fiducial volume with the absence of dead regions in the LAr volume.

The readout consists of multiple wire planes with different orientations to facilitate the reconstruction. The wires are either ‘induction’ wires, which allow the electrons to deposit charge but continue past, or ‘collection’ wires, on which the electric field lines end and all

the charge on the electron is collected. Each wire plane is therefore held at a different ‘bias voltage’ to prevent any field lines ending on the induction wire, thus creating local electric fields which promote the continuing forward motion of the electrons. The signal seen is therefore dependent on the type of wire plane; a bipolar pulse on an induction plane wire and unipolar on a collection plane wire. It is also common, though not essential, to make use of a ‘grid plane’ upstream of the signal planes in order to shield them from the electron charge until the drift electrons are close. Without such a plane, the bipolar pulse would be highly asymmetric, though would still have zero integral. It also makes changing the drift voltage (controlling the electric field) slightly easier as the signal planes are somewhat shielded from its effects. MicroBooNE does not operate with a grid plane and, although the 35 ton and the DUNE reference design make use of a grid plane, it is uncertain whether the benefit outweighs the cost for a huge LArTPC detector such as the DUNE far detector. There are alternative readout possibilities to this typical design which have been suggested but, given the scale of future LArTPCs, it is highly unlikely a viable solution which delivers superior readout at a comparable cost will be found.

Upon ionisation, an electron has a certain probability (around 60%) of recombining before the field can separate it from its ion. Whilst this compromises the signal observed, it is accompanied by a flash of scintillation light which may be detected and used to assign an ‘event time’ to the interaction, known as T0. Without this information, it would be impossible to place an absolute time scale on the event and result in an unresolved coordinate along the drift direction. The magnitude of the applied electric field must be chosen to balance these two effects; a larger field would result in less recombination and therefore compromise the scintillation light while a smaller field would have consequences on the signal received at the wire planes. Figure 3.4 demonstrates this and justifies the field value of 500 V/cm which is often chosen in current LAr neutrino experiments.

The basic operational principles of a LArTPC is demonstrated in Figure 3.5. The specifics of how the ionisation charge and the scintillation light is collected and processed is experiment-specific and will be discussed in the context of DUNE in Chapter 3 and the 35 ton experiment in Chapter 4. This information is all that is required to fully understand and analyse the interactions occurring in the detector; methods used to reconstruct particles and interactions in LAr will be the subject of Chapter 5.

3.1.3 LArTPC Challenges

There is no doubt of the promise of LArTPCs for the future of neutrino physics but with such expectation comes many challenges. This will be elaborated upon in more detail when discussing the 35 ton run in Section 4.8 but will be briefly mentioned here for completeness.

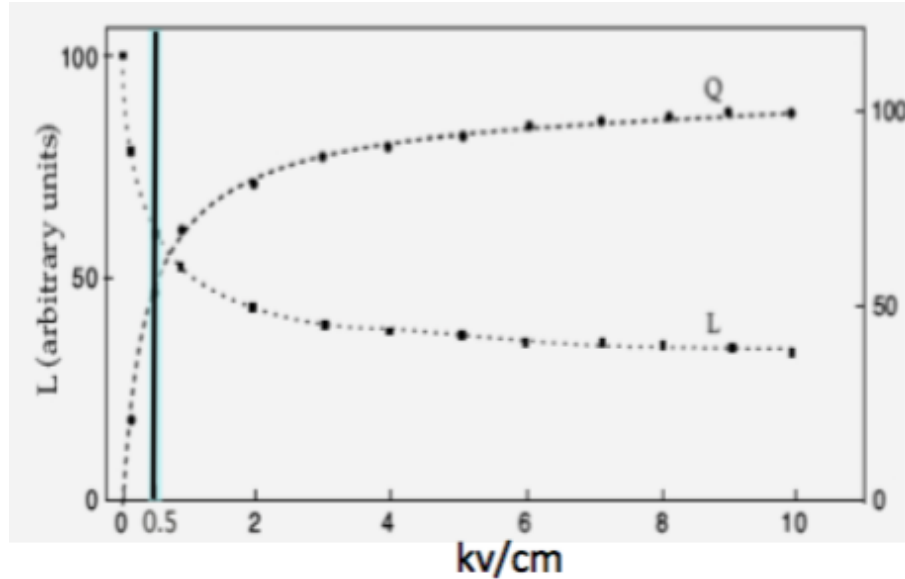


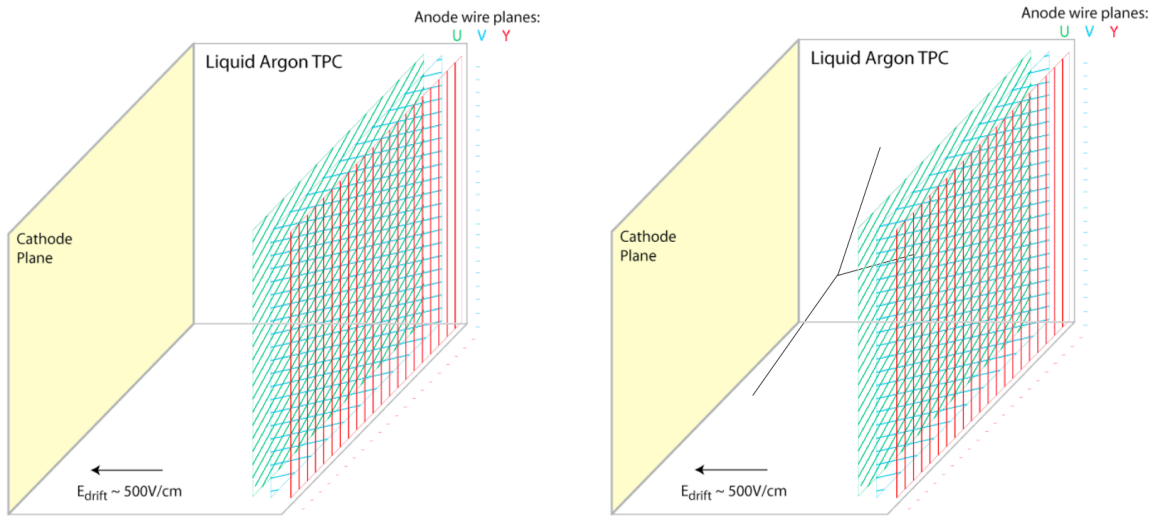
Fig. 3.4 Demonstration of the competing effect the electric field has on the luminosity of the ionisation electrons and scintillation light arriving at the detector readout. Since both are essential in reconstructing the complete interactions, a balance must be found. [PLACEHOLDER IMAGE].

Given the drift fields required, and the necessary distances, the associated high voltage on the cathode must be on the order of ~ 100 kV. This presents engineering challenges related to the feedthrough and cryostat design but also can lead to dielectric breakdown of the liquid nearby such huge voltages. The properties of LAr and the design implications must be very well understood to ensure this does not endanger the quality of the detector medium.

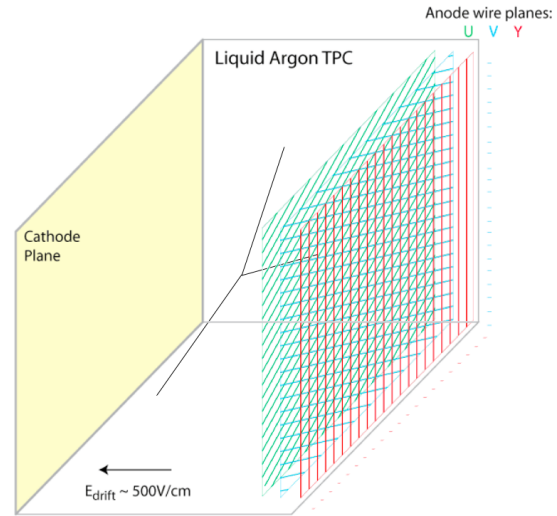
The presence of electro-negative impurities in the argon can capture drift electrons as they travel towards the anode planes and hinder the signal observed. The probability of this recombination is referred to as the ‘electron lifetime’ and is directly affected by the maintained purity of the argon. DUNE expects a contamination no greater than 100 ppt O₂ and 20 ppm N₂ (to also ensure sufficient light yield) [90]. This necessitates a purification system to remove impurities and requires the constant recirculation of the liquid through it. A liquifier is also necessary to recondense any boiled-off gases at the surface.

Along with the possibility of lost signal through finite electron lifetimes, the electrons may also undergo interactions and drift off course either transversely or longitudinally. This ‘diffusion’ affects the location and size of the observed signal so must also be well understood.

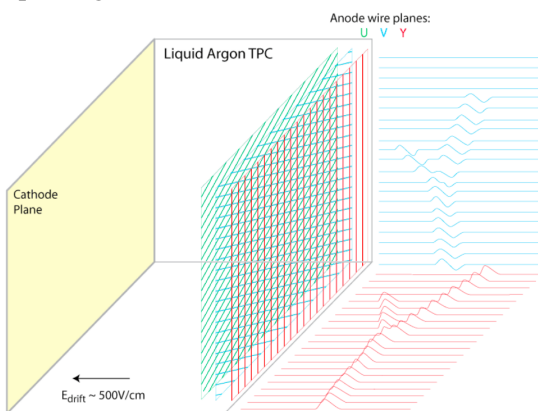
With so much resting on the success of the DUNE experiment, and considering all these effects which must be understood, prototyping is essential. The 35 ton prototype was constructed as an attempt to better understand LArTPCs and is the subject of Chapter 4.



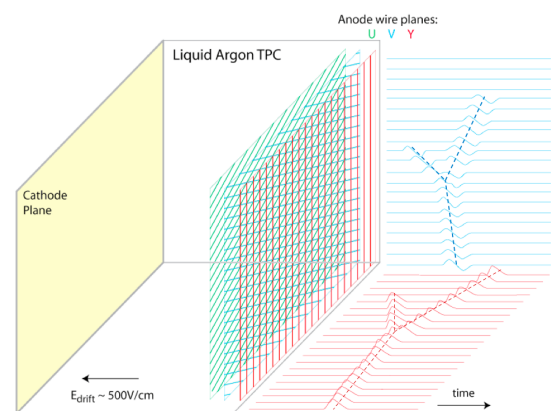
(a) Typical LArTPC with one cathode (left) and three read out anode planes (right) (two induction, U and V, and one collection, Y), setting up an electric field. The central region is filled with liquid argon.



(b) An ionising particle enters the detector and liberates electrons from the medium, which then drift towards the anode planes.



(c) As the electrons drift through, charge is induced on the first two wire planes and collected on the final one. Due to the differing orientations of the wires between planes, three complementary views of the interaction are provided (two are shown).



(d) By combining the two dimensional information provided by the anode planes with the drift time information, the original particle tracks can be inferred.

Fig. 3.5 Schematic demonstrating the basic operational principles of a LArTPC. The images are stills taken from an illustration created by Bo Yu (BNL) ([do I need to cite this? It's a very common slide and I can't actually find a Bo Yu talk with it in... everyone just puts his name on the slide!](#)).

3.2 Overview of DUNE

The outstanding questions in neutrino physics discussed in Section 2.3, namely the resolution of the mass hierarchy, the determination of the CP-violating phase δ_{CP} , the measurement of the octant of θ_{23} and precision calculations of all the mixing angles, motivate the need for next generation experiments. The DUNE experiment will make decisive contributions to each of these areas; it will also search for nucleon decay with the ability to set world-leading proton lifetime limits and make detailed, unique measurements of the ν_e flux from a core-collapse supernovae within our galaxy should one occur during the experiment. Along with this, DUNE will be used to look for Beyond Standard Model physics (such as non-standard interaction and sterile neutrinos), signatures of dark matter and, utilising the capable near detector, measurements of a range of neutrino cross-sections and nuclear effects including final state interactions.

The chosen technology for the DUNE far detector, in order to maximise sensitivity to all these factors, is a LArTPC, introduced and described in Section 3.1. The detector will contain four modules, each comprised of 10 kt fiducial LAr and separate data acquisition and readout systems. The beam will be provided by Fermilab as part of its PIP-II program [100] and will be wide band, enabling the study of a range of neutrino energies. This facilitates a study of multiple oscillation peaks, essentially due to differing L/E ratios, and is relevant when considering the effects of an unknown CP-violating phase and unresolved mass hierarchy. Since the impact of both of these uncertainties is apparent as an asymmetry between neutrinos and antineutrinos (Equation 2.32), there is an implicit degeneracy which must be resolved to ensure both phenomena are correctly determined. Having access to multiple oscillation peaks means this may be dealt with in a single experiment, as demonstrated in Figure 3.6 [101].

DUNE was officially formed in early 2015 following the dissolution and merging of two leading next generation long-baseline experiments: the Long Baseline Neutrino Experiment (LBNE) in the U.S. [102–104] and the Large Apparatus for Grand Unification, Neutrino Astrophysics, and Long Baseline Neutrino Oscillations (LAGUNA-LBNO) in Europe [105]. Given the scale of these projects, it was decided in 2014 that efforts should be focussed on one flagship experiment utilising the expertise of as many experts in neutrino physics and LArTPC technology as possible [106]. The benchmark DUNE design is very similar to that of the former LBNE experiment, which also made use of an upgraded Fermilab neutrino beam and a large LArTPC at SURF, and gained the understanding of dual-phase LArTPC detectors developed by LAGUNA-LBNO. It is likely that at least one of the four DUNE detector modules will be a dual-phase LArTPC.

The experiment will be facilitated by the Long Baseline Neutrino Facility (LBNF), which will oversee the technical side of the project and ensure the DUNE experiment can function

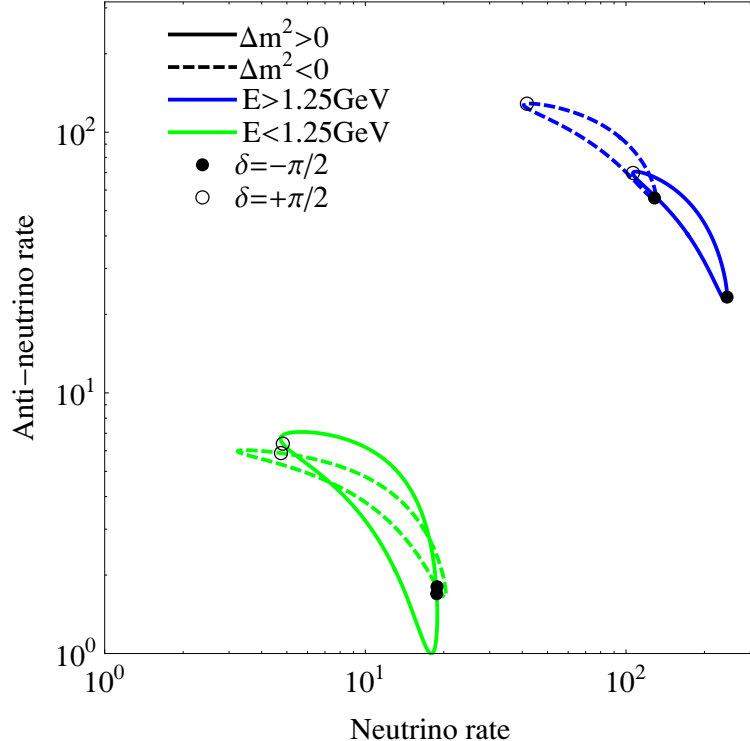


Fig. 3.6 Demonstration of how having access to multiple oscillation maxima facilitates measurements of both the neutrino mass hierarchy and leptonic CP violation using the same experiment. In the plot, θ_{13} is held constant and the rates are determined by the number of neutrino and antineutrino events respectively. Assuming a baseline of 1300 km, as for DUNE, the first oscillation maximum is at $E_\nu = 2.5$ GeV and the second is at $E_\nu = 0.84$ GeV. The banana-shaped distributions are obtained as the value of δ_{CP} is varied from $-\pi$ to π . There is good separation between the distributions associated with each hierarchy at the first maximum whereas at the second maximum this is degenerate and the rates are similar for a given value of δ_{CP} regardless of the hierarchy. It can be seen how complimentary measurements at each maxima can be used to make unambiguous measurements of both the mass hierarchy and of CP violation with the same experiment. Taken from [101].

as desired. The relationship between the LBNF and the DUNE projects is based on the model used at CERN to manage the Large Hadron Collider (LHC) and each of the experiments which use it. LBNF has its own management structure and operates separately from DUNE, though the two projects work closely together. It is supported mainly via the Department of Energy in the U.S. whereas DUNE is internationally funded. The DUNE collaboration is responsible for defining the scientific goals of the experiment and the corresponding technical requirements. Using these, LBNF will design and construct all technical facilities, such as the beam upgrade, the facilities for the near detectors at Fermilab and the excavation and outfitting of the large caverns for the far detectors underground at SURF along the required infrastructure to support the construction of the cryostats and the associated cryogenic systems. DUNE will provide the four massive LArTPCs and the near detector systems, to be constructed at the sites supplied by LBNF. These will be discussed further in Section 3.3. During the lifetime of the experiment, LBNF is responsible for the maintaining and operation of all the facilities whilst DUNE will commission and operate the detectors. The scientific research program conducted with the collected data is the duty of the DUNE collaboration and will be explored in Section 3.4.

Given the scale of the projects, work is already underway. Construction at the far detector site starts this year, with installation of the first detector module due to commence in 2021. The start of the DUNE experiment will then correspond to the completion of this module, scheduled in 2024. The PIP-II upgraded 1.2 MW beam will be ready in 2025 and will signify the commencement of beam data taking. Subsequent detector modules will be added as soon as is feasible thereafter, increasing the fiducial volume up to the target mass of 40 kt. Further beam upgrades, up to 2.4 MW (PIP-III) are envisaged beyond this to bring the experiment up to full power and maximise the physics capability of the project. The timescales of both LBNF and DUNE, along with all the essential research which must be conducted as the plans progress, is the subject of Section 3.5.

3.3 Experimental Details

The design of the DUNE experiment is driven by the physics ambition of the project and all specific experimental details are motivated by the science DUNE wishes to study. This section will briefly report on the current understanding of how DUNE will be planned. It should be noted that whilst the important defining features of the design will endure it is likely, given the timescales of the project, particular details will change for the final proposal.

The plans for the beam will be overviewed in Section 3.3.1 before the present considerations for the far and near detectors are presented in Sections 3.3.2 and 3.3.3.

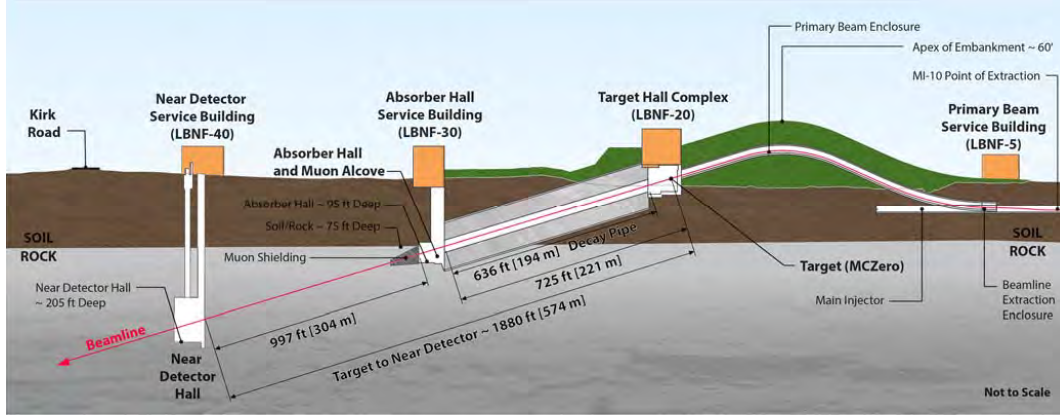


Fig. 3.7 Longitudinal section of the LBNF beamline facility at Fermilab [89].

3.3.1 Beam

The beam is required to be wide band to facilitate access to the first two oscillation maxima (at 1300 km, 2.4 GeV and 0.8 GeV). It is a conventional, horn-focussed, sign selected neutrino beam and is detailed in Figure 3.7.

A proton beam (60-120 GeV) is extracted from the Fermilab Main Injector, transported through a man-made embankment and bent downwards to establish the final trajectory towards the far detector. The beam is incident on a target to produce secondary mesons which are subsequently focussed into a decay pipe by magnetic horns where they decay into muons and neutrinos. The polarity of the horns used determines whether or not the beam is neutrino or antineutrino dominated. At the end of the decay pipe, the muons and any residual hadrons are stopped to produce a beam of neutrinos, tuned with energies between 0.5 GeV and 5 GeV. The fluxes of different neutrino species present in the beam in both neutrino- and antineutrino-running modes are shown in Figure 3.8. The target is based on the design used in the Fermilab NuMI (Neutrinos from Main Injector) beam, in operation since 2005, and consists of a graphite core with dual titanium water lines to dissipate heat, encased in a titanium containment tube.

The current beam design has been evolving since 2012 when it was first conceived for the LBNE experiment. Many potential optimisations have been identified and some are now part of the reference design; others are still in the process of evaluation. In the sensitivities presented in Section 3.4, two beam configurations are referred to: reference and optimised. The optimised design pertains to such ongoing considerations envisioned to improve performance, for example in flux at the first and especially the second oscillation maximum and in the reduction of wrong-sign neutrino backgrounds. The improvements are

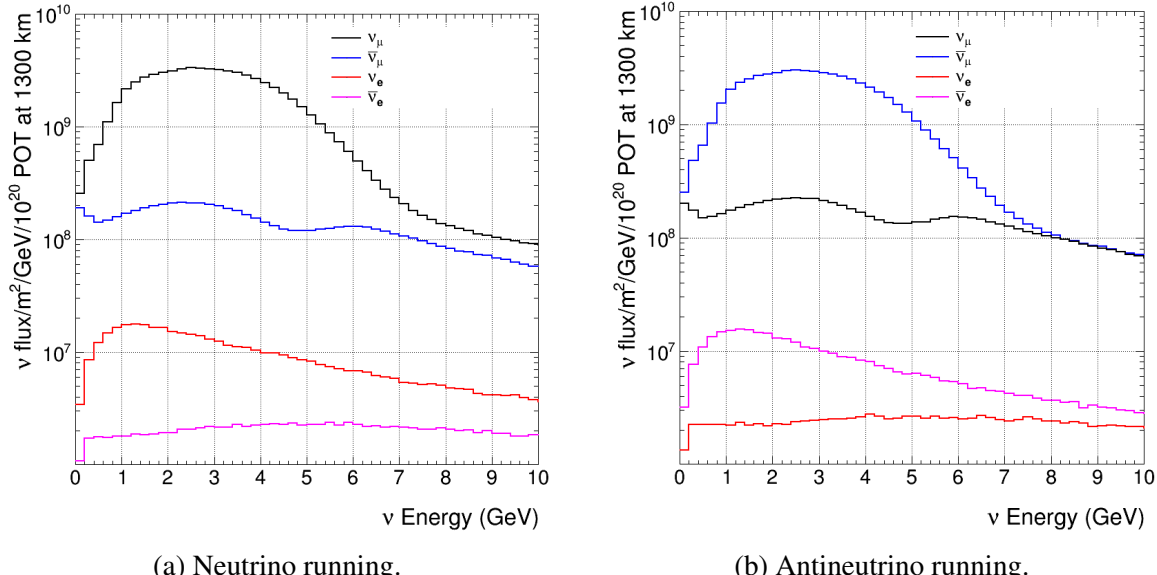


Fig. 3.8 The fluxes of the different neutrino flavour components of the DUNE beam in neutrino and antineutrino running mode [89].

foreseen to come from an thorough assessment of the target-horn system and will influence the reference design as the beam plans become more mature.

3.3.2 Far Detector

There are two potential designs for a far detector LArTPC utilising either single-phase or dual-phase LArTPCs. Both are under consideration in the upcoming ProtoDUNE prototypes (described in Section 3.5) and final decisions will be taken upon their completion and on reflection on the status of the technology. The first module will certainly employ a single-phase design with future instalments potentially either. The design of the cryostats, demonstrated in Figure 3.9, is such that only minor modifications would be required when switching between technologies. Each cryostat will hold a fiducial/active/total LAr mass of 10.0/13.3/17.1 kt.

The basic features of each detector design will be overviewed in the following sections. As the first detector will be single-phase, and the work detailed in this thesis pertains solely to this detector design, a much greater emphasis will be placed on this design choice in the proceeding discussions.

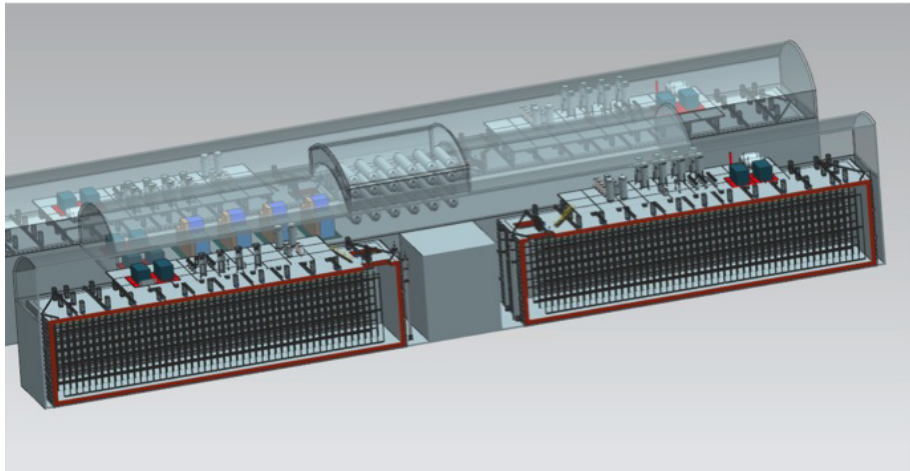


Fig. 3.9 The layout of the four cryostats underground at SURF comprising the DUNE far detector [90]. The detectors occupying the cryostats here are of the single-phase design, however they can also be used to accommodate detectors utilising dual-phase technology.

3.3.2.1 Single-Phase

The layout of the single-phase DUNE detector design is shown in Figure 3.10. The modular form of the detector ensures it is flexible and scalable and facilitates the transportation and assembly of component parts. The detector units are named Anode Plane Assemblies (APAs) and Cathode Plane Assemblies (CPAs) and, as their names suggest, carry the required voltages necessary to establish the electric field. The active volume is 12 m high, 14.5 m wide and 58 m long in the beam direction, with the APAs and CPAs placed such that their planes are parallel to the beam. Each APA is 2.3 m wide and 6 m high, requiring them to be stacked two high and 25 long to instrument the required volume. The CPAs have the same width but half the height so must be stacked four high and, given the drift distance of 3.6 m, carry a voltage of -180 V in order to provide the required field of 500 V/cm. Each module therefore contains 150 APAs and 200 CPAs, surrounded on its open sides by a field cage. The entire TPC is suspended from the ceiling of the cryostat on rails.

The basic design of an APA is demonstrated in Figure 3.11. Each comprises four sets of wire planes; from the outside in: a grid plane (G), two induction views (U and V) and a collection plane (Z). The APAs are designed to maximise active detector region and are therefore stacked as closely together as possible and read out charge from multiple drift regions simultaneously. This requires all readout be positioned at the top (or bottom of lower APAs) of the frame and use of a wrapped wire approach for the induction wires, since these must be fixed at an angle. This wrapping also carries the added benefit of reducing the number of channels required since a wire from the U plane on one side of an APA is

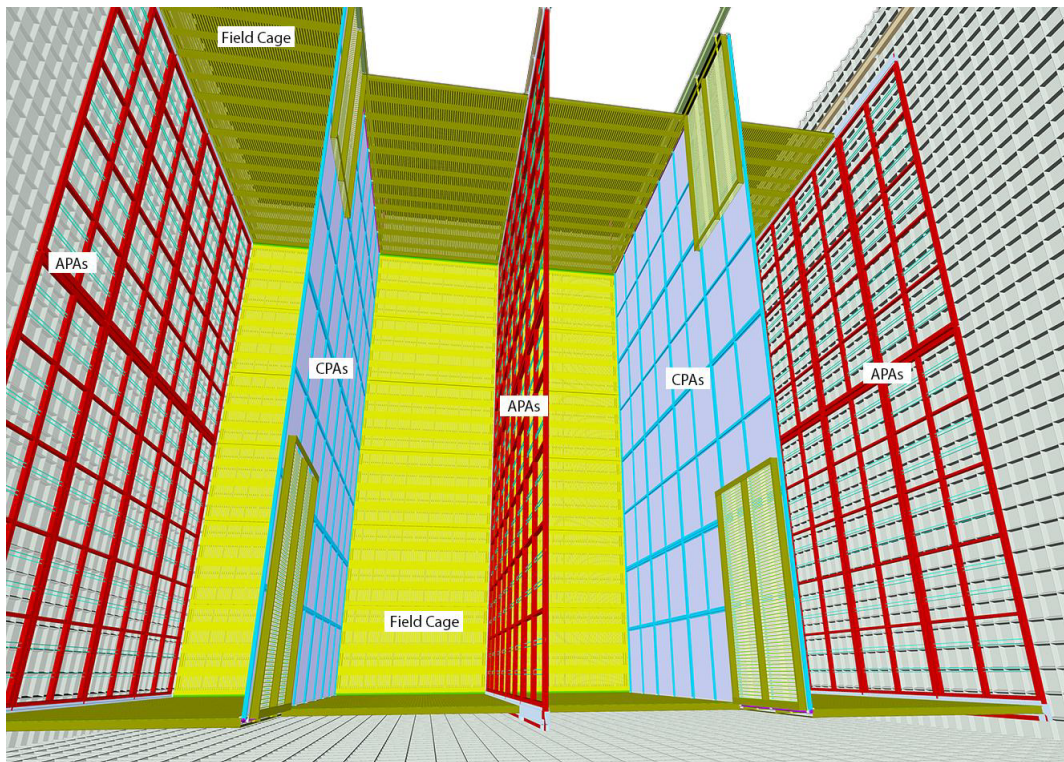


Fig. 3.10 The basic design of a single-phase DUNE far detector module [90]. The beam direction is into the page and the electric field, provided by the Anode Plane Assemblies (APAs) and Cathode Plane Assemblies (CPAs), is perpendicular to this across the page.

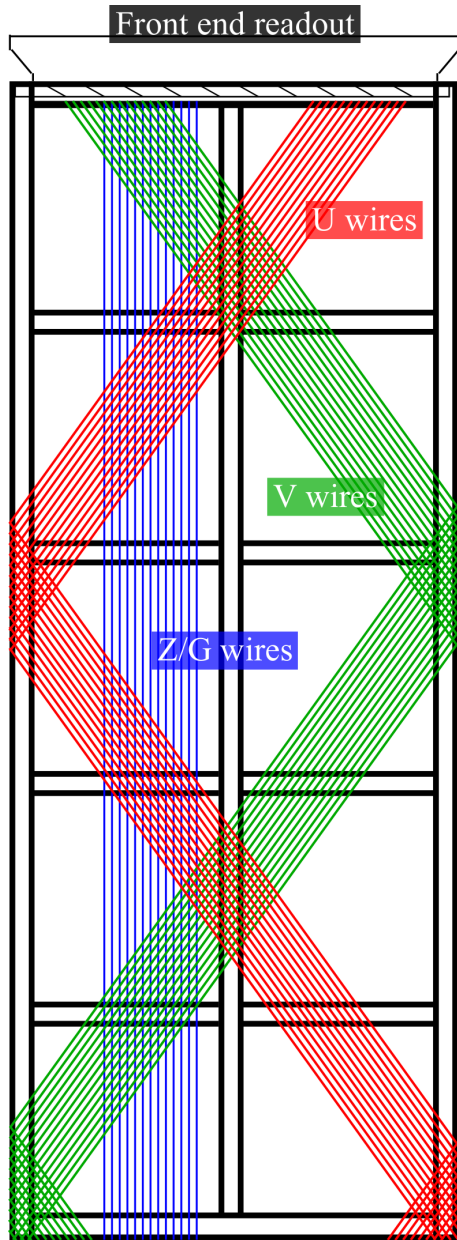


Fig. 3.11 Design of a DUNE far detector Anode Plane Assembly (APA). The three instrumented planes, collection (Z) and two inductions (U and V), are shown in blue, red and green respectively. The grid plane is not shown but is parallel to the collection wires. The induction wires are wrapped around the frame and make angles of $\pm 35.7^\circ$ to the vertical, chosen so that each wire segment crosses each collection channel no more than once. This ensures there is no ambiguity in the side of the APA the charge arrived at.

part of the V plane on the opposite side. The collection and grid wires are both vertical, necessitating a set for each face of an APA. A single wire reading out multiple drift regions concurrently potentially leads to an ambiguity in the particular wire segment at which the charge arrived. This is broken in one of two ways; either the wires in the U and V planes are placed at slightly different angles, reducing the number of triple crossing points with a given collection wire, or the angle of the induction plane wires is chosen such that each wire segment intersects no more than one collection wire. The former is prototyped in the 35 ton experiment whilst the current plan for the DUNE far detector is to opt for the latter. An angle of $\pm 35.7^\circ$ ensures this is the case, demonstrated in Figure 3.11. A grounded mesh, with good optical transparency, is fixed to the face of the APA frame behind each collection plane to ensure a uniform electric field in the region inside the APA, between the two sets of biased collection wires and the grounded frame.

The front-end electronics are mounted on the APAs and function within the cryostat; it is for this reason they are referred to as ‘cold electronics’. They are implemented as two successive ASIC chips, the first providing amplification and signal shaping and the second the digitisation of the signal. Early versions of these chips were utilised in the 35 ton experiment for front-end readout. *Note to me: could put picture of signal shaping here if it appears necessary as I write about the 35ton stuff...*

The external triggering in the DUNE far detector relies on detecting the scintillation light from immediate recombination of ionisation electrons with the argon ions. This requires dedicated photon detectors which may detect this light with suitable efficacy. At a field of 500 V/cm, the photon yield is around 20,000 per MeV at wavelengths of 128 nm. The current reference design, depicted in Figure 3.12, involves placing light-guides, containing wavelength shifter, at the centre of each APA frames and using SiPMs for readout. There will be 10 per APA, to be inserted after wire wrapping, with dimensions 2.2 m long, 83 mm wide and 6 mm thick.

Overall, optimisation of this detector design involves considerations of the physics reach as well as the associated cost, schedule and risks. Relevant decisions concern the spacing between the readout wires (‘pitch’), which directly affects the detector resolution; the spacing between the wire planes, affecting the shape of the field; the wire angle, necessary for reconstruction but with possible ambiguities; the wire length, affecting the noise levels observed; and the maximum drift length, which influences the size of signal observed. Each has been optimised to ensure the physics goals are reached while reducing as much as possible the cost of the detectors.

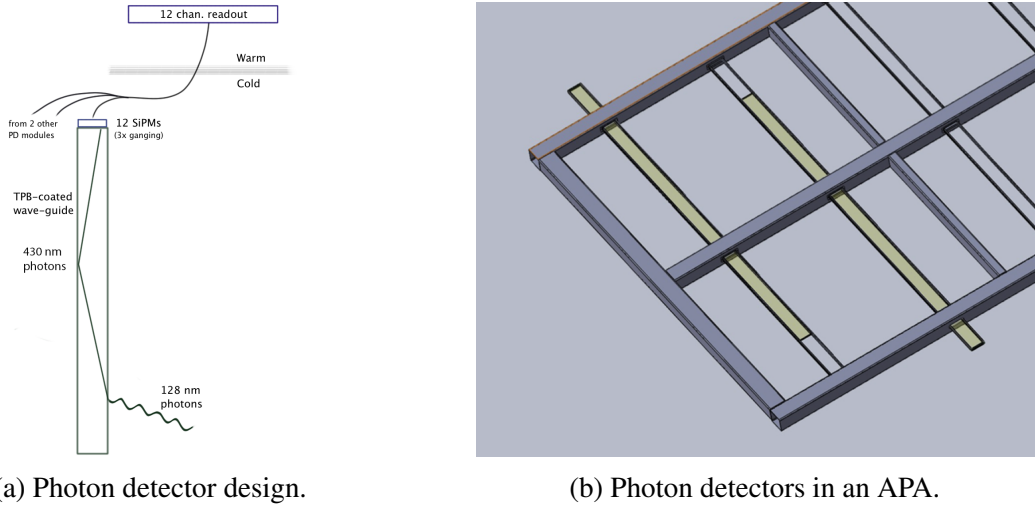


Fig. 3.12 The design of the photon detectors for the DUNE far detector [90]. The basic design of each bar is shown in Figure 3.12a and their positioning within an APA is shown in Figure 3.12b.

3.3.2.2 Dual-Phase

The DUNE dual-phase LArTPC design differs from its single-phase counterpart in that the cathode is placed at the bottom of the cryostat, with the anode readout at the top (above the gas layer), demonstrated in Figure 3.13. This sets up a field in the vertical direction and results in upwards electron drift. The detector is a single volume, 60 m long, 12 m wide and 12 m high. Due to the gain provided by the gas phase, the required argon purity is equivalent to the single-phase detector despite the electron drift being more than three times greater. Each module additionally contains 180 PMTs (1 per 4 m^2), located underneath the cathode.

The amplification uses Large Electron Multipliers (LEMs): printed circuit boards with electrodes at the top and bottom surfaces across which a potential difference is applied. The data collection is performed by modules named Charge Readout Planes (CRPs), each containing many LEM/anode sandwiches and two independent, orthogonal readout views. The basic operation, including the electric fields at each point in the electron extraction, amplification and readout, is demonstrated in Figure 3.14. As with the single-phase design, the nominal drift field in the liquid is 0.5 kV/cm. The electrons are extracted from the liquid with 100% efficiency using a 2 kV/cm field and are amplified in a field on the order of 30 kV/cm, providing a gain between 20-100. The readout utilises two perpendicular collection planes at the same level which allow full 3D reconstruction when combined with the location in the drift direction from photon detector information. Each CRP has dimensions $3 \times 3 \text{ m}^2$ (containing 36 ($0.5 \times 0.5 \text{ m}^2$) LEM/anode sandwiches) and each module requires 80 such instruments to read out the active volume.

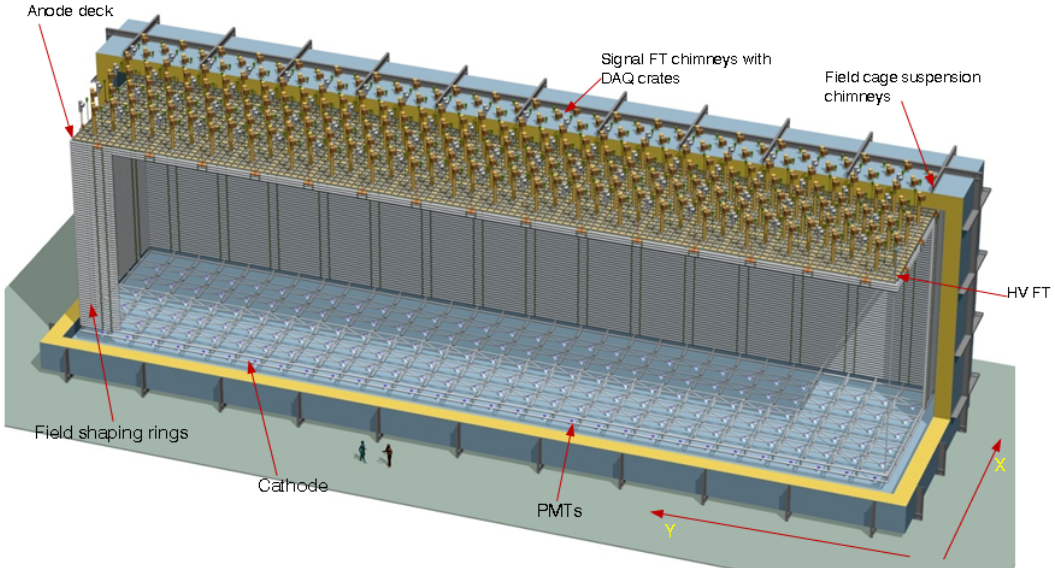


Fig. 3.13 The DUNE dual-phase detector (partially open) [90]. The cathode is at the bottom of the cryostat, with the PMTs responsible for detecting the scintillation light beneath. The anode is at the top, resulting in upwards electron drift, above a layer of gaseous argon present to introduce a gain in the collected signal.

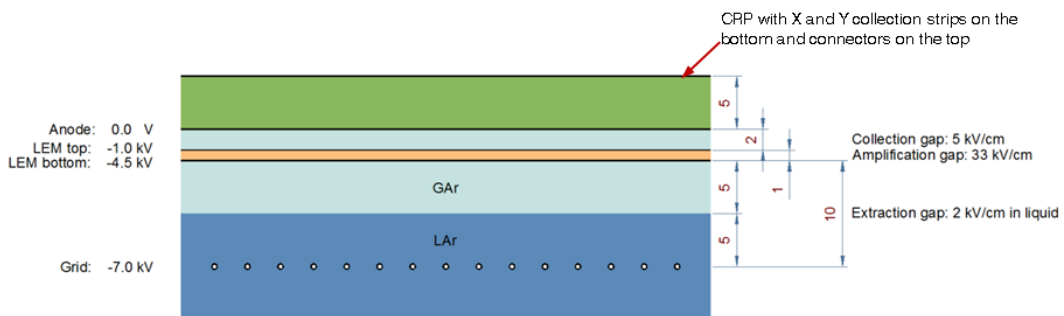


Fig. 3.14 The extraction, amplification and readout of the ionisation electrons through the gaseous argon phase in the DUNE dual-phase LArTPC design [90]. The voltages at each stage are shown on the left and the associated fields set up are described on the right.

3.3.3 Near Detector

The primary role of the near detector is to characterise the energy spectrum and the composition of the neutrino beam before oscillations have occurred, and to make measurements of neutrino interaction cross-sections. This is necessary to control systematic uncertainties and requires good understanding of the muon- and electron-flavoured neutrino and antineutrino components of the beam. The unprecedented number of neutrino interactions collated by the near detector will also facilitate a broad program of ancillary physics and is an important constituent of the DUNE experiment.

The near detector will comprise of a near neutrino detector (NND) to perform these studies and a Beamline Measurement System (BLM) located downstream of the beam absorber designed to make measurements to constrain the neutrino flux at the near and far detectors. The NND and BLM systems will be the subject of Sections 3.3.3.1 and 3.3.3.2 respectively.

3.3.3.1 Near Neutrino Detector

The NND is required to make precise measurements of neutrino interactions and distinguish between all four particle species present in the beam in order to characterise their spectra. The current design utilises a magnetised Fine-Grained Tracker (FGT) design containing a Straw-Tube Tracker (STT) and Electromagnetic Calorimeter (ECAL), shown in Figure 3.15. The STT and ECALs are surrounded by a 0.4 T dipole magnet and also employ muon identifiers (MuIDs) in the magnet steel and upstream/downstream of the STT. The detector is yet to be finalised and it is possible a different design will be chosen instead, or additional detectors added such as a small-scale LArTPC or high-pressure argon TPC to further reduce systematic uncertainties.

The STT consists of over 107,000 tubes made from carbon and aluminium and with outer diameter 1 cm to provide fine-grained tracking (thickness $< 0.1X_0$) with excellent angular and spatial resolution. The tubes will be filled with either 70% Ar, 30% CO₂ or 70% Xe, 30% CO₂ depending on the positioning of the tubes in the detector and are read out at both ends. Nuclear targets will be placed upstream with multiple materials used to make complimentary measurements. Pressurised argon gas or calcium will allow nuclear effects of neutrino interactions on argon and modelling of signals and backgrounds in the DUNE far detector. Carbon (graphite) may also be used to study interactions on free protons and H₂O and D₂O targets will allow analysis of interactions on quasi-free neutrinos via statistical subtractions.

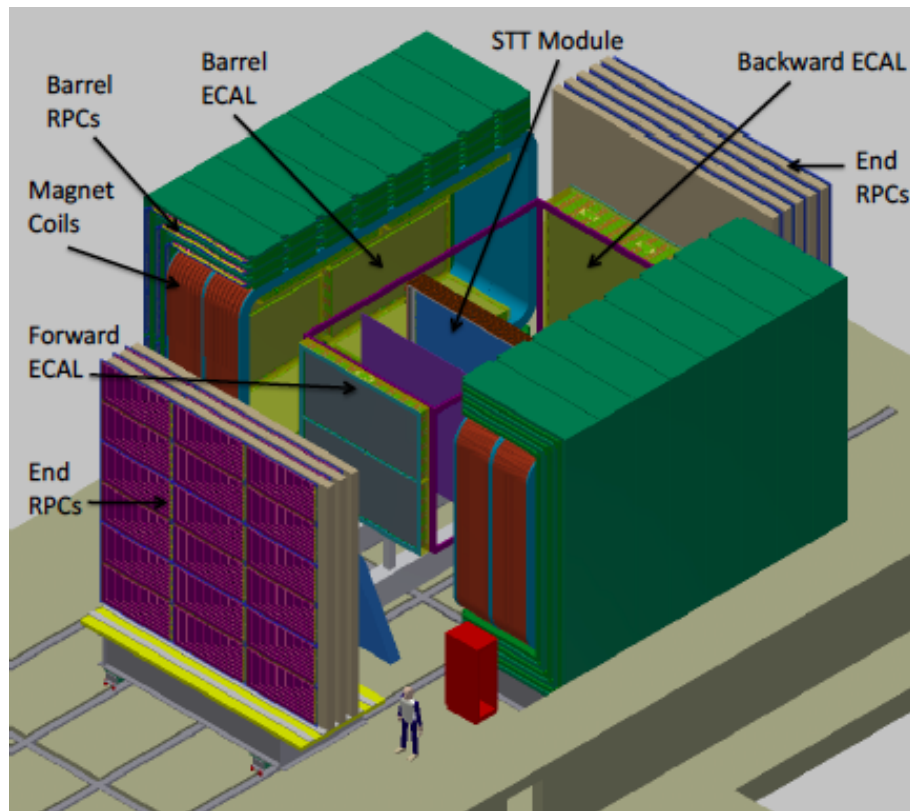


Fig. 3.15 Schematic of the DUNE near neutrino detector fine-grained tracker design [90].

The ECAL provides high segmentation in both the transverse and longitudinal directions and is composed of three separate systems; Forward ECAL, Barrel ECAL and Backward ECAL. It is designed to reconstruct photons from π^0 decay and electrons and positrons from Bremsstrahlung radiation and consists of layers of either 1.75 mm thick (Forward ECAL) or 3.5 mm thick (Barrel and Backward ECALs) lead sheets positioned within 2.5 cm wide, 10 mm thick plastic scintillator bars.

The 0.4 T magnet has inner dimensions 4.5 m wide, 4.5 m high, 8.0 m long and assists with measurements of particle momentum and charge. It is also instrumented with the MuIDs designed to distinguish muons from hadrons utilising the ability of muons to penetrate the iron without showering or interacting. The MuID is comprised of 432 resistive plate chamber (RPC) modules distributed within two 10 cm thick steel plates of the magnet and will also perform basic reconstruction on the muon track segments which can be matched with tracks from the STT tracker for global object reconstruction.

3.3.3.2 Beamline Measurement System

The beamline measurement system will operate for the life of the experiment and will monitor the beam profile on a spill-by-spill basis. Along with constraining the neutrino flux, it will be used to monitor the pulse-to-pulse variations for beam diagnostics. It will make measurements of the muons exiting the decay pipe originating from the meson decays which created the neutrinos in the beam. This provides an independent measure of the muon neutrino flux and an additional handle on beam electron neutrinos resulting from muon decays. The measurements are also useful in validating the simulation of the thick target, horn material, decay tunnel and absorber.

3.4 The Physics of DUNE

The staged approach to the DUNE experiment will allow early preliminary results but will require more time for facilities from later phases to be constructed and commissioned. For this and other reasons, the accumulated data is often referred to as an ‘exposure’, a function of detector size, beam power and time with units $\text{kt}\cdot\text{MW}\cdot\text{year}$. The current assumptions on exposures for the first few years of operation are shown in Table 3.2. This staging will be assumed in all sensitivities presented in this section.

The appearance probability expected at the DUNE far detector is demonstrated in Figure 3.16 for various values of δ_{CP} . It can be seen why a broadband beam with the ability to operate in neutrino and antineutrino mode mode is critical; the value of δ_{CP} affects both the

Table 3.2 Exposures anticipated for the DUNE experiment for the first few years of operation. Due to the staged approach in construction, it will take some time to reach full design capabilities. The first exposure column represents the exposure expected in that year and the next column the cumulative total. Adapted from [66].

Year	Exposure (kt·MW·year)	Total (kt·MW·year)	Detector stage
Year 1	10.7	10.7	10 kt far detector, no near detector, 1.07 MW 80 GeV proton beam (1.47×10^{21} pot per year)
Year 2	21.4	32.1	Addition of second 10 kt far detector module
Year 3	32.1	64.2	Addition of third 10 kt far detector module and initial constraints from near detector
Year 4	42.8	107.0	Addition of fourth 10 kt far detector module
Year 5	42.8	149.8	Inclusion of constraints from full near detector data analysis
Year 7	85.6	278.2	Upgrade beam power to 2.14 MW for 80 GeV proton beam

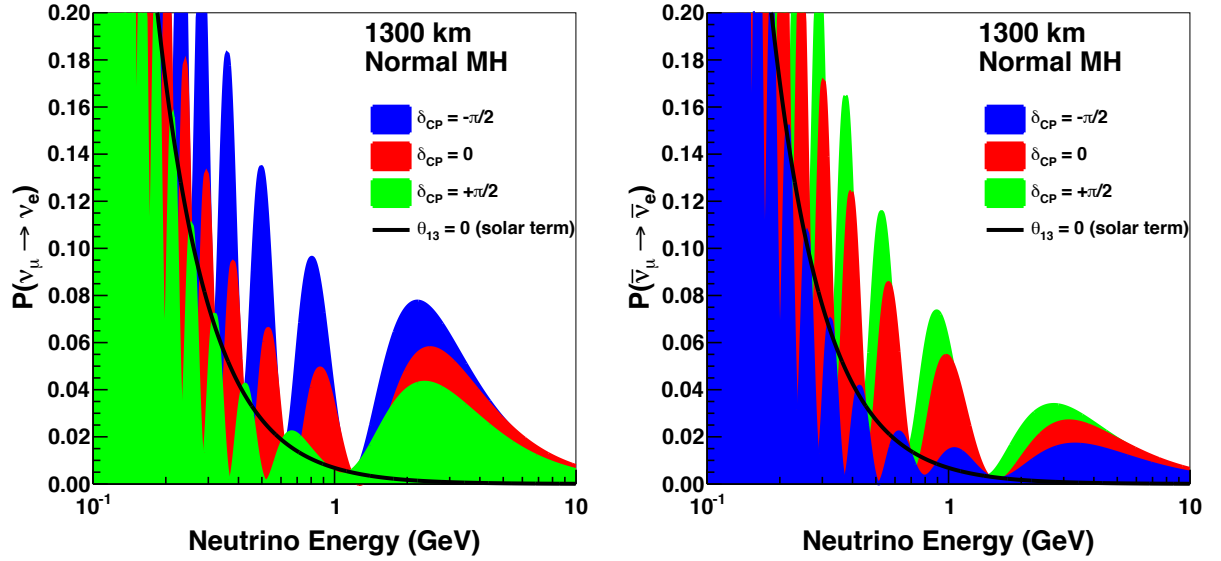


Fig. 3.16 The appearance probability at a baseline of 1300 km, as a function of neutrino energy, for $\delta_{CP} = -\pi/2$ (blue), 0 (red) and $\pi/2$ (green) for neutrinos (left) and antineutrinos (right), for normal hierarchy. The black lines indicates the oscillation probability if θ_{13} were equal to zero. Taken from [88].

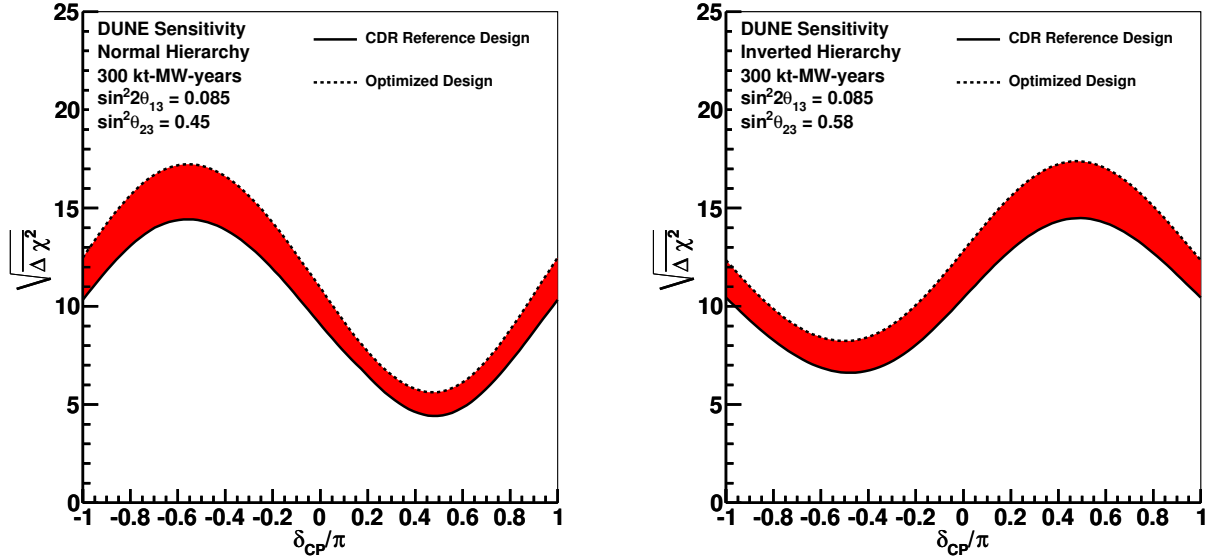
frequency and amplitude of the oscillations, with differing effects at the distinct oscillation nodes and between neutrinos and antineutrinos.

3.4.1 Mass Hierarchy and CP Violation

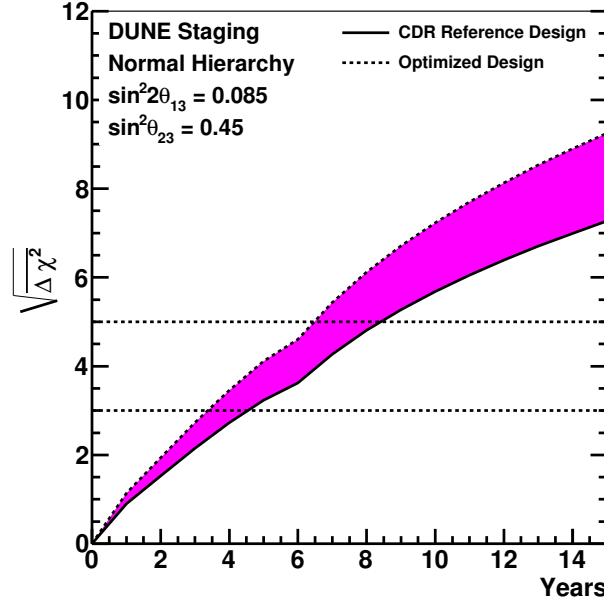
The measurements of the mass hierarchy and the degree of CP violation are determined by simultaneously fitting the $v_\mu \rightarrow v_\mu$, $\bar{v}_\mu \rightarrow \bar{v}_\mu$, $v_\mu \rightarrow v_e$ and $\bar{v}_\mu \rightarrow \bar{v}_e$ oscillated spectra, assuming 50% neutrino, 50% antineutrino exposure.

The sensitivity of DUNE to the neutrino mass hierarchy is shown in Figure 3.17. It is evident DUNE will discover the ordering of the mass states at 5σ significance within the first few years of running, regardless of the value of δ_{CP} . This is achievable because of the large matter effects present with a 1300 km baseline; the asymmetry between neutrinos and antineutrinos due to this is approximately $\pm 40\%$ in the region of peak flux.

The equivalent sensitivities for CP violation is displayed in Figure 3.18. It is impossible to cover 100% of δ_{CP} values because, in the case of CP conservation, the violation effects (i.e. disparities between neutrino and antineutrino oscillations) disappear. DUNE will be able to measure 75% of possible δ_{CP} values with 3σ significance after 1320 kt·MW·year and, in the case of near-maximal CP violation currently hinted at by T2K [84], 50% of these large CP-violating δ_{CP} values will be measured at 5σ confidence with an exposure of



(a) The significance with which the mass hierarchy can be determined as a function of the value of δ_{CP} for an exposure of 300 kt·MW·year assuming normal hierarchy (left) and inverted hierarchy (right). Taken from [88].



(b) Assuming normal hierarchy, the minimum significance (the lowest point on the curve in Figure 3.17a) with which the mass hierarchy can be determined for all values of δ_{CP} as a function of years of running under the assumptions in Table 3.2. Taken from [66].

Fig. 3.17 Sensitivity of the DUNE experiment to the neutrino mass hierarchy.

810 kt·MW·year, around 14 years of running following the staging described in Table 3.2. A full scope experiment operating with multi-megawatt beam power will eventually achieve around a 5% precision of the CP-violating phase, comparable to the equivalent precision in the quark sector described in the CKM matrix.

3.4.2 Oscillation Parameters

DUNE will make precision measurements of all parameters describing neutrino oscillations and improve our understanding of oscillation phenomenology. The least known mixing angle, θ_{23} , will be measured with a precision of at least 1° , even near 45° . This is possible by performing a combined analysis of the $\nu_\mu \rightarrow \nu_\mu$ and $\nu_\mu \rightarrow \nu_e$ channels, proportional to $\sin^2 2\theta_{23}$ and $\sin^2 \theta_{23}$ respectively (from Equations 2.31 and 2.30). The sensitivity of DUNE to the octant of θ_{23} , and the resolution of the value itself, is presented in Figure 3.19. The current world-leading measurements of θ_{13} from reactor experiments will also be achieved after sufficient exposure in the DUNE experiment, using analyses of ν_e and $\bar{\nu}_e$ appearance. The resolution of this, along with the anticipated resolution of the associated mass splitting, Δm_{31}^2 , are shown in Figure 3.20.

3.4.3 Other Physics

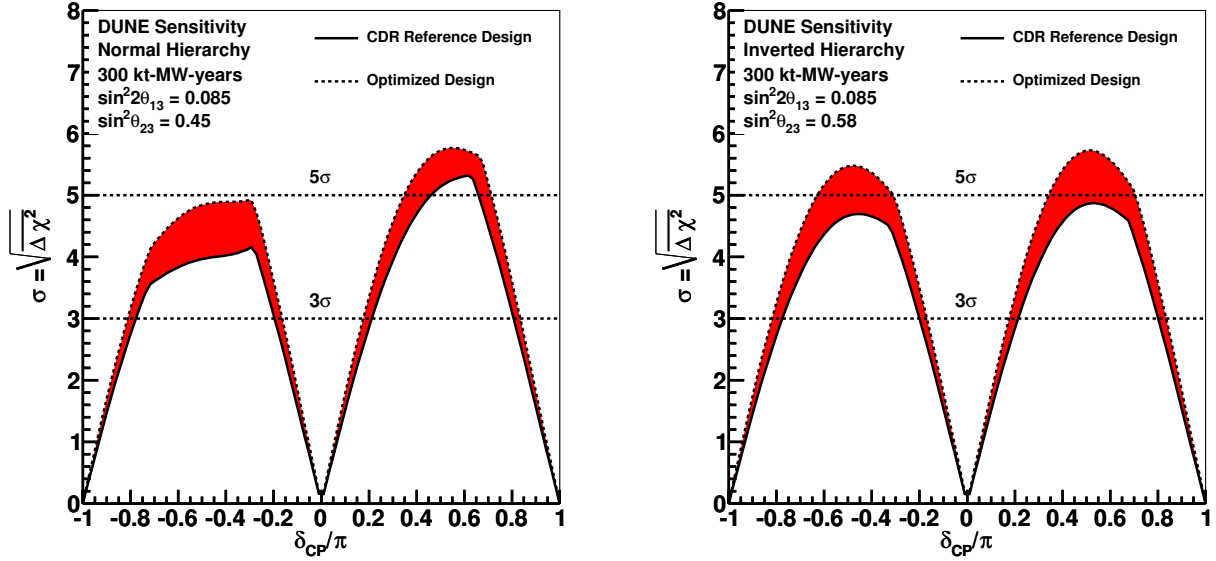
The LBNF/DUNE physics program is diverse and contains priorities unrelated to beam neutrino physics. These are not wholly relevant to this thesis and shall not be discussed in detail but it would be inappropriate to ignore the additional physics potential of the experiment.

The capabilities to search for nucleon decay, mainly via the $p \rightarrow K^+ \bar{\nu}$ channel, will improve lifetime limits by an order of magnitude after 20 years' running. It will significantly extend sensitivities compared to water Cherenkov detectors as a consequence of a higher detection efficiency and low background rates. Many models in which this mode is dominant (e.g. supersymmetric GUT models) also favour other models with final-state kaons, enabling a wide range of nucleon decay physics to be studied at the DUNE far detector.

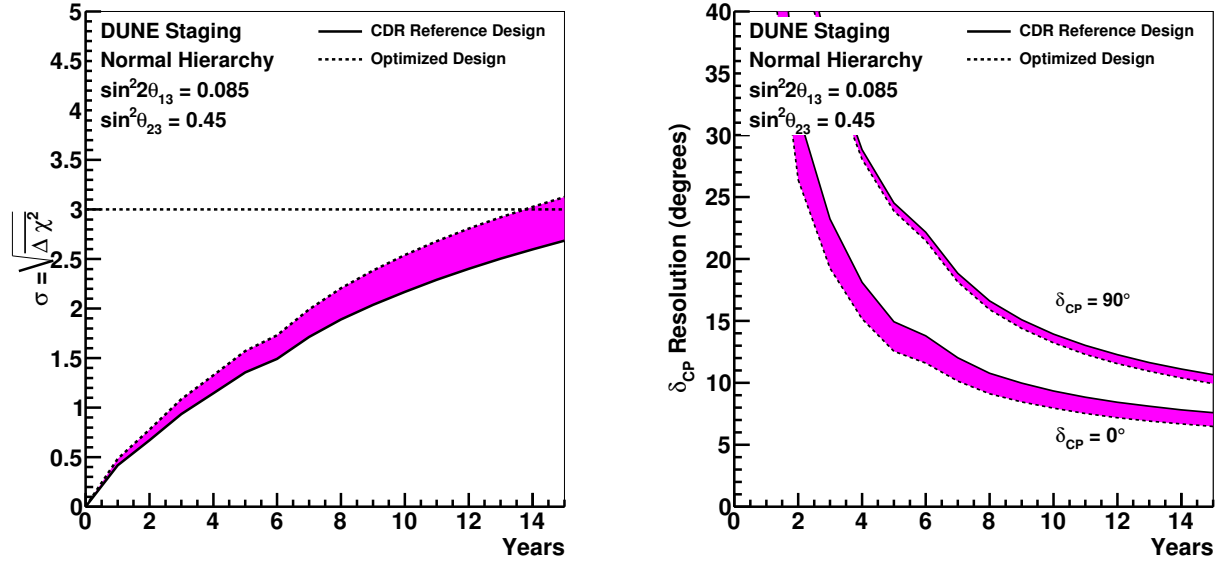
The unique sensitivity to supernova ν_e neutrinos, via the interaction

$$\nu_e + {}^{40}\text{Ar} \rightarrow e^- + {}^{40}\text{K}^*, \quad (3.1)$$

inaccessible to water or liquid scintillator detectors which detect the $\bar{\nu}_e$ component via inverse beta decay on free protons, will, along with $\bar{\nu}_e$ interactions, allow precision measurements of the composition of supernovae should one occur during the run of the experiment. The

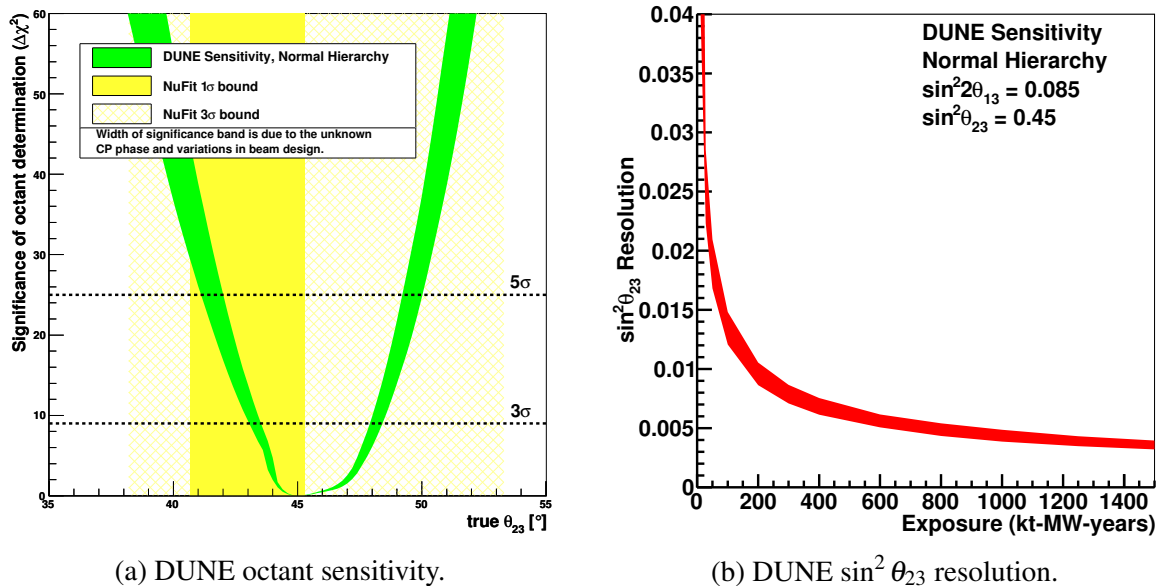


(a) The significance with which CP violation can be determined as a function of the value of δ_{CP} for an exposure of 300 kt·MW·year assuming normal hierarchy (left) and inverted hierarchy (right). Taken from [88].



(b) Assuming normal hierarchy, the significance with which CP violation can be determined for 75% of δ_{CP} values (left) and the expected 1σ resolution (right) as a function of years of running under the assumptions in Table 3.2. Taken from [66].

Fig. 3.18 Sensitivity of the DUNE experiment to leptonic CP violation.



(a) DUNE octant sensitivity.

(b) DUNE $\sin^2 \theta_{23}$ resolution.

Fig. 3.19 The sensitivity of DUNE to the octant and value of θ_{23} . Figure 3.19a shows the significance with which DUNE can resolve the θ_{23} octant as a function of the true value of θ_{23} . The green shaded band around the curve represents the range in sensitivity due to potential variations in the beam design and in the true value of δ_{CP} . The yellow shaded regions indicate the current 1 σ and 3 σ bounds on the value of θ_{23} from a global fit. An exposure of 1320 kt·MW·year, which will provide a 3 σ measurement of CP violation for 75% of the values of δ_{CP} is assumed. Figure 3.19b shows the resolution of a measurement of $\sin^2 \theta_{23}$ as a function of exposure assuming normal mass hierarchy and $\sin^2 \theta_{23} = 0.45$ from the current global fit. The shaded region represents the range in sensitivity due to potential variations in the beam design. Taken from [88].

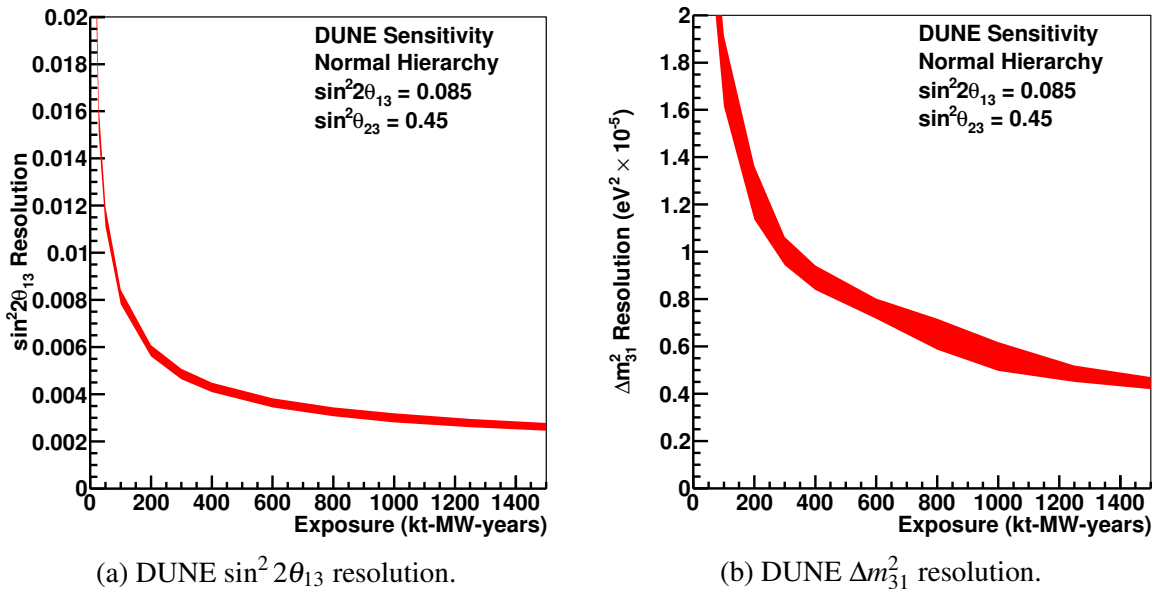


Fig. 3.20 The sensitivity of DUNE to the oscillation parameters describing ν_e and $\bar{\nu}_e$ appearance as a function of exposure assuming normal hierarchy. Figure 3.20a shows the resolution of a measurement of $\sin^2 2\theta_{13}$ and Figure 3.20b shows the resolution of Δm_{31}^2 assuming, from current global fits, $\sin^2 2\theta_{13} = 0.085$ and $\Delta m_{31}^2 = 2.457 \times 10^{-3} \text{ eV}^2$. The shaded regions represent the range in sensitivity due to potential variations in the beam design. Taken from [88].

neutrinos from a core-collapse are emitted supernova in a burst of a few tens of seconds, with around half the luminosity in the first second. They are roughly divided equally between the three known neutrino flavours and have energies between 5-50 MeV. A large neutrino signal from a supernova will allow unique studies of astrophysical phenomena related to the end of the lifetime of a star.

3.5 The Road to DUNE

The staging presented in Table 3.2 is hugely ambitious and requires a great deal of preparation to ensure the project is a success. The preparations have commenced with a program of prototyping and construction to ensure assembly of the first 10 kt module can begin as scheduled in 2021. Work at the far detector site is underway and construction at the near detector will start next year to ensure the beam and near detector facilities are ready for 2026.

Each 10 kt module is larger than any LArTPC ever operated by well over an order of magnitude and it is crucial the detector technology is understood and the experiment operates as expected. To ensure this is the case, a comprehensive prototyping strategy is planned. This will be briefly overviewed in this section.

3.5.1 The 35 ton Prototype

The first prototype to test many of the design features of the DUNE far detector was the 35 ton, shown in Figure 3.21. This is the subject of the majority of this thesis and will be properly discussed in Chapter 4. Lessons learned from the 35 ton experience are already influencing the design choices and operating schedules of the next prototypes and the far detector, highlighting the benefits of a thorough research and development program.

The 35 ton experiment demonstrated the cryostat and detector technologies over the course of two runs, in early 2014 and early 2016 respectively, by collecting and analysing data from cosmic-induced tracks and showers. Analysis of data from the second run is the subject of Chapter 7.

3.5.2 ProtoDUNE

The next prototypes, ProtoDUNE, will take data during the second half of 2018 and will be a full scale engineering prototype of the DUNE far detector. ProtoDUNE is hosted at the Neutrino Platform at CERN and consists of two demonstrators utilising single-phase (ProtoDUNE-SP) [107] and dual-phase (ProtoDUNE-DP) [108] designs. The layout is shown

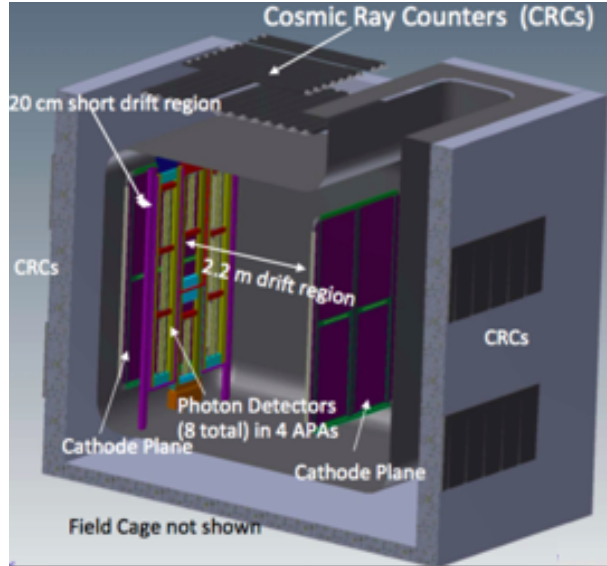


Fig. 3.21 Will replace this will a better image when I write the 35ton chapter. The 35 ton cryostat and detector designed to prototype the DUNE far detector design.

in Figure 3.22. The cryostats contain more than 700 t LAr and represent an intermediary stage between the 35 ton and the DUNE far detector modules.

The detectors are being constructed in a CERN test beam and will be subjected to various particles, including $e^\pm, \mu^\pm, K^\pm, p, \bar{p}$. Along with characterising the detector performance and identifying potential improvements, ProtoDUNE will provide calibrations, such as electromagnetic shower energy resolution, electron/photon separation and particle identification, for the far detector and facilitate an assessment of the detector systematics. It will also provide opportunity, in a detector functionally identical to the far detector modules, to validate the simulation and reconstruction techniques developed in Monte Carlo. Upon completion of the ProtoDUNE program, DUNE will be prepared to begin final preparations and construction of the first, single-phase, far detector module.

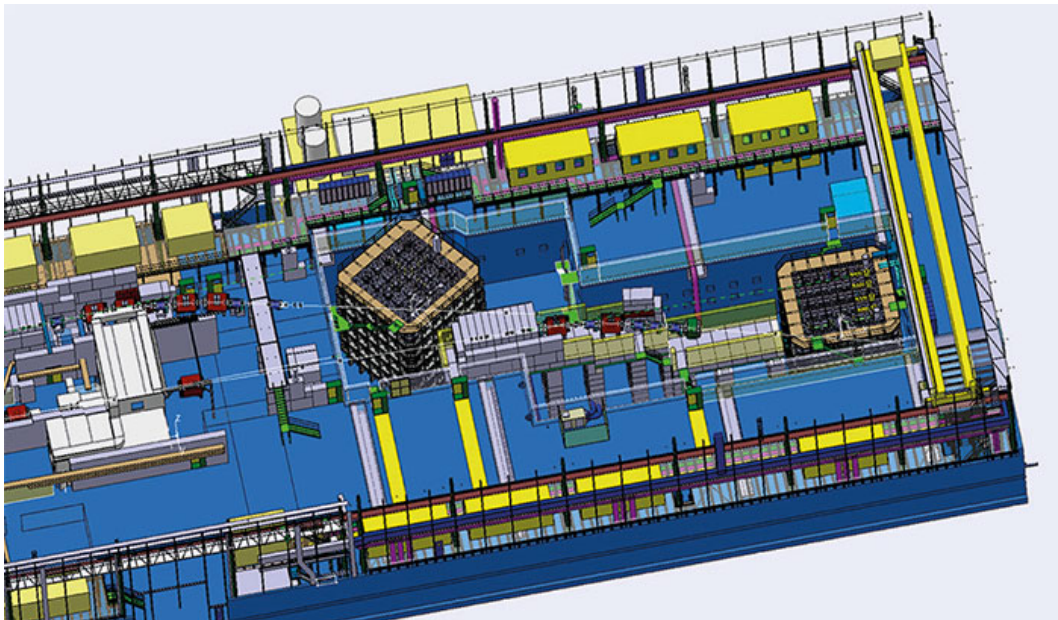


Fig. 3.22 Schematic showing the layout of the ProtoDUNE at the CERN neutrino platform [109]. The cryostat at the left, on a slight angle, is the dual-phase LArTPC and the single-phase detector is at the right hand side. The beamline, running from left to right through both detectors, is evident.

Chapter 4

The DUNE 35 ton Prototype

The 35 ton is a prototype experiment for the DUNE far detector design. It was constructed to prototype the unique design features of the LBNE far detector and was the only planned prototype for this detector. Following the dissolution of LBNE and the subsequent merging along with LBNO into the DUNE experiment, the 35 ton has become an integral part of the design and execution of the DUNE far detector design.

The 35 ton consists of a membrane cryostat (Sec. 4.3), designed to be filled with 35 metric tons of liquid argon, and a small-scale DUNE-style detector (Sec. 4.4) including a TPC and photon detectors. It was constructed in 2012 at PC4, a former proton facility in a decommissioned beamline, at Fermilab. The Phase I run, without a detector, took place between December 2013 and February 2014. Between February 2014 and September 2015 the detector was constructed and heavily tested at FNAL before being installed inside the cryostat ready for the Phase II run. This took place between February 2016 and April 2016 (officially starting on 11th February, as I type!).

4.1 Motivation

The use of liquid argon TPCs (LArTPCs) for the study of neutrinos in long-baseline experiments shows great promise and is the direction neutrino research, particularly in the US, is headed. Fermilab has an extensive program of LArTPC experiments to design, test and improve such detectors, culminating in DUNE, the flagship experiment due to come online in the early 2020s. Although they exhibit great physics potential, they do not come without significant engineering challenges. For example, DUNE will have four 10 kton cryostats containing liquid argon kept at very high purity. Constructing such a cryostat is itself difficult and expensive but in order to achieve, and maintain, the required purity, much R&D is required.

Previous LArTPC experiments, such as ICARUS [], Argoneut [], LArIAT [] and MicroBooNE [] (?), have been constructed as flat plane vessels and have used an evacuation method as the first step in removing atmospheric impurities which would contaminate the liquid argon. Constructing the DUNE far detector cryostats in a similar manner would be both very expensive and incredibly challenging. In order to investigate possible alternatives, the Fermilab program includes the Liquid Argon Purity Demonstrator (LAPD) and 35 ton experiments, together showing a cheaper and more feasible approach to designing and operating LArTPCs. These experiments are the subject of the present chapter.

4.2 The Liquid Argon Purity Demonstrator

The Liquid Argon Purity Demonstrator (LAPD) [110] was designed to demonstrate that the required purity of future LArTPC experiments is possible to achieve without the use of large scale vacuum pumps. The required mechanical capability of the cryostat to withstand such a method, along with the operation of the evacuation system itself, adds a considerable amount to the cost of the project. Suggestions to get around this include using multiple smaller scale cryostats, but this leads to greater complexity relating to both the engineering requirements of the piping infrastructure and the reconstruction capabilities of interactions spanning numerous fiducial volumes. LAPD successfully pioneered the method of using purging as the first step in purification of the liquid argon. This important result is discussed below and has significantly influenced the design of future LAr cryostats, including the 35 ton.

4.2.1 LAPD Experimental Setup

LAPD consists of a cylindrical tank (diameter 10 feet, height 10 feet) with a domed head capable of holding 32.6 tons of liquid argon. It is instrumented with cryogenic equipment and a purification system, consisting of two purifiers and a piping system. Figure 4.1 shows a CAD model of the tank and purification piping.

Insulation for the tank is provided by fibreglass sheets covering the outer volume which, along with the tank, is refrigerated by liquid nitrogen from an external supply. There also exist cooling coils near the top of the tank which serve to recondense vapourised argon and feed it back into the tank, via the filtration system.

The liquid argon is fed into the tank from outside PC4. The argon purity is maintained through the use of the purifiers, located outside of the main volume. Argon is constantly circulated from the tank to these vessels through stainless steel pipes. The filtration system

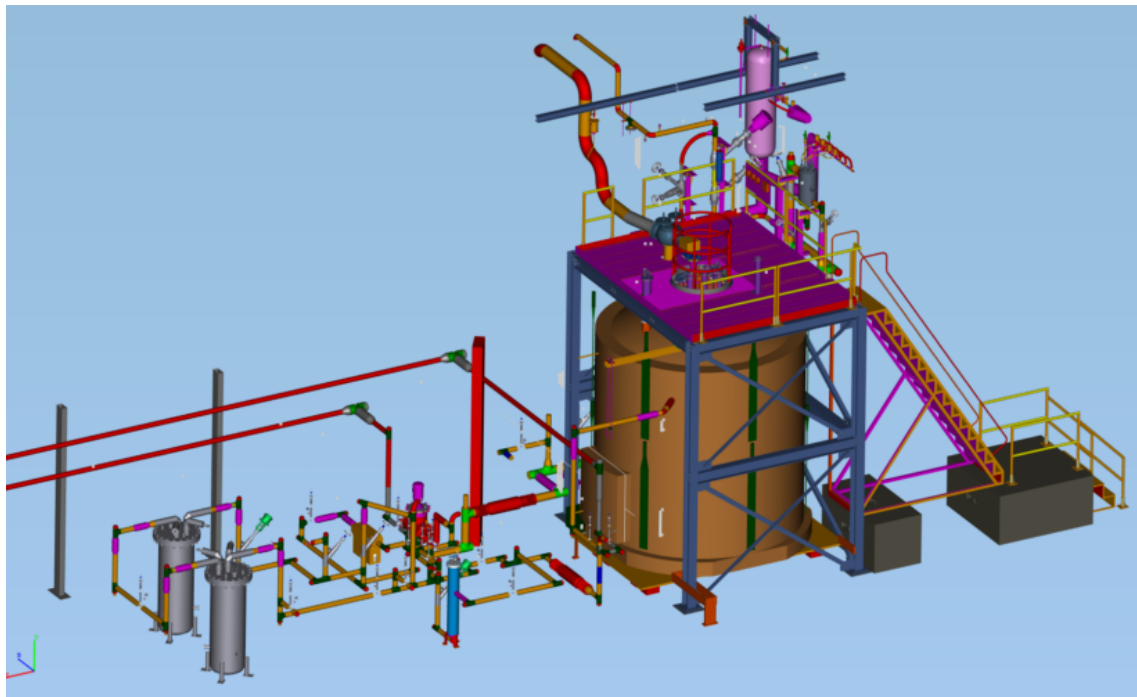


Fig. 4.1 The LAPD tank and purification system [110]. The domed tank on the right, beneath the platform, is the cryostat. The piping allow the flow of liquid argon into and out of the cryostat and is used as part of the purification system. Two cylindrical purifiers, visible in the lower left of the figure, remove contaminants from the argon as it is pumped through. All components of the experiment are discussed in the text.

used by LAPD, and subsequently by the 35 ton cryostat, is discussed in greater detail in section 4.2.2.

4.2.2 The LAPD Filtration System

A LArTPC relies on the detection of the drift electrons produced upon ionisation of the argon by a propagating particle. Electronegative contaminants in the medium jeopardise this process by recombining with the electrons before they can reach the readout electronics. The phase ‘electron lifetime’ therefore refers to the amount of time that an electron will typically drift along the electron field, and is directly related to the concentration of impurities in the liquid. Even using a modularised detector, as the DUNE far detector will be, drift lengths on the order of 5 m are realistically required, leading to purity requirements of several milliseconds. The dominant contaminants which are removed by the LAPD and 35 ton filtration system are oxygen and water.

The liquid argon is extracted from near the bottom of the tank and returned to the top after passing through the purifiers. It first passes through the water filter before continuing

on through the oxygen filter. The water filter comprises a molecular sieve which prevents the propagation of large molecules, such as water. This purification step must occur first since the proceeding filter also removes water molecules and would therefore be less efficient at removing oxygen if used first. The oxygen filter consists of a thin activated-copper layer on an alumnia substrate [111]. Both filters will lose some functionality over time as they collect more and more impurities and so require ‘regenerating’ in order to remove the contaminants. This can be done in-situ, as described in [111]; this complicates the design of the filter but is necessary when considering the purification system required for the full DUNE far detector.

The contamination gradient, and associated purities at each stage during the LAPD Phase II run, is shown in figure 4.2. These purities are known through the use of purity monitors; these are the subject of section 4.2.3.

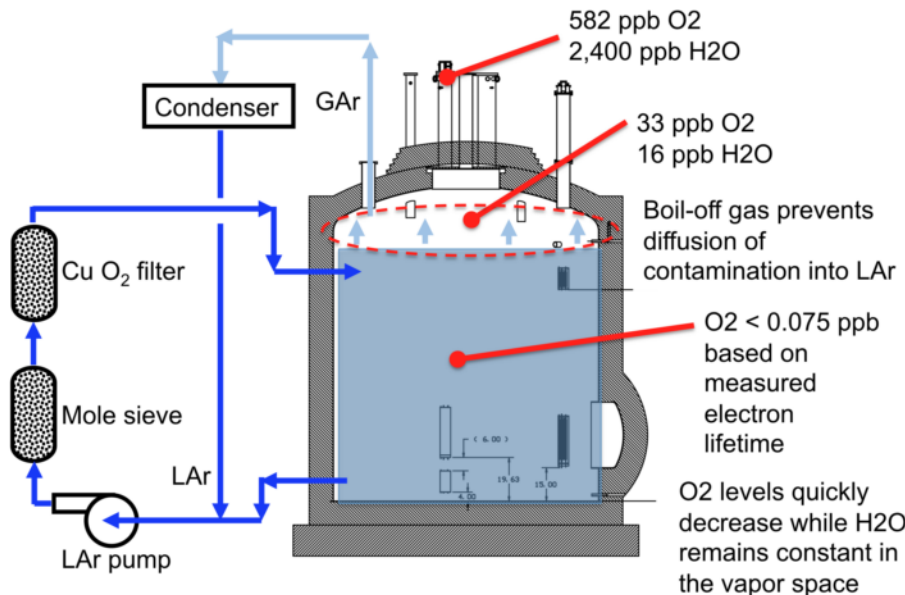


Fig. 4.2 Contaminant gradient in the LAPD tank at different stages of the purification process [110]. The associated LAr purities, in units of parts-per-billion (ppb) are also shown.

4.2.3 Purity Monitoring

As discussed in section 4.2.2, extreme LAr purity is required for the successful readout of ionisation electrons by the electronics. These purities must be constantly monitored to ensure the high quality of argon necessary during data taking. Since these impurity concentrations are beyond the capabilities of many conventional gas analysers, a device called a purity monitor is employed. Such a device is shown schematically in figure 4.3.

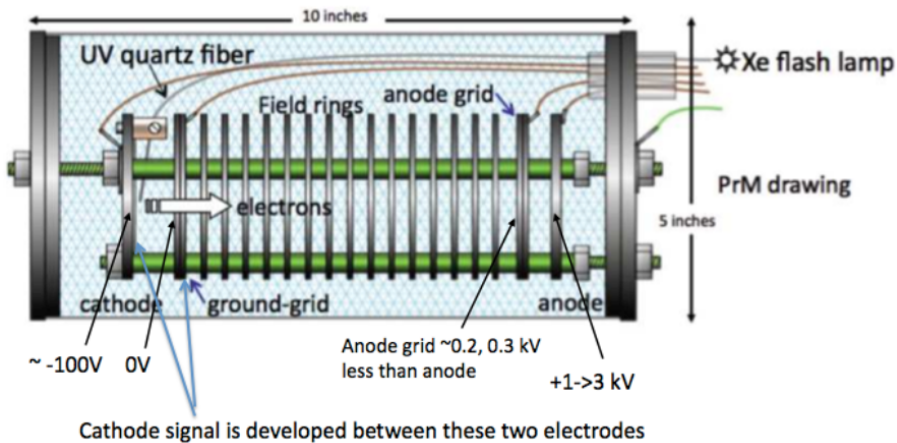


Fig. 4.3 Diagram showing schematically the design of purity monitor used in LAPD, and subsequently the 35 ton experiment [112]. Their use is described in the text.

The purity monitors deployed consist of a cylindrical volume, filled with LAr for its surrounding environment. They contain a photo cathode and an anode, between which lies short drift volume. When taking purity measurements, light from a Xenon flash lamp is incident on the cathode, liberating photoelectrons which traverse towards the anode. Electronegative impurities in the LAr will decrease the electron lifetime and therefore the mean number of electrons reaching a certain point along the drift volume. A measurement of the ratio of the charge arriving at the anode to that at the cathode is hence a measurement of the inherent purity of the liquid.

These monitors were placed both in the LAPD tank and just after the filtration system in order to study the purity at different points in the recirculation. Several gas analysers, measuring nitrogen, oxygen and water contaminants to various levels of accuracy, were also used. Temperature sensors to measure the vertical temperature profile within the cryostat were necessary to account its effect on the electron drift velocity.

Several of the technologies pioneered in LAPD were also used in the 35 ton experiment, as will be shortly discussed.

4.2.4 LAPD Results

LAPD successfully demonstrated achieving and maintaining the required LAr purity for a large neutrino detector is possible without the costly and challenging use of evacuation techniques. It initially ran for six weeks and reached a purity of better than 60 ppt (parts-per-trillion) oxygen equivalent [110]. The measured electron lifetimes over the course of the run

is shown in figure ???. As can be seen, electron lifetimes of up to 4 ms were reached, which is [put into context with current DUNE requirements!].

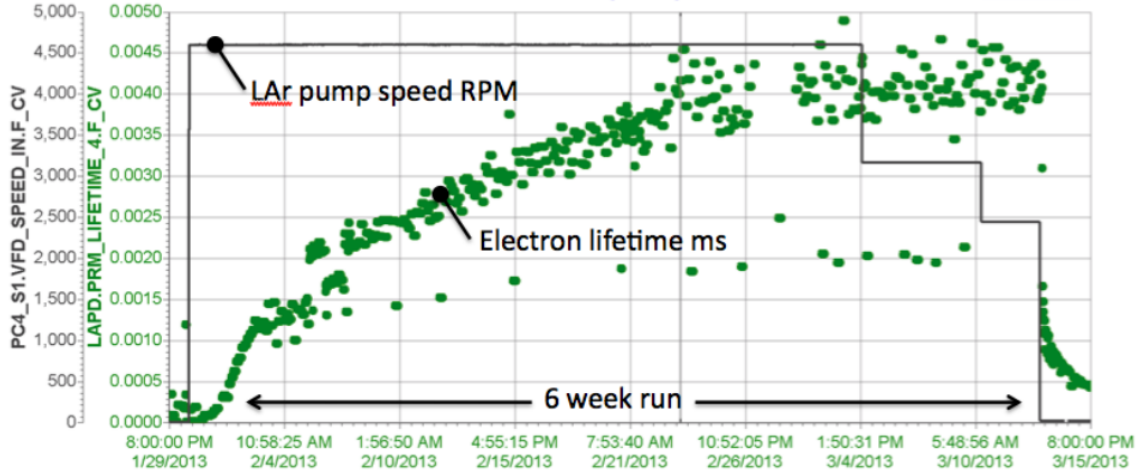


Fig. 4.4

This important result has great significance when considering future LArTPC experiments and laid the way for the 35 ton experiment. This experiment will now be discussed in the subsequent sections.

4.3 The 35 ton Cryostat

The 35 ton prototype takes advantage of membrane cryostat technology and is the first test of this construction technique for LArTPCs. Membrane cryostats have been widely used in the liquified natural gas industry for many years but the 35 ton experiment is the first to make use of the technology for liquid argon. Furthermore, it is the first membrane cryostat to be constructed in the United States and the first to be constructed for scientific purposes [113]. The 35 ton cryostat is the subject of the present section.

4.3.1 Construction

Boring stuff about cement and shit.

Cryostat!

4.3.2 The 35 ton and LAPD

It's near LAPD!

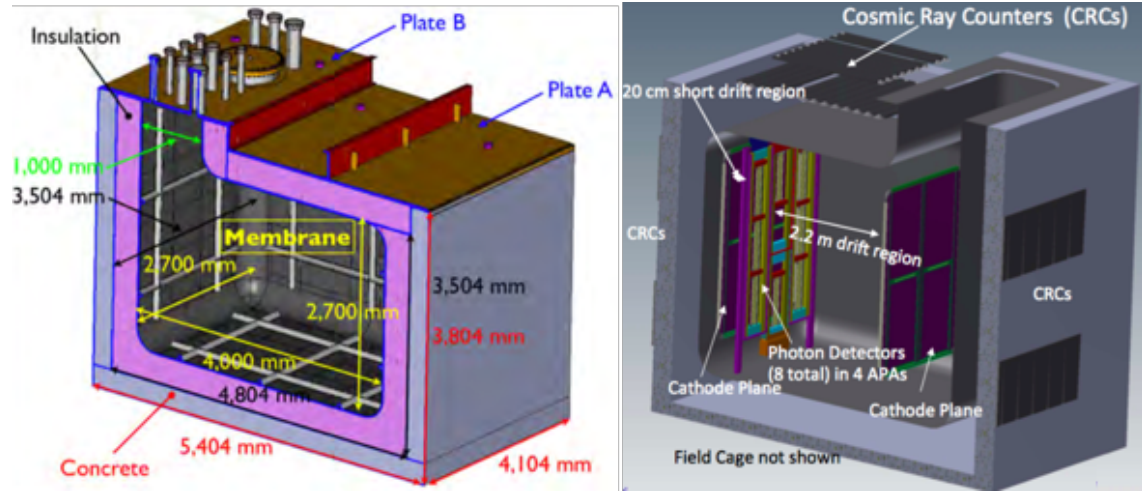


Fig. 4.5 The 35 ton cryostat [112]. The cryostat as operated during Phase I is shown on the left and the corresponding version, including a full small-scale detector, used in Phase II is on the right.

4.4 The 35 ton Detector

In 35t, we have FE ASICs which are the very front end and apply the signal shaping and gain. Have regulators to control the power these receive (these are noisy...). Also ADC ASICs to do digitisation in the cold. MicroBooNE don't do this, this just have the front end and do everything else in the warm. FE ASICs are the problem, same for uBooNE and 35t. ADC ASIC has stuck code problem.

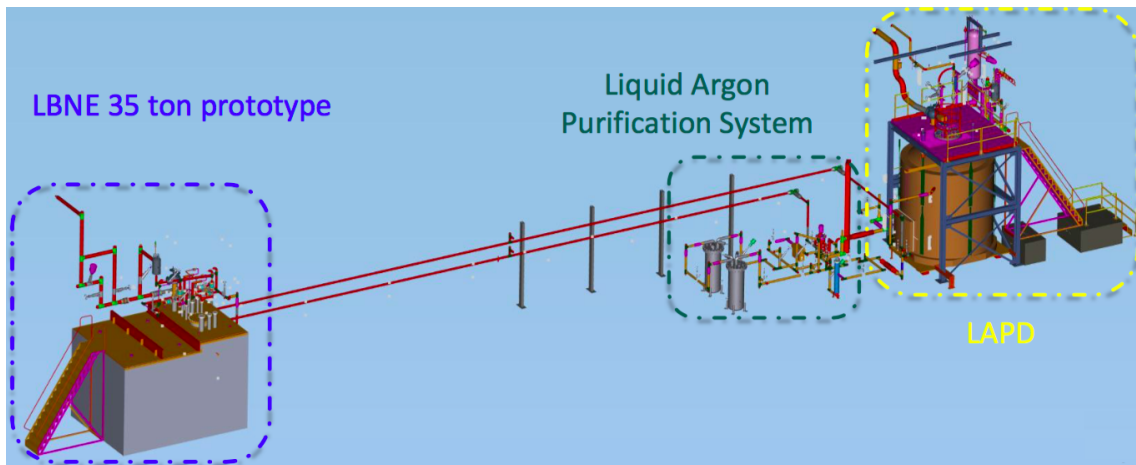


Fig. 4.6 [112].

4.4.1 Detector Components

4.4.1.1 TPC

4.4.1.2 Photon Detectors

4.4.1.3 External Counters

4.4.2 Readout Electronics

4.4.2.1 FEMBs

4.4.2.2 RCEs

4.4.2.3 SSPs

4.4.2.4 PTB

4.4.3 DAQ

4.5 Filling the 35 ton

4.6 The 35 ton Experimental Setup

4.6.1 Filtration System

Same as LAPD.

4.6.2 Purity Monitoring

Same as LAPD.

4.7 35 ton Phase I

4.7.1 Outcomes

4.8 35 ton Phase II

4.8.1 Commissioning

4.8.2 The Sheffield Camera System

Wait for Nicola to finish the paper and plagerise!

4.8.3 Online Monitoring for Data Quality Monitoring

4.8.4 Outcomes

Chapter 7

Analysis of 35 ton Data

Could this chapter be a little more specifically titled?

The 35 ton run (see Section 4.8) provided 22 days of good quality (high purity, stable field (250 V/cm), stable DAQ), analysable data. Due to the issues encountered, high quality physics analyses proved very challenging and instead studies, particularly those presented here, focused on trying to understand the detector and characterise previously untested responses. In this respect, the 35 ton proves to be a vital experiment in informing the next generation of prototypes and even the final DUNE far detector design. It also boasts datasets which no planned experiment will before the full DUNE modules; it is therefore essential as much information as possible is extracted from the 35 ton analyses.

Before analyses are presented, techniques developed to enhance the quality of the data, and the data selection, will be discussed in Section 7.1. A short section demonstrating how LAr purity may be determined from data is contained in Section 7.2 before the main analyses, concerning tracks passing across APA gaps and through the APA frames, are presented in Section 7.3 and Section 7.4 respectively. Finally, a brief investigation into the performance of basic shower and calorimetric reconstruction on the 35 ton data is discussed in Section 7.5. A summary is provided in Section 7.6.

7.1 Preparing 35 ton Data for Analysis

To ensure analyses are as accurate as possible, careful pre-selection and preprocessing of the data is performed. Methods for producing the analysable sample are discussed in the section.

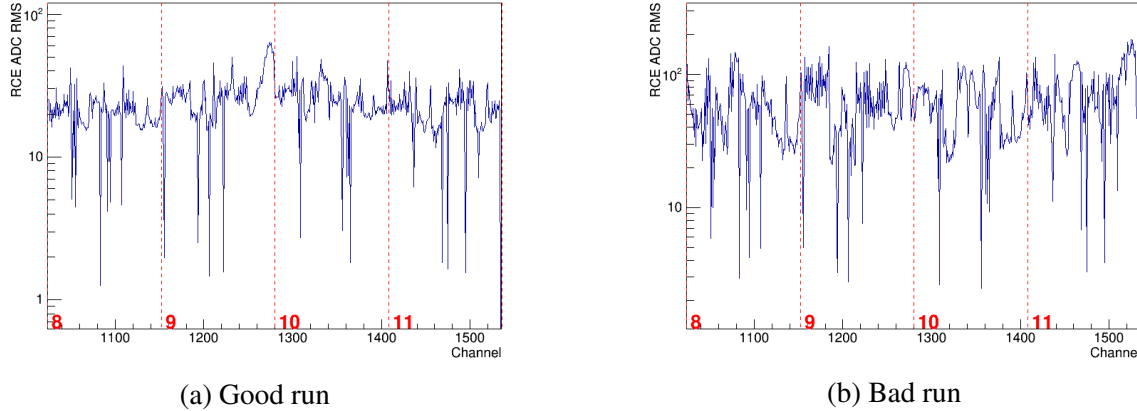


Fig. 7.1 Comparison between noise levels for ‘good’ and ‘bad’ 35 ton runs. The channels shown are on APA2 (online convention, APA0 offline) and are read out by RCEs 8 through 11 (labelled). The increase in read out charge RMS is evident in the case of the noisy run. These plots are from runs 15797 (Fig 7.1a) and 15790 (Figure 7.1b) and were taken only 50 minutes apart.

7.1.1 Selecting the Data

The level of noise present in the TPC data varied hugely between runs – this is evident from analysing the RMS of the charge read out on a particular channel. Figure 7.1 shows a comparison of this metric for ‘good’ and ‘bad’ runs.

Runs which exhibited the lowest noise were selected for analysis. In all there were 1269 runs used representing some data taken before the FNAL site wide power outage (3rd March 2016) with most the week after stabilising the experiment again (9th March – 17th March). A selection of bad channels, classified as either ‘dead’ (electrically) or ‘bad’ (exhibit sufficiently more than average noise), represent 8% of the total number of channels.

Due to the continuous nature of data taking, there is a non-trivial correlation between a ‘DAQ event’, a collection of fragments read out by the DAQ, and a ‘physics event’, an event in which particle interactions occurred. The external triggers used in the 35 ton, namely the external muon scintillators and the photon detectors, are used to define the event time. Given the trigger rate at which most data was taken (~ 1 Hz), a typical run comprising a few thousand events will only contain $\mathcal{O}(10)$ triggered events. Furthermore, given the data format, these events often straddle multiple DAQ events (refer to Figure 6.5 for a demonstration of this). A splitter/stitcher module is employed to search for triggers within runs and construct physics events containing the useful information for analysis. This produces a file with just this relevant information, which are then used for analysis.

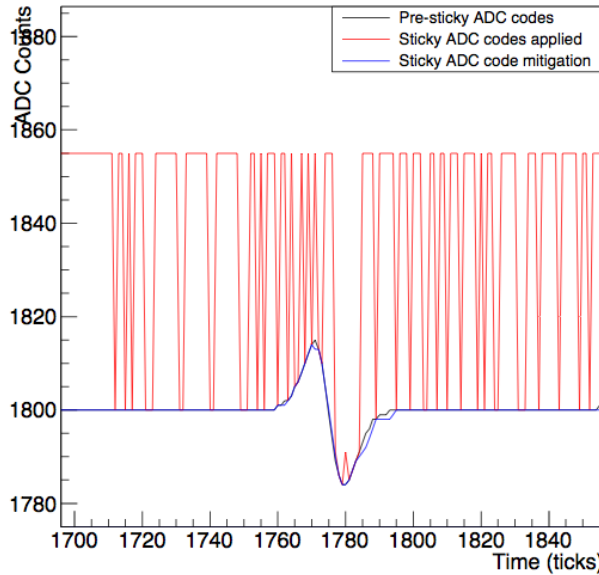


Fig. 7.2 Simulated demonstration of the method used to correct for stuck codes in the 35 ton data. On a given channel, ADCs exhibiting the consequences of this problem are corrected by interpolating charge at neighbouring time units. This is tested by simulating a waveform and adding the observed stuck code effect; the efficacy of the method at correcting the afflicted bits can then be evaluated.

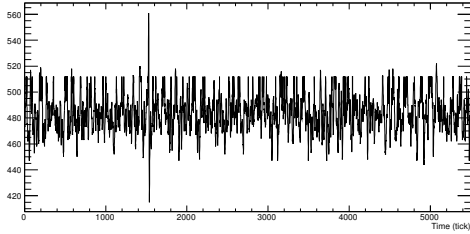
7.1.2 Improving Data Quality

Two issues present in the raw data, namely the presence of correlated noise and the stuck bits in the digitiser, are dealt with as an initial step of the reconstruction. First, an algorithm attempting to correct for the stuck bits analyses waveforms on a wire and identifies problematic ADCs; interpolating between charges read out at neighbouring times is successful at reconstructing the initial waveform in most cases. Figure 7.2 demonstrates this interpolation method on simulated data. The effect of applying this algorithm on a full waveform, to correct for all the stuck bits, is apparent in Figure 7.3.

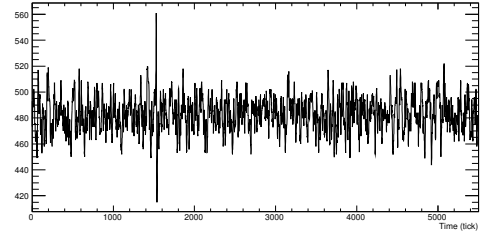
Following this process, a coherent noise removal stage is applied. This simply looks at the average noise across channels sharing a front-end voltage regulator and removes this component from the readout ADC for each channel. The effect of this correction is seen in Figure 7.4.

7.1.3 Reconstructing Muon Tracks

All analyses discussed below only make use of information recorded on the collection planes. Since the induction wires are longer (a necessity for wrapping), a larger capacitance results in higher noise levels, complicating the reconstruction. In general, after applying the

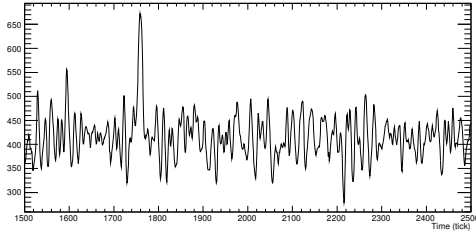


(a) Raw waveform before correcting for stuck bits.

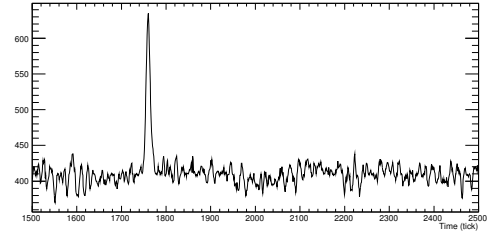


(b) After applying stuck bit mitigation.

Fig. 7.3 The effect of applying stuck bit mitigation to a waveform as seen in raw data. This particular waveform is from run 15660, channel 722 (induction channel).



(a) Waveform before removing coherent noise.



(b) After removing coherent noise.

Fig. 7.4 The effect of removing coherent noise from all channels on a voltage regulator. This waveform is from run 15660, channel 2010 (collection channel). The signal is noticeably larger following this process, considerably improving reconstruction performance.

refinements outlined in Section 7.1.2, the signals on the collection channels are prominent enough for competent analyses. The methods used to select tracks are described in this section and applied during the subsequent studies.

Using only the collection plane presents challenges, the most obvious being the impossibility of full 3D reconstruction. A hit on a collection wire at a given time gives well-defined x and z coordinates but cannot give any information in the y -direction. ‘Quasi-3D’ reconstruction is achieved by making use of the external counters. Through-going muons are triggered by the coincidence of hits in two opposite counters; this information can be used to give a crude handle on the y position of hits.

Figure 7.5 outlines the stages of selecting hits originating from the particle track which caused the trigger. Figure 7.5a shows all hits from an example event containing a through-going muon. The first stage of track selection involves taking those hits which lie in the ‘counter shadow’, the narrow section of collection plane area physically inbetween the opposing counters through which the triggering particle passed. The hits which remain are shown in Figure 7.5b. The track hits are visible along with further, unrelated hits. These are removed by requiring that only hits on wires with single occupancy be kept, and then applying a linear fit and removing all hits with residual > 2 cm. The final output after these stages is shown in Figure 7.5c.

The result of this track selection, as evident from Figure 7.5c, is a well-formed, high quality track with which it is possible to perform analyses. These will be the focus of the remainder of this chapter.

7.1.4 Preparing Simulated Data

Comparisons with simulated data are often essential in understanding various phenomena in the data. Throughout the analyses presented in this chapter, simulations were used to aid investigations and therefore it is important to ensure the Monte Carlo is as similar to the real data as possible.

The standard LArSoft simulation tools were used as described in Section 5.1, employing the CRY cosmic ray generator. The data passing through the detector was filtered on counter coincidences, exactly as the raw data is triggered. The simulated data was then processed in the same way as the real data and reconstructed using the methods described in Section 7.1.3.

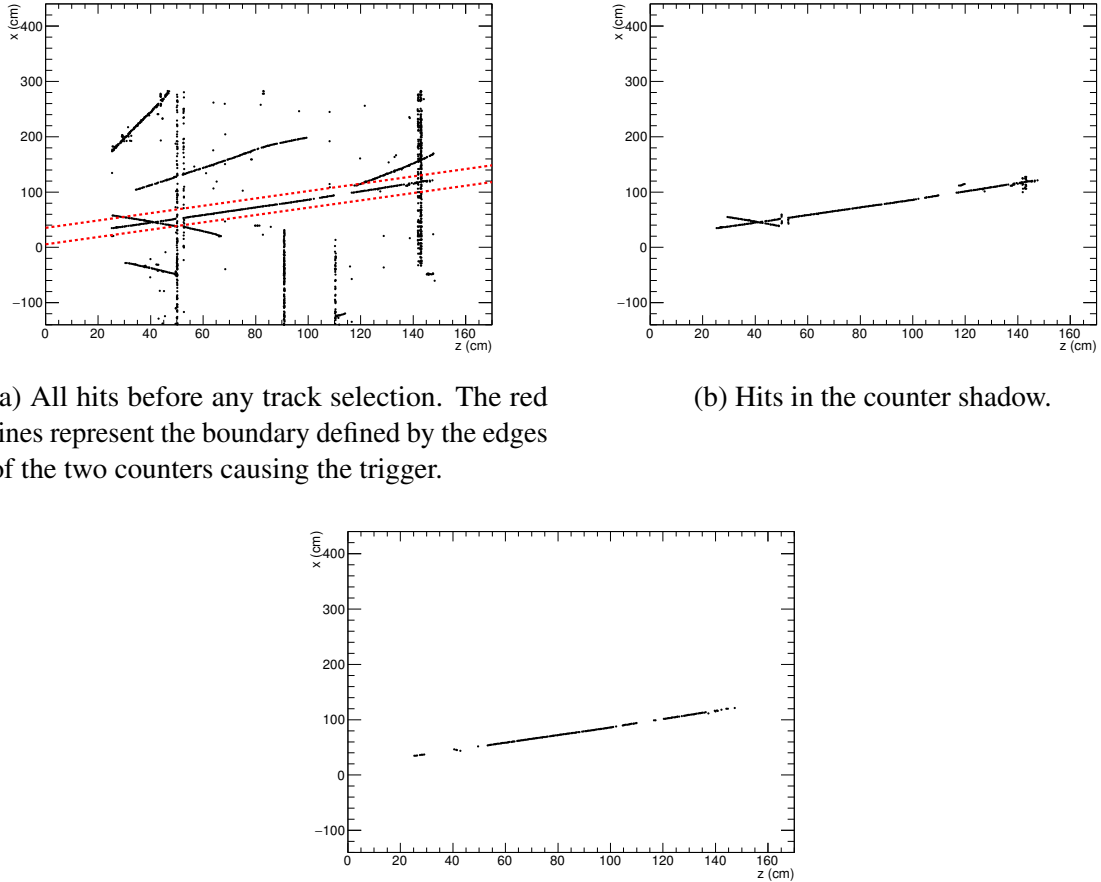


Fig. 7.5 Demonstration of the successive stages applied to hits on collection wires in order to select hits from the through-going track associated with the particle which caused the trigger. The hits left after all stages are taken forward into the analyses.

7.2 LAr Purity from Crossing Muons

The purity of the liquid argon is directly related to the concentration of electronegative impurities present in the medium which may capture drift electrons before they reach the anode planes. This gives rise to the concept of ‘electron lifetime’, τ , which affects the charge $Q_{\text{collected}}$ collected by the readout wires;

$$Q_{\text{collected}} = (Q_{\text{ionised}} - Q_{\text{recombination}})e^{-t/\tau}, \quad (7.1)$$

where Q_{ionised} is the ionised charge, $Q_{\text{recombination}}$ is the charge lost due to initial recombination with the position ion and t is the drift time of the charge packet.

It is possible to make a rough measurement of the electron lifetime directly from crossing muon tracks and two complimentary methods are reported here – using hits from single tracks which make a large angle to the APA frames and using multiple tracks parallel to the APAs binned into discrete drift distances. These are described in Sections 7.2.1 and ?? respectively. The analysis here serves mainly to demonstrate how these measurements are made and to produce preliminary results; a rigorous assessment is a in-depth study in itself and is not attempted in this thesis.

7.2.1 Single Track LAr Purity Measurements

7.3 APA Gap-Crossing Muons

One of the primary motivations for the design of the 35 ton TPC was to test its modular form, where a single drift region is read out by multiple anode assemblies. Particles passing through the detector will inevitably leave deposits in multiple TPCs and will pass uninstrumented regions of the detector, such as gaps in between neighbouring APAs. Many APA gap-crossing tracks are evident from the event display in Figure 7.6 and an example such track is demonstrated schematically in Figure 7.7. It is essential the implications of this design choice are understood before constructing the far detector modules, each of which will contain 150 APAs.

The 35 ton dataset consisting of muons which pass across the face of APAs and therefore deposit charge in consecutive TPCs is discussed in this present section. An analysis of these tracks to calculate the size of the gaps is presented in Section 7.3.1 and a study of the charge deposited by such tracks is the subject of Section 7.3.2.

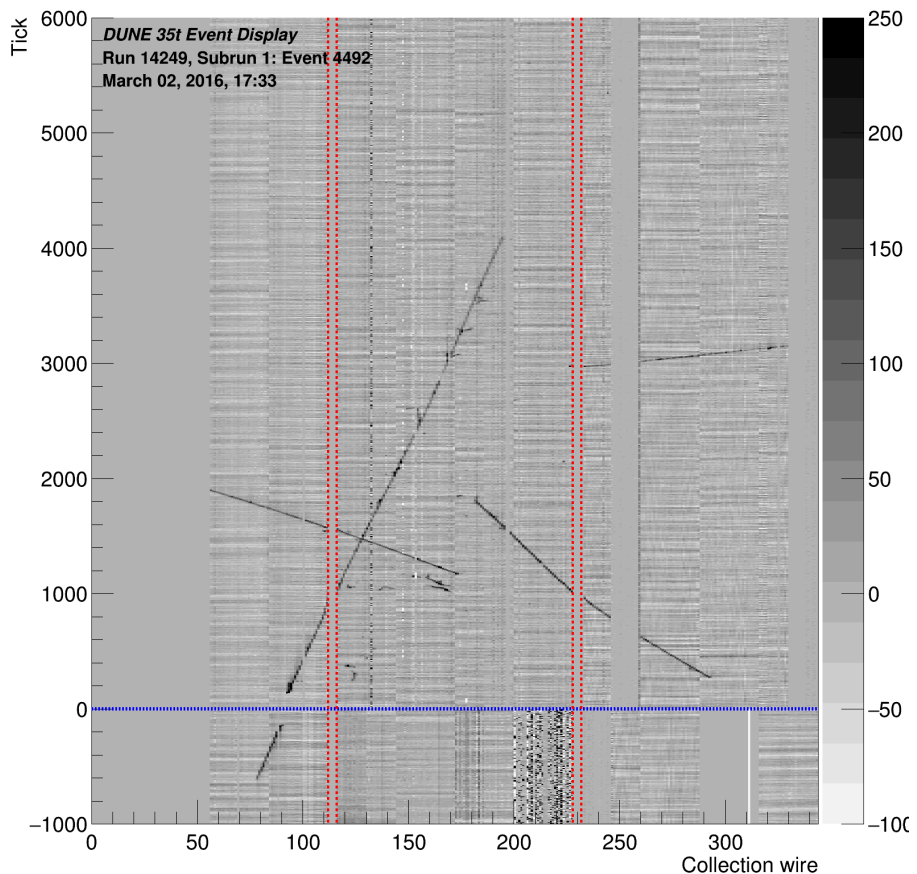


Fig. 7.6 Event display showing tracks passing across APA gaps and also through the APAs. A study of the tracks which pass across gaps between the APAs (the red lines) is the subject of Section 7.3. There is a visible offset apparent as the track crosses through the APAs (the blue line); correcting for T0 would eliminate this and yield a single accurately connected track. This is discussed further in Section 7.4.

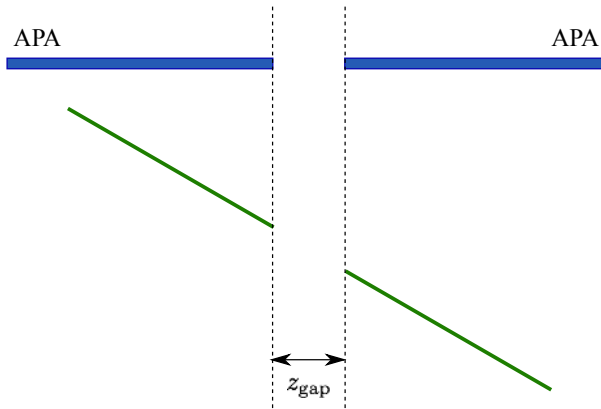


Fig. 7.7 Schematic showing an example APA gap-crossing track as viewed looking down from the top of the detector. The vertical direction represents the drift direction (x); the horizontal direction represents the z -direction. In general, these tracks make an angle with respect to the face of the APAs, as shown in the figure. As the gap in between the APAs is uninstrumented, no charge is deposited in this region.

7.3.1 APA-Gap Offset Determination

It is possible to use these gap-crossing tracks to make measurements of the gaps between each of the APAs. This involves aligning the track segments from neighbouring TPCs, demonstrated in Figure 7.8. The value of the z -offset, Δz , is determined by considering a range of offset hypotheses, performing a linear fit and finding the offset which minimises the residual least squares

$$L = \sum_i^{nhits} (o_i - e_i)^2, \quad (7.2)$$

where $o_i - e_i$ is the distance from hit i to the best fit line.

There are eight gaps which can be measured from the data, demonstrated in Figure 7.9. Due to very low statistics, it was found measurements of the gaps on the short drift volume side of the APAs were not possible using the 35 ton data. Analysis of the gaps using tracks passing through the long drift volume, hereafter named TPC1/TPC3, TPC1/TPC5, TPC3/TPC7 and TPC5/TPC7, was therefore the focus of this study.

A number of cuts were applied to ensure only high quality tracks were included for analysis:

- Only hits greater than 1 cm and less than 15 cm away from the gap were included in the track segments. The purpose of this cut is to limit the effect of multiple scatterings and the poorly understood region closest to the gap, where charge deposited in the uninstrumented region may later be collected.

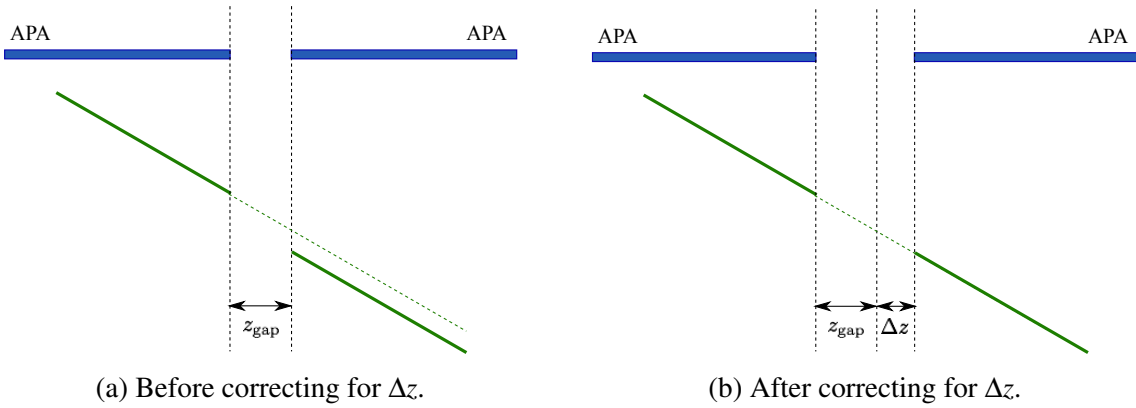


Fig. 7.8 Schematic showing an example track crossing two drift regions offset by an unknown quantity Δz . The effect of this is evident from the track deposits (Figure 7.8a) and can be corrected by ensuring the segments are aligned between the TPCs (Figure 7.8b).

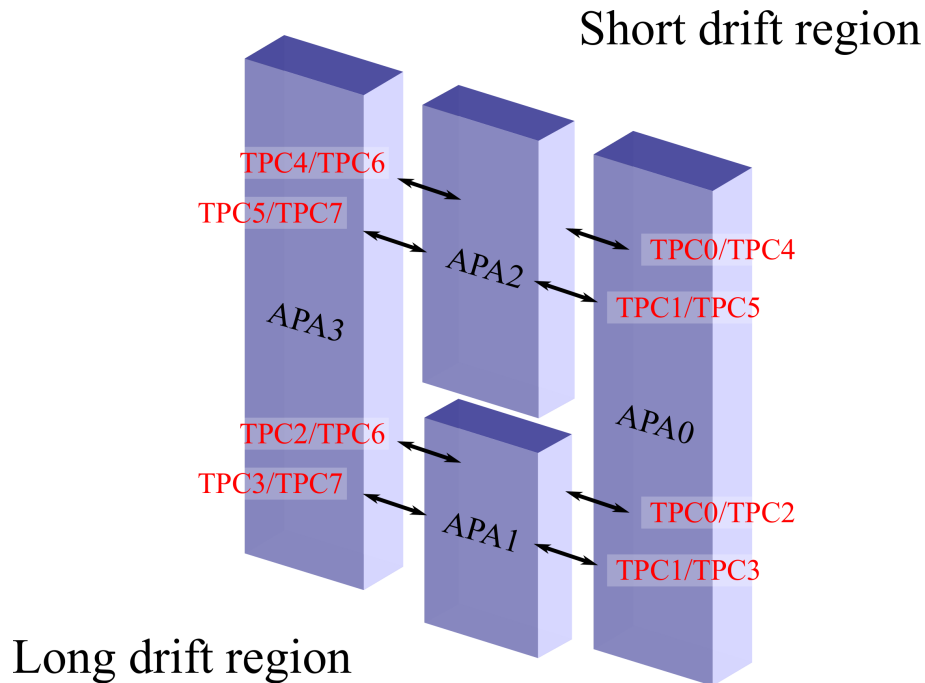


Fig. 7.9 Illustration of the eight gaps between the four APA frames.

- Each track segment must contain at least ten hits to allow an accurate measure of the gradient.
- The angle between the track segments either side of the gap must be less than 2° to remove any poorly reconstructed tracks, or segments originating from different particle tracks.
- The angle the track makes with respect to the APA face must be large enough that the gap offset effect can be measured to an acceptable accuracy. It is common in the 35 ton to refer to a ‘counter gradient’, the offset between the two counters forming the through-going particle trigger in the drift direction, in units of counter length (refer to Figure ??). The tracks must have a counter gradient of at least three.

7.3.1.1 Measuring the APA Gaps

The gap which may expect the largest number of crossers is TPC5/TPC7 and so the method will be demonstrated using data from this channel. The z -offset determined using the method and cuts described above is shown in Figure 7.10. An unexpected feature is evident from this distribution; there is not a single peak but two, seemingly related to the angle which the through-going particle makes with respect to the APAs.

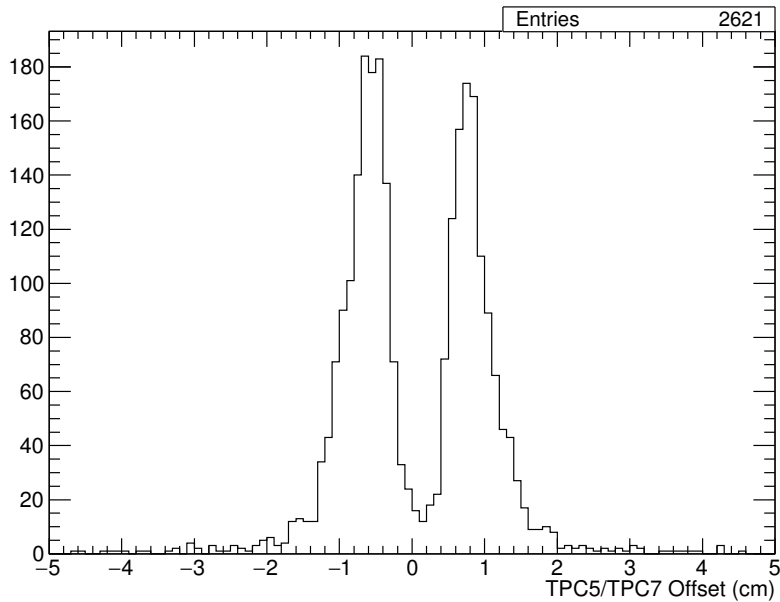
One explanation for this observed double-peak effect involves considering the possibility of additional offsets from the assumed positions of the APAs. This is demonstrated in Figure 7.11. It appears an offset in the x -position of the APAs could result in the problems encountered in the data. In order to test this, these offsets were artificially introduced into the simulation; the findings are presented in Figure 7.13. It appears the distribution of Δz measured from the data is consistent with APAs with offsets from expectation in both x and z . Moreover, it may be possible to measure both offsets from the same data set.

It is clear from Figure 7.13 that the z -offset may be determined as the minimum between the angular-separated distributions. This can be justified by geometrical considerations, explained in Figure 7.14. In this case, this may be achieved by fitting a function of the form

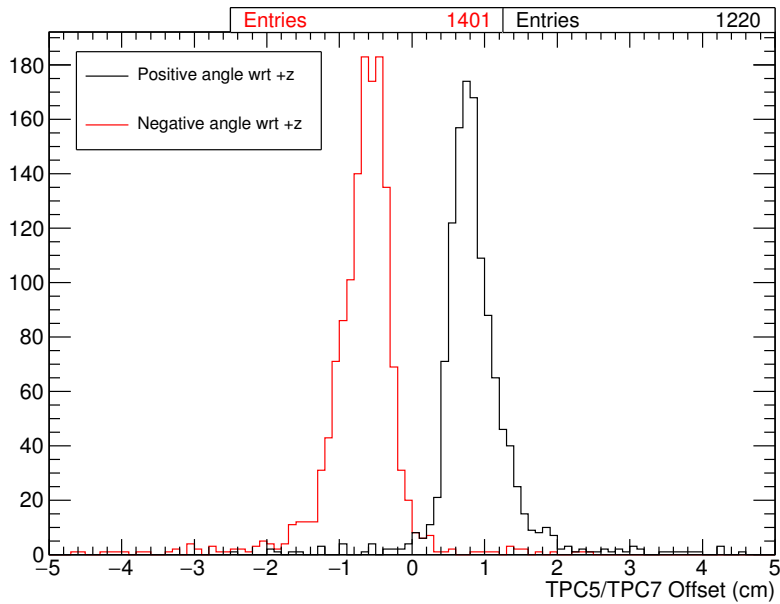
$$f(x) = a(x - b)^2 + c \quad (7.3)$$

and extracting parameter b as the true value of Δz . This is shown in Figure 7.15.

Using this measured value of Δz , the offsets can be analysed again, this time measuring the x -offset by correcting for the z -offset. The measured x -offset distribution is shown in Figure 7.16. With this value of Δx , the z -offset can be evaluated once more to ensure the distribution contains a single peak, as initially expected. This is confirmed in Figure 7.17.



(a) Full distribution.



(b) Separated by the angle the track makes to the APAs.

Fig. 7.10 The z -offset for the TPC5/TPC7 gap measured in the 35 ton data. A very noticeable double-peak structure is evident in Figure 7.10a; this bias appears to be related to the sign of the angle the particle track makes to the APA planes.

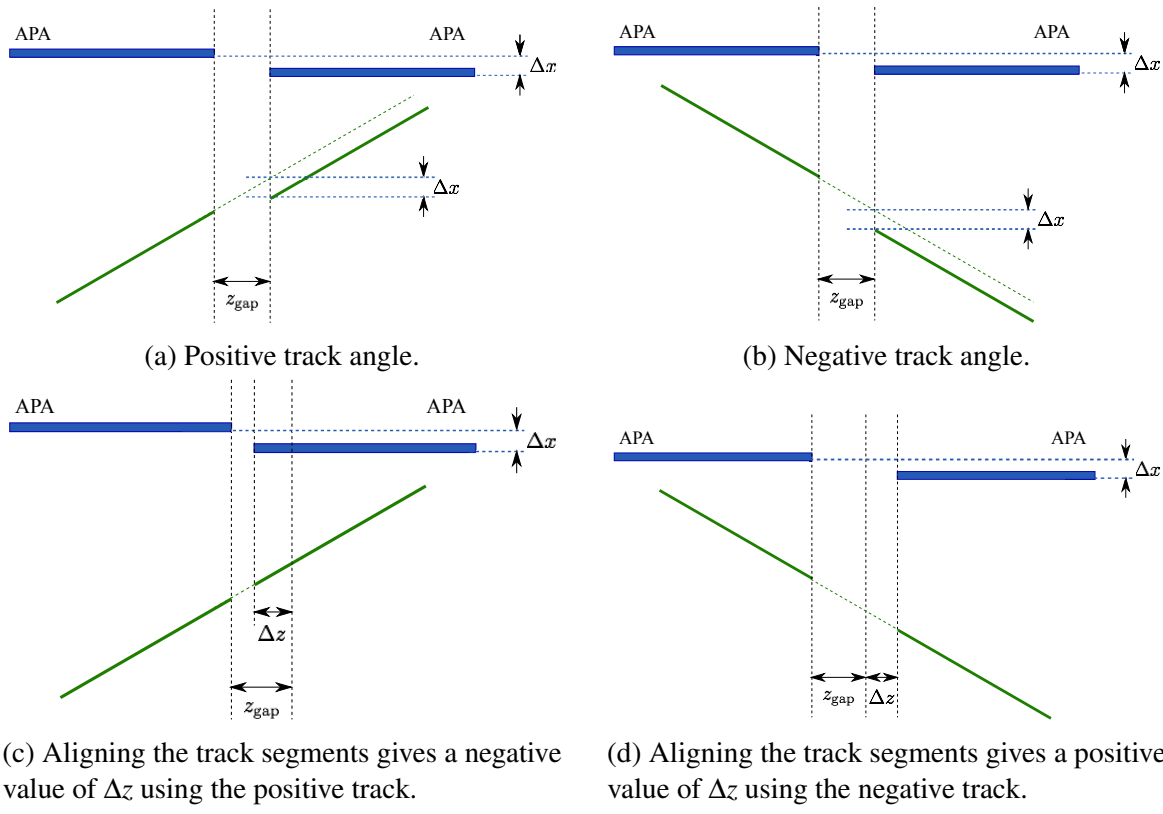


Fig. 7.11 Demonstration of how an x -offset in the positions of the APAs can explain the degeneracy evident in the z -offset measured using the 35 ton data (Figure 7.10). In the left-hand plots, Figures 7.11a and 7.11c, the through-going particle makes a positive angle to the face of the APAs and in the right-hand plots, Figures 7.11b and 7.11d, the particle is travelling with a negative gradient. In both cases, the offset of the APAs in the x -direction is the same. It is clear from Figures 7.11c and 7.11d how the sign of the measured Δz is dependent on the angle of the track.

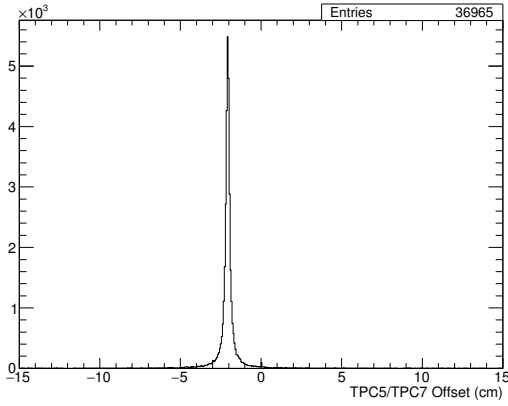
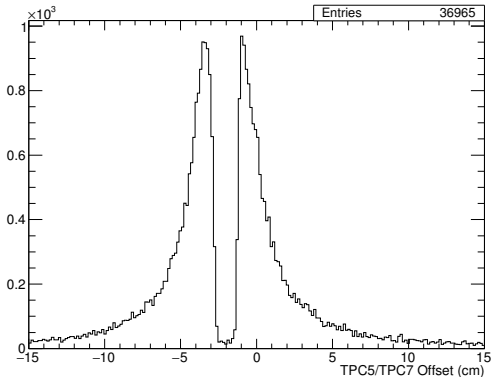
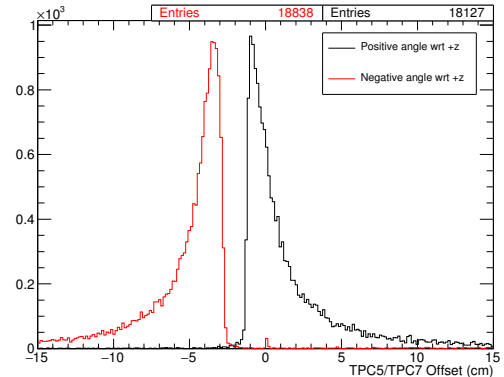
(a) $z\text{-offset} = 2 \text{ cm}$, $x\text{-offset} = 0 \text{ cm}$.(b) $z\text{-offset} = 2 \text{ cm}$, $x\text{-offset} = 0.5 \text{ cm}$.(c) $z\text{-offset} = 2 \text{ cm}$, $x\text{-offset} = 0.5 \text{ cm}$.

Fig. 7.12 Studies of the effects of offsets in the positions of the APAs in simulation. Artificial z - and x - offsets are introduced and their impact observed in the measurements of Δz . Figure 7.13a shows the effect of an offset in the z -direction; as expected, there is a single peak measuring the inputted value. Figures 7.13b and 7.13c show the consequence of offsets in both the x - and z -directions. This appears to show exactly what is seen in the 35 ton data (Figure 7.10).

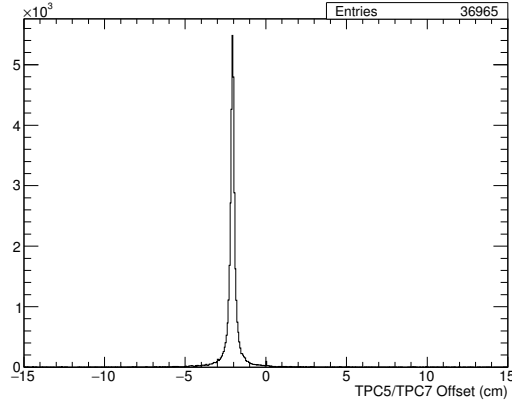
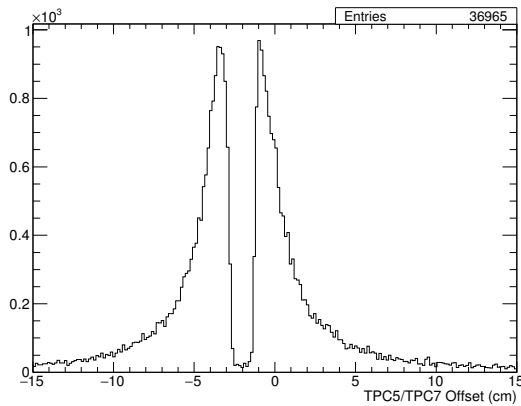
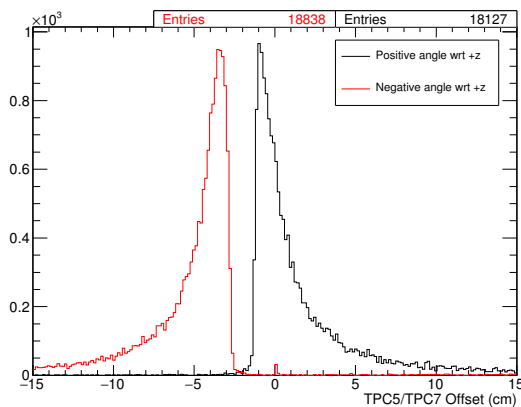
(a) $z\text{-offset} = 2 \text{ cm}$, $x\text{-offset} = 0 \text{ cm}$.(b) $z\text{-offset} = 2 \text{ cm}$, $x\text{-offset} = 0.5 \text{ cm}$.(c) $z\text{-offset} = 2 \text{ cm}$, $x\text{-offset} = 0.5 \text{ cm}$.

Fig. 7.13 Same as previous page – which is better? I prefer the layout of the previous page but I like this one because you can see the 2cm offset in line with each other down the page! Studies of the effects of offsets in the positions of the APAs in simulation. Artificial z - and x - offsets are introduced and their impact observed in the measurements of Δz . Figure 7.13a shows the effect of an offset in the z -direction; as expected, there is a single peak measuring the inputted value. Figures 7.13b and 7.13c show the consequence of offsets in both the x - and z -directions. This appears to show exactly what is seen in the 35 ton data (Figure 7.10).

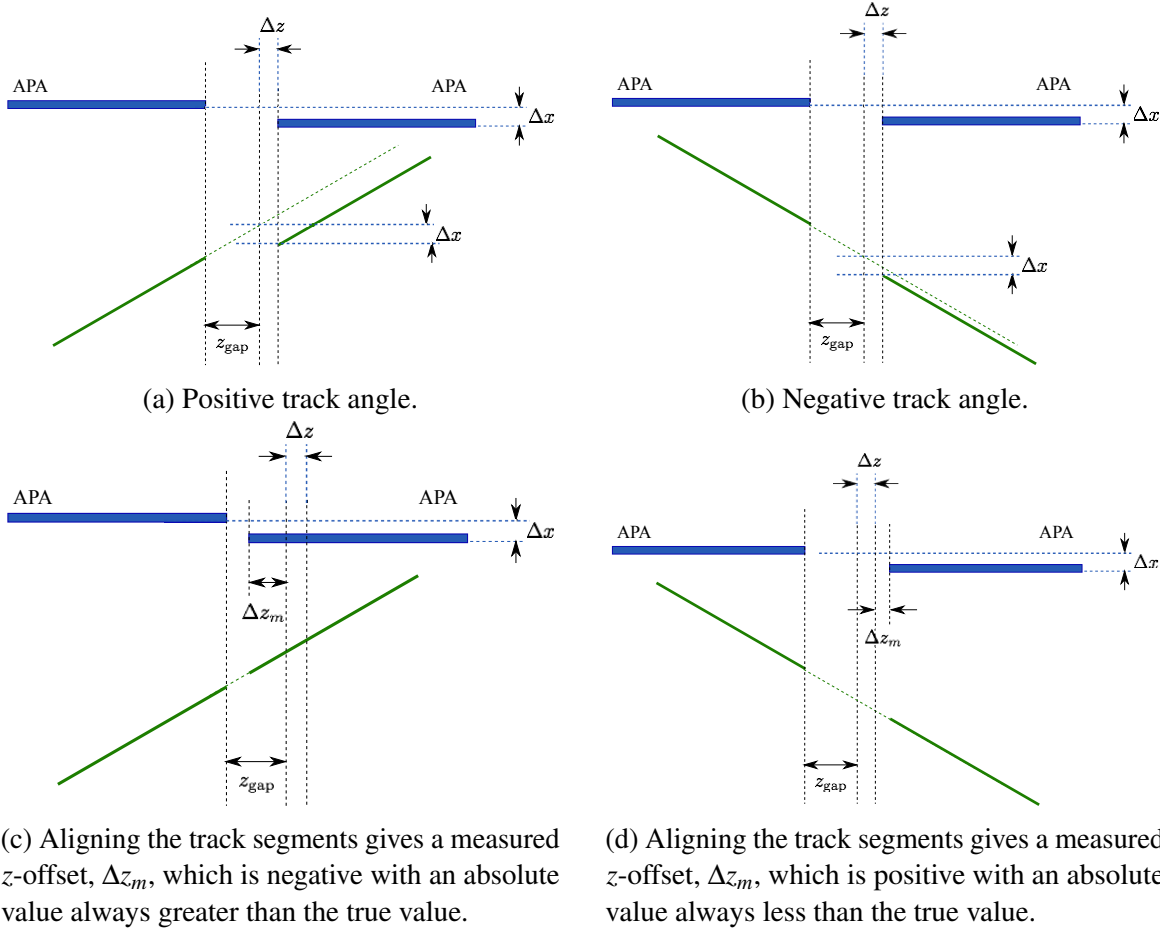


Fig. 7.14 Demonstration of the effects of offsets in both the x - and z -directions in the determination of Δz between TPC5 and TPC7. With an x -offset present, it is impossible for the true value of Δz to be measured – this is evident from Figure 7.13. It is clear from these geometrical considerations how the measured offset Δz_m will populate distributions either side of the true value; the true value Δz is given by the minimum between the two distributions.

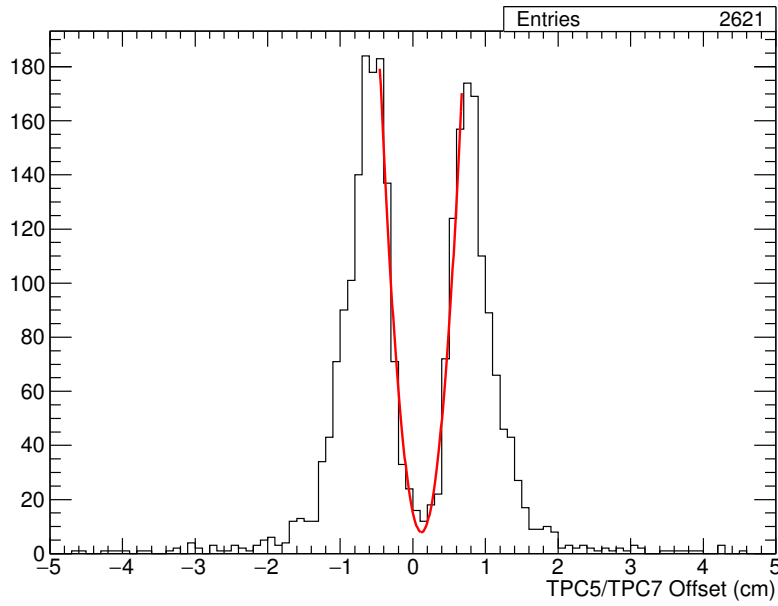


Fig. 7.15 Extraction of the true value of Δz from the full distribution of measured z -offsets. A measured value of 0.117 ± 0.007 cm is found.

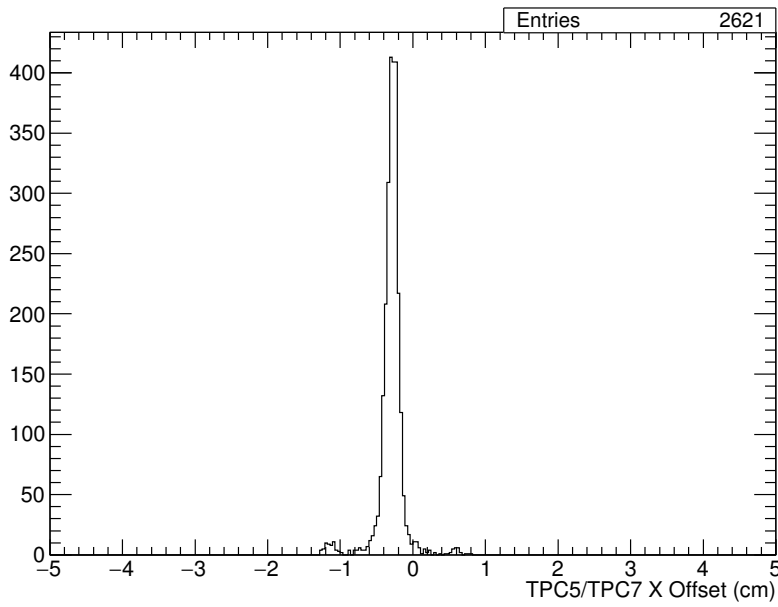


Fig. 7.16 Measurement of the x -offset between TPC5 and TPC7 after applying the z -gap corrected determined using the method described in the text and Figure 7.15. A measurement of -0.286 ± 0.002 cm is determined.

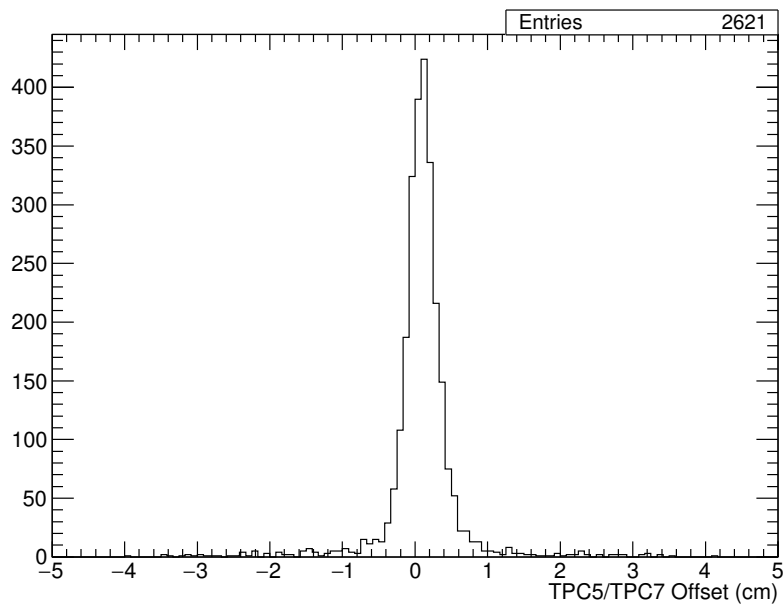


Fig. 7.17 Measurement of the z -offset between TPC5 and TPC7 after applying the x -offset determined from Figure 7.16. As initially anticipated, there is a single peak distributed around the true value of the offset. This validates the method used and confirms the initial presence of an x -offset between the neighbouring APAs. The final measurement of Δz is 0.103 ± 0.004 cm which agrees reasonably with the value measured previously (0.117 ± 0.007 cm from Figure 7.15).

7.3.1.2 Measurements of the APA Offsets

The offsets apparent from the data for all of the gaps accessible using TPC tracks in the long drift volume were determined as described in Section 7.3.1.1. Appendix ## contains all relevant figures (does an appendix seem a good idea here? I don't think we need the same figures as the previous section for each of the gaps here, but might be nice to have them somewhere?). Table 7.1 contains all the measurements and the new gaps, taking these offsets into account, are presented in Table 7.2.

NOTE: this discussion is exactly the same as what I put in the paper... is this a problem?
It seems silly rephrasing everything but I understand it may be necessary.

The determined errors are statistical only; the effects of systematic uncertainties were not considered and assumed to be negligible in comparison. Given the method used to determine these offsets, which involved multiple fits in differing parameter spaces, one may expect correlations between the uncertainties in the offsets measured in x and z . The implications of this correlation was considered by varying the value of each parameter across the range of its 1σ error and evaluating the effect of this on subsequent measurements. It was found this is negligible in the context of the determined uncertainties and would not justify thorough evaluation.

There appears to be some consistency in the measurements of the x -offsets by considering differences in this value between TPC1 and TPC7. Despite the fact they do not neighbour each other, this is possible by considering the successive offsets measured between TPC1/TPC3 and TPC3/TPC7, and TPC1/TPC5 and TPC5/TPC7. An exceptional agreement is seen between the two values. There also seems to be slight evidence of a rotation between TPC1 and TPC7 when considering the associated z -offsets; the offset at the top of the APA (when measured via TPC5) is greater than at the bottom (when measured via TPC3). However, this can certainly be explained in the context of the limitations of the method and statistical fluctuations and would require more data and a more robust approach to justify these claims. Such analysis is not possible with the 35 ton data.

The method demonstrated here will have direct implications for similar studies using the full DUNE far detector. All the gaps between the APAs, both in the drift and z directions, will need to be understood for accurate reconstruction and are essential in order to make the precise physics measurements DUNE wishes to. For example, accurate calorimetric reconstruction is imperative in order to perform particle identification and shower energy determination and is directly related to the drift time of the ionisation electrons; any offsets in APA positions will lead to systematic uncertainties in this information.

Table 7.1 Measurements of all the APA offsets determined from the 35 ton TPC data. The method followed is described in Section 7.3.1.1. The first row represents the initial measurements of the z -offset from the two-peak distribution, with the following two lines detailing the measured offsets that follow from these results.

	TPC1/TPC3	TPC1/TPC5	TPC3/TPC7	TPC5/TPC7
Initial z -offset (cm)	-0.64 ± 0.04	0.15 ± 0.01	0.58 ± 0.06	0.117 ± 0.007
x -offset (cm)	-0.377 ± 0.006	-0.252 ± 0.002	-0.16 ± 0.01	-0.286 ± 0.002
z -offset (cm)	-0.63 ± 0.02	0.131 ± 0.007	0.55 ± 0.03	0.103 ± 0.004

Table 7.2 The corrected gaps between the APAs, in x and z , based on the offsets measured (Table 7.1).

	Assumed (cm)	Offset (cm)	Corrected (cm)
TPC1/TPC3 x -gap	0	-0.377 ± 0.006	-0.377 ± 0.006
TPC1/TPC5 x -gap	0	-0.252 ± 0.002	-0.252 ± 0.002
TPC3/TPC7 x -gap	0	-0.16 ± 0.01	-0.16 ± 0.01
TPC5/TPC7 x -gap	0	-0.286 ± 0.002	-0.286 ± 0.002
TPC1/(3)/TPC7 x -gap	0	-0.538 ± 0.003	-0.538 ± 0.003
TPC1/(5)/TPC7 x -gap	0	-0.537 ± 0.010	-0.537 ± 0.010
TPC1/TPC3 z -gap	2.53	-0.63 ± 0.02	1.90 ± 0.02
TPC1/TPC5 z -gap	2.08	0.131 ± 0.007	2.211 ± 0.007
TPC3/TPC7 z -gap	1.63	0.55 ± 0.03	2.18 ± 0.03
TPC5/TPC7 z -gap	2.08	0.103 ± 0.004	2.183 ± 0.004
TPC1/(3)/TPC7 z -gap	4.16	-0.08 ± 0.04	4.08 ± 0.04
TPC1/(5)/TPC7 z -gap	4.16	0.23 ± 0.01	4.39 ± 0.01

7.3.2 Charge Deposited by APA Gap-Crossing Muons

The charge deposited by gap-crossing particles cannot be collected in the dead regions between the APA frames. It is interesting to consider where the charge is read out in order to further understand the implications of a modular TPC design.

Figures 7.18 and 7.19 demonstrate the properties of hits as a function of distance from the nearest TPC edge. It appears more hits are found as charge is collected near a gap but the charge of these hits do not differ significantly. This may be interpreted as hits arriving at a slightly later time near the APA gaps after drifting towards the nearest wire to the gap from a more gap-centred position. One may expect to observe this in the data as a smearing in the tick direction where charge is deposited over more time, leading to a small gradient change. Although not as noticeable as anticipated, this effect is observable in the event display shown in Figure 7.20.

7.4 APA-Crossing Muons

The 35 ton is the only proposed experiment before the full DUNE far detector modules that have fully implemented anode planes within the cryostat reading out data from multiple drift regions simultaneously (ProtoDUNE will have wrapped wire APAs but will only read out one drift region each and SBND has the CPAs in the centre of the cryostat with the APAs at the edges). Referring to Figure 3.10, this is a design consideration that features prominently in the eventual detector so any implications in the data must be well understood. Analysis of tracks which pass through the APAs and deposit charge in both drift regions is the subject of this section.

In Section 7.4.1, a method to determine the absolute event time, T_0 , from APA-crossing tracks is presented and in Section 7.4.2 the charge deposited by these tracks, particularly when crossing through the planes, is studied. Comparisons between the two drift regions, made possible by comparing tracks left by the same particle, are contained in Section 7.4.3.

7.4.1 T_0 Determination from APA Crossing Tracks

Given the nature of a TPC detector, an ‘event time’ (T_0) must be known in order to set an absolute timescale, and therefore absolute position, on all interactions within the detector. An accurate T_0 is essential for calorimetric reconstruction: in order to understand how much charge a hit had when it was created, a lifetime correction dependent on the total drift time must be applied. An incorrect T_0 would lead to a systematic under- or over-estimation of

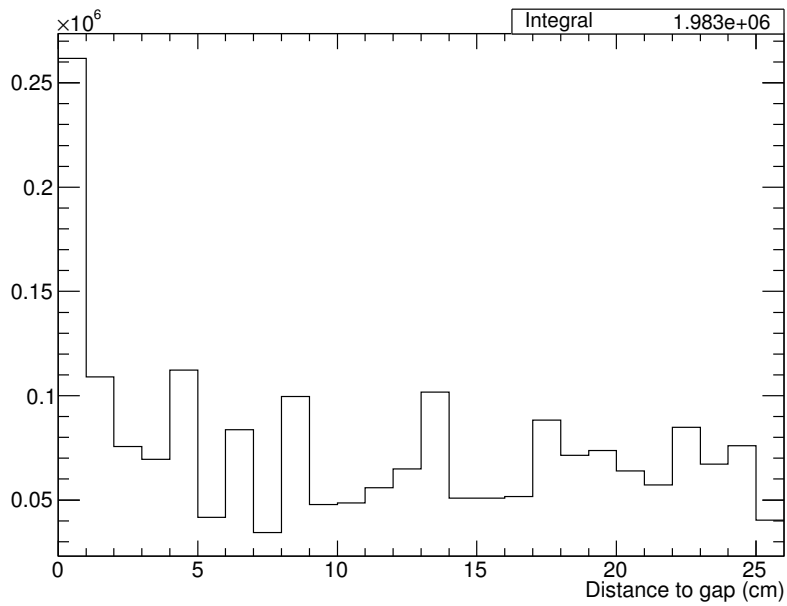


Fig. 7.18 Number of reconstructed hits at different distances from nearest APA gap.

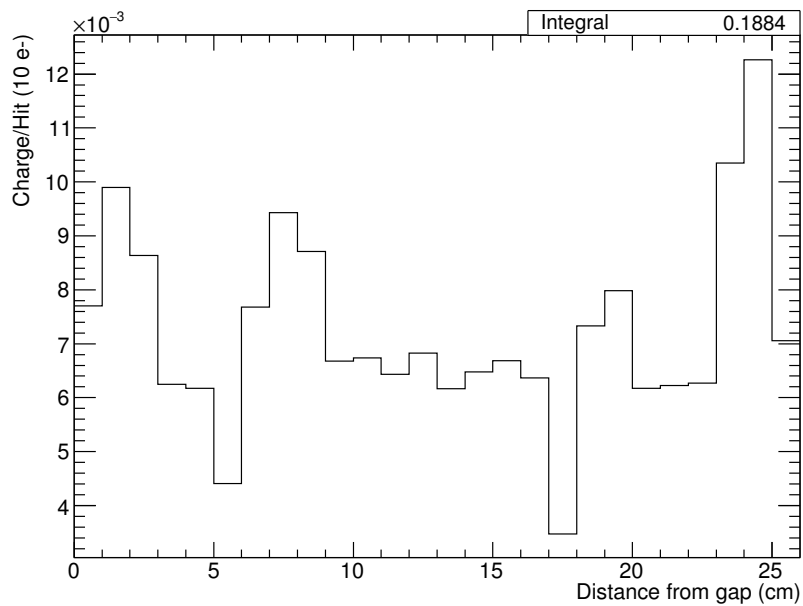


Fig. 7.19 The average charge of hits as a function of distance to nearest APA gap.

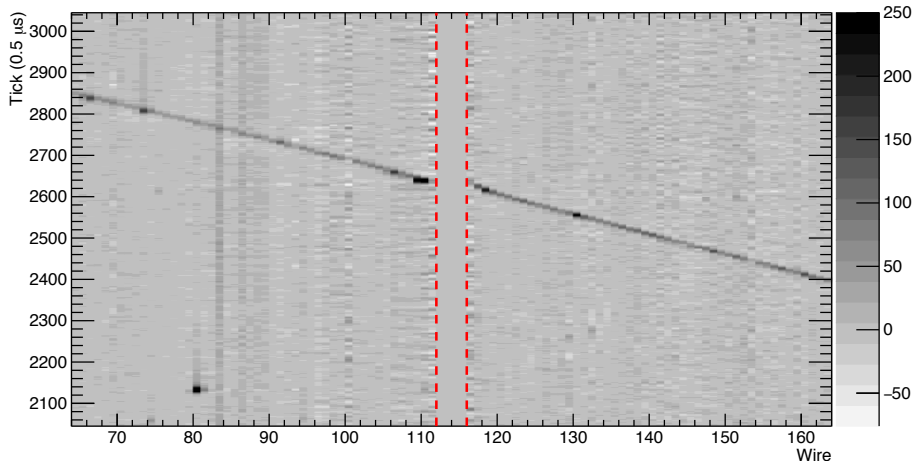


Fig. 7.20 Event display of an APA gap-crossing track, focussed on the gap region. Charge arriving at the centre of a gap deflects toward the nearest wire and is collected at a slightly later time. This results in more charge being deposited on wires nearest the gap, with a larger spread in time. This is subtly observable in the charge distributions shown here.

the reconstructed energy and have implications in particle identification and shower energy determination.

In a LArTPC, an event time is usually given by an external triggering system. The DUNE far detector will rely on the instantaneous detection of photons produced from the immediate recombination of the ionisation electrons with positive Ar ions. In the 35 ton, an additional external system was provided by the scintillation counters. Since the sample of APA-crossing muons used in this analysis were all selected and reconstructed using counter information, an interaction time is immediately known.

Without correctly accounting for T0, the tracks on each side of the APAs appear offset from the planes. This is evident from the event display shown in Figure 7.6. By aligning the track segments on either side of the APAs, a measurement of T0 can be made directly from the TPC data.

7.4.1.1 Aligning APA Crossing Tracks

Two complementary methods were used to accurately align the track segments across the APA. Both involved initially correcting for the counter T0, T_0^{counter} , before considering a range of alternative T0 hypotheses and minimising a relevant metric to determine the most likely value. In the first method, demonstrated in Figure 7.21, a least square linear fit is applied to the track and the residual minimised (the ‘residual method’). The second method, demonstrated in Figure 7.22, involves fitting a line to each segment in turn and minimising the projected distance between the intersections of the lines with the centre of the APAs

($x = 0$) (the ‘separation point method’). As will be shown, and can be seen from Figs. 7.21b and 7.22b, the two methods agree very well with each other.

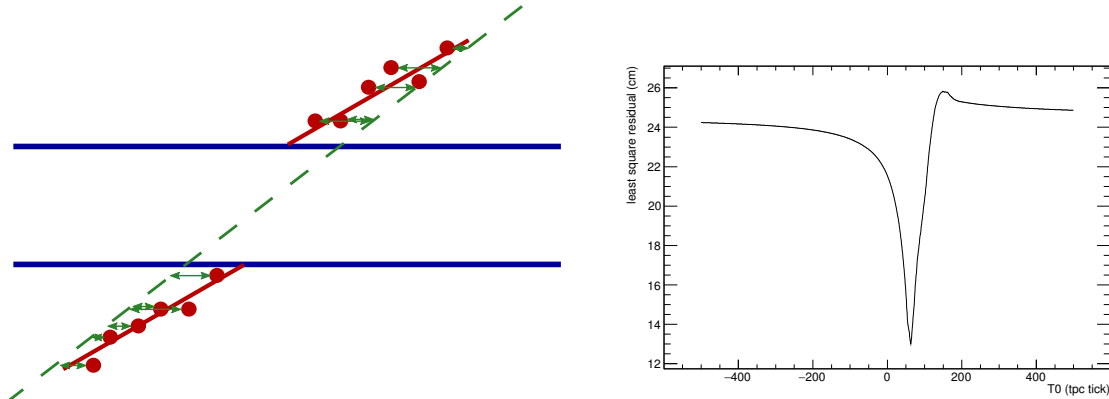
Naively, one would expect the T0 determined using these methods, T_0^{TPC} , to agree with T_0^{counter} . This is confirmed by applying the analysis to simulated data and demonstrated in Figure 7.23a. However, there appears to be a systematic offset between the T0 given by the counters and measured from the TPC data. The distribution of this discrepancy is shown in Figures 7.23b and 7.23c for each of the two methods described; it peaks around 61 ticks ($30.5 \mu\text{s}$) and is importantly incompatible with zero. This suggests an inconsistency somewhere in the data taking and attempts to understand this track misalignment will be the subject of the remainder of this section. Figure 7.24 shows an example track before and after this disparity is corrected for. As is evident from Figure 7.23, the separation point method provides more consistent results so this will be used exclusively for alignment measurements in the rest of this section.

7.4.1.2 Understanding the Misalignment of APA-Crossing Tracks

The underlying issue described above is essentially a misalignment of the same particle track between the two drift regions, demonstrated plainly in Figure 7.25. This obviously is not physical and stems from an issue with the detector or data readout. The most obvious cause is a miscalibration of the DAQ timing systems for the separate detector components, as previously assumed. There are however other possible solutions to the problem and it is likely the effect arises from a combination of different factors.

Geometry Apart from timing, a misunderstanding of the geometry could explain this perceived misalignment. The spacing between the collection planes is one such example, as demonstrated in Figure 7.26a; the spacing necessary to explain this effect, determined by aligning the tracks using the methods discussed above over a range of collection plane spacing hypotheses, is demonstrated in Figure 7.26b. As is evident from the figure, the collection planes must be repositioned in such a way that they would be reversed; the track alignment complications cannot be explained solely by this.

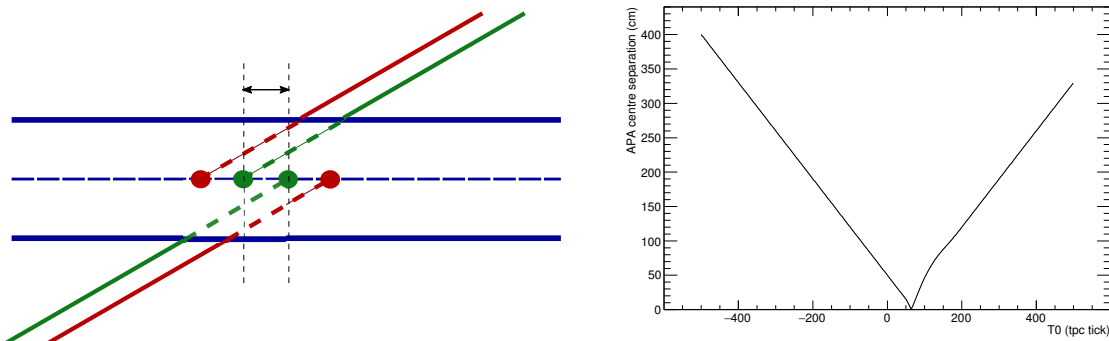
A further problem is related to the wire positioning on the APAs in the z -direction; it is understood there may be a discrepancy between the two sides of the APA resulting in hits from the long and short drift regions at the same z -position reconstructed with a systematic offset. Figure 7.27a shows how this could be utilised to explain the apparent track misalignment with Figure 7.27b showing the distribution of corrected z positions necessary to resolve the issue. Offsets of $\sim 2 \text{ cm}$, as suggested by these results, are highly unlikely



(a) Demonstration of the calculation of residuals from a linear fit through all hits. The red points are hits and the green line represents a linear fit through all points on both sides of the APA.

(b) The residuals to the linear fit of the track over a range of T_0 candidates. The value of T_0 which minimises this distribution (62 ticks in this case) is considered the most likely interaction time.

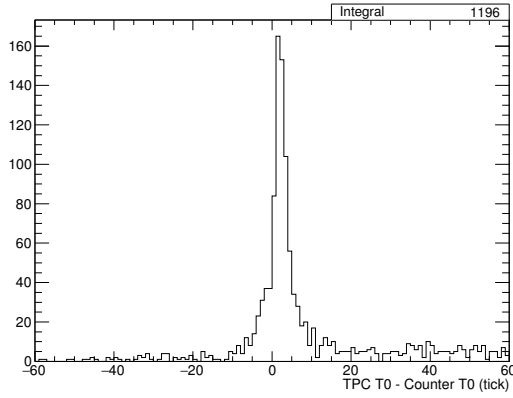
Fig. 7.21 Method to align track segments on either side of the APAs involving minimising residuals from a linear least square fit. A fit is applied to all hits and the resulting residual, a representation of the ‘goodness of fit’, is minimised over a range of T_0 candidates to find the most likely interaction time for the particle leaving the track.



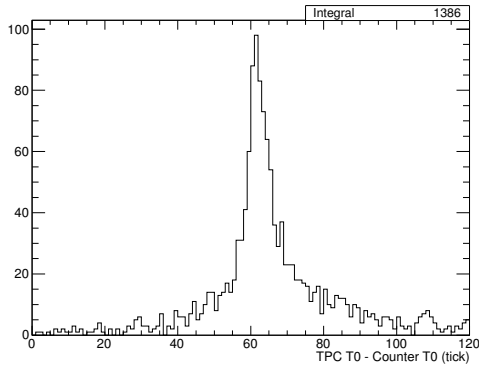
(a) Demonstration of the determination of the distance between the track segments at the centre of the APAs. The red and green lines represent linear fits to the hits (applied separately on each side of the APA) for different values of T_0 .

(b) The separation distance over a range of T_0 candidates. The value of T_0 which minimises this distribution (63 ticks in this case) is considered the most likely interaction time.

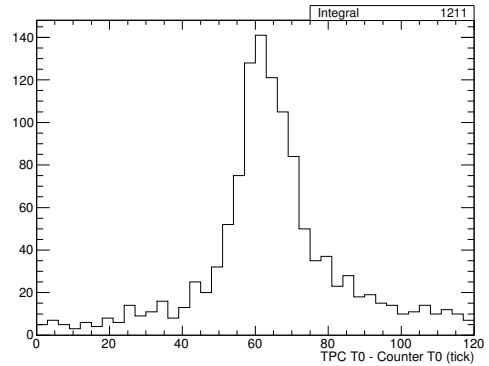
Fig. 7.22 Method to align track segments on either side of the APAs involving minimising the distance between the projected intersection of each with the centre of the APAs. A fit is applied to each track segment separately and the distance between the intersection of these lines with the centre of the APA is minimised over a range of T_0 candidates to find the most likely interaction time for the particle leaving the track.



(a) 35 ton simulation. The difference in the two measurements of T_0 is distributed around zero, as expected, and validates the method. The peak is actually at 1 tick, indicating a slight systematic offset.



(b) 35 ton data using the separation point method.



(c) 35 ton data using the residual method.

Fig. 7.23 Difference between the T_0 calculated from TPC data and the T_0 provided by the counters representing the trigger time of the through-going muon, for simulation (Figure 7.23a) and data (Figures 7.23b and 7.23c). If the two measurements of T_0 agree the distribution would peak around zero, confirmed in simulation; the fact this is not the case for data is indicative of a systematic offset somewhere in the data taking.

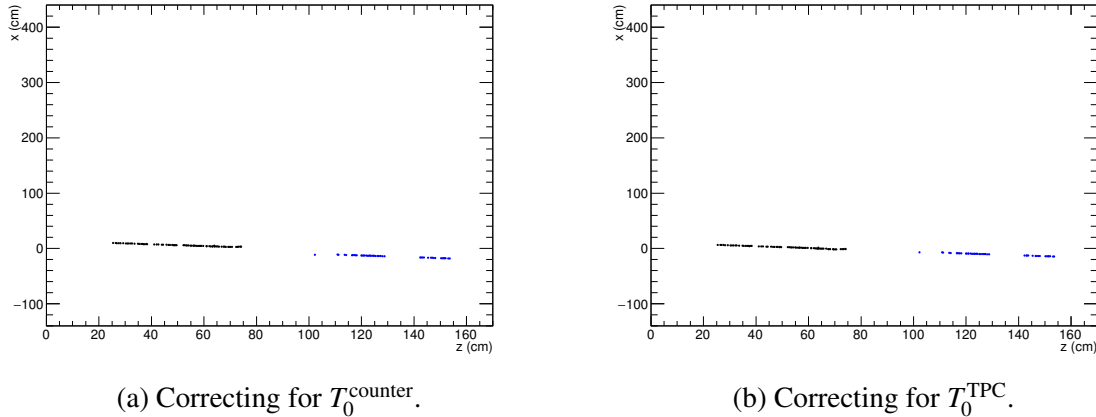


Fig. 7.24 Correcting for T_0 using T_0^{counter} (Figure 7.24a) and T_0^{TPC} (Figure 7.24b). The difference is subtle but noticeable; the method for determining T_0 directly from the TPC data can be validated by eye. The minimisation of the metrics to determine T_0^{TPC} in this case are demonstrated in Figs. 7.21b and 7.22b.

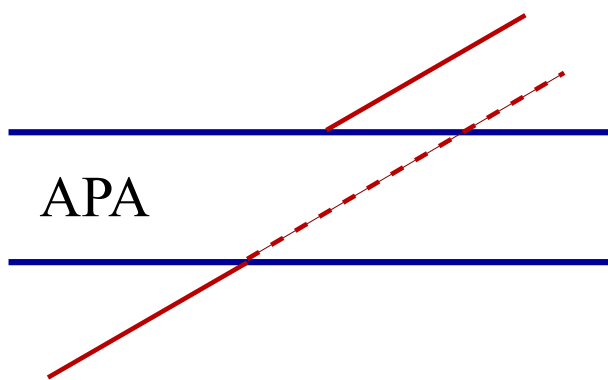


Fig. 7.25 Possibly unnecessary, but helps to explain all the various factors which could explain the offset. Can remake if necessary. Demonstration of the effect observed in the 35 ton data concerning tracks crossing the APAs. Even after correcting for the T_0 provided by the counters, there is still a misalignment of the track segments across the APA frames.

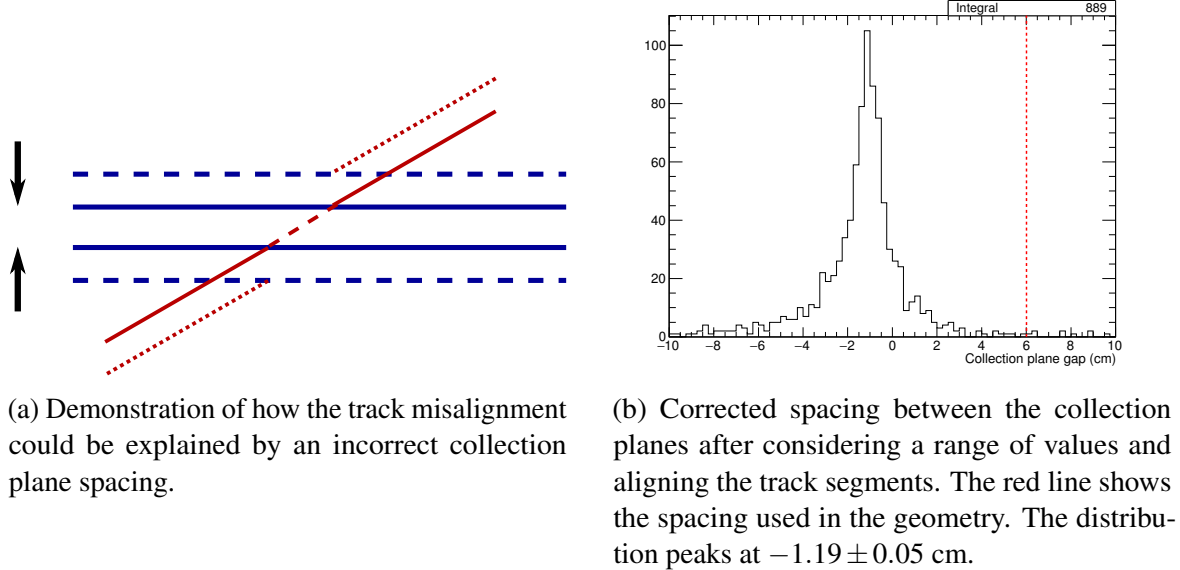


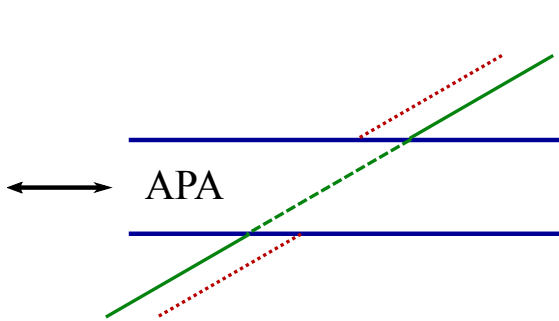
Fig. 7.26 Attempting to correct the track segment misalignment by assuming a misunderstanding of the spacing between the collection planes. It appears the resulting spacing necessary to correct for this issue would involve physically reversing the order of the planes.

given the scale of offsets identified in Section 7.3.1.2, indicating again the track alignment problem cannot be resolved in this way.

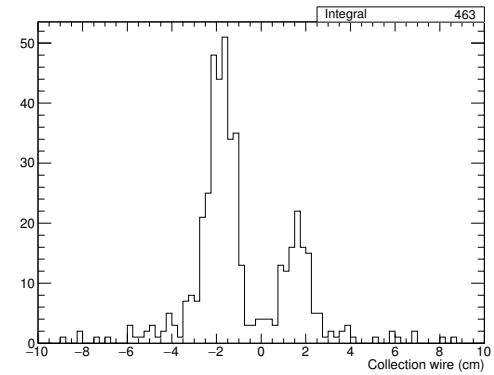
Drift velocity The drift velocity affects the angle of the tracks in wire/time space; a high velocity would result in a refraction-like effect towards the APA planes. As demonstrated in Figure 7.28a, this could explain the track segment misalignment if the effect was large enough. Figure 7.28b shows the necessary drift velocity required to account for the disparity observed in data; compared to a nominal value of 109 cm/ms, the scale of the change required to explain the oddity is unreasonably large, around a factor of five.

This can be tested by measuring the drift velocity directly from the data. Taking tracks which pass through opposite counter pairs and comparing this drift distance with drift time is a trivial exercise, demonstrated in Figure 7.29. The measured value of 110.2 ± 0.4 cm/ms agrees very well with the aforesaid value, determined theoretically, of 109 cm/ms. It may therefore be assumed the drift velocity is as expected and does not contribute at all to the track alignment anomaly.

Timing The timing offset calculated in Section 7.4.1.1, $32 \mu\text{s}$, is so large it was assumed another explanation for the track segment misalignment was likely. However, after reviewing all possibilities it appears there must be a significant timing offset present somewhere in the

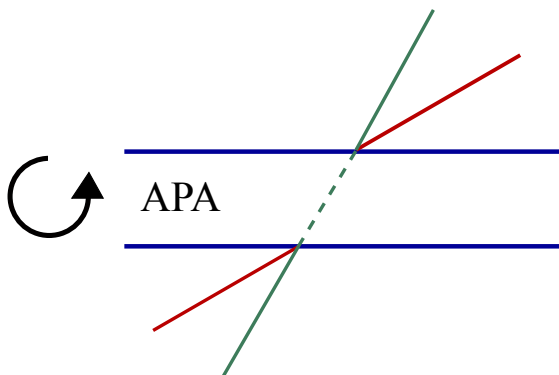


(a) Demonstration of how the track misalignment could be explained by an offset in the wire z -position on either side of the APA.

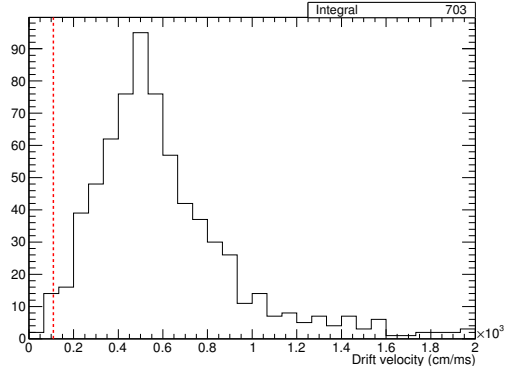


(b) Corrected z -positions of the APA wires after considering a range of values and aligning the track segments.

Fig. 7.27 Attempting to correct the track segment misalignment by assuming a misunderstanding of the positioning of the collection wires inside the detector. The wire offset would have to be around 2 cm to fix this issue.

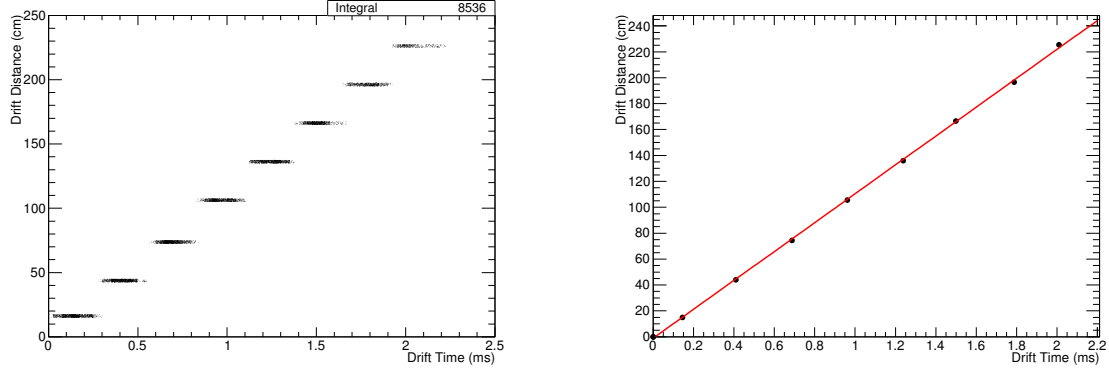


(a) Demonstration of how the track misalignment could be explained by an incorrect drift velocity.



(b) Corrected drift velocity required to align the track across the APAs. The red line shows the assumed value of 109 cm/ms.

Fig. 7.28 Attempting to correct the track segment misalignment by assuming an incorrect drift velocity. In order to account for the effect noted in the data the drift velocity would have to around five times larger than that initially calculated from models.



(a) Distribution of hit drift times for eight sets of counter pairs, assuming all tracks pass through the centres of the counters.

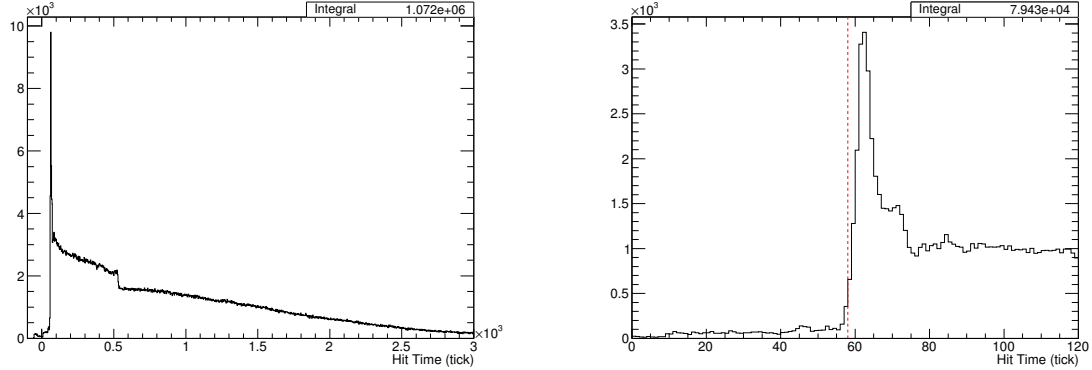
(b) The eight points found from taking the Gaussian mean of the time distributions for each rough drift distance.

Fig. 7.29 Measuring the drift velocity of the ionisation electrons by taking tracks passing through opposite counter pairs and comparing the corresponding drift distance to the drift time. Assuming all tracks pass through the geometric centres of the counters, a poor assumption, a distribution of hit time for this drift distance can be found; this is shown in 7.29a. Taking each counter pair separately and fitting a Gaussian to the distribution of drift times nullifies the assumptions necessary due to a lack of exact knowledge, on a track by track basis, of the exact x -position. This is shown in the graph in Figure 7.29b.

data. Further evidence for this hypothesis is presented in Figure 7.30 which displays the T0-corrected time distribution for all hits on the APA-crossing track. The minimum drift time these hits may have, since they pass directly through the planes, is the interaction time, T0. As is evident from the distribution in Figure 7.30b, this is around 58 ticks ($29 \mu\text{s}$) and is notably inconsistent with zero. The curious spike at the interaction time motivates the work presented in Section 7.4.2 and will be discussed there. Additionally, it is possible to compare the T0 provided by the counters with information from the photon detectors. This is shown in Figure 7.31 and provides further confirmation for a timing miscalibration in the TPC readout.

This interesting result provoked further investigation into the notion of a timing offset between detector components, specifically the TPC and counter readout (RCEs and PTB respectively). Confirmation of this miscalibration is displayed in Figure 7.32 which shows the difference between the timestamps recorded by each of the subcomponents upon receiving the trigger.

There are now three measurements of the timing offset with a slight disagreement between each. This will be discussed further in Section 7.4.1.3.



(a) Over the full range of drift times. The sharp dip around 500 ticks corresponds to the maximum drift time for hits in the short drift region; beyond this only hits in the long drift region contributes to the distribution.

(b) Zoomed in on the interaction time. The red line is drawn at 58 ticks ($29 \mu\text{s}$) and represents, by eye, the start of the distribution.

Fig. 7.30 The T0-corrected drift time for hits on APA-crossing tracks. The lower leading edge of this distribution is an indication of the interaction time, T0.

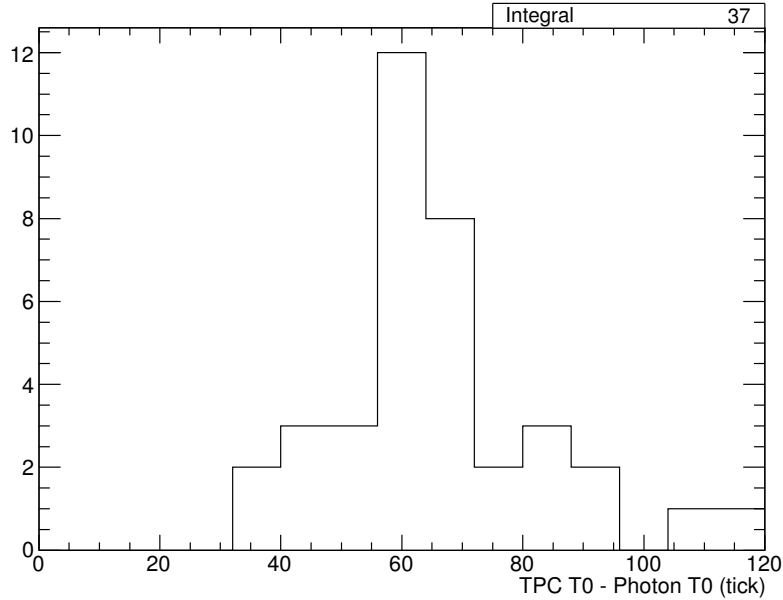


Fig. 7.31 Difference between the interaction time measured by the TPC data and that provided by photon detector information. Only events with a single reconstructed flash are considered, with each assumed to have been caused by the triggering particle. This results in very few events, but clear supporting evidence of a timing offset on the order of 60 ticks is found.

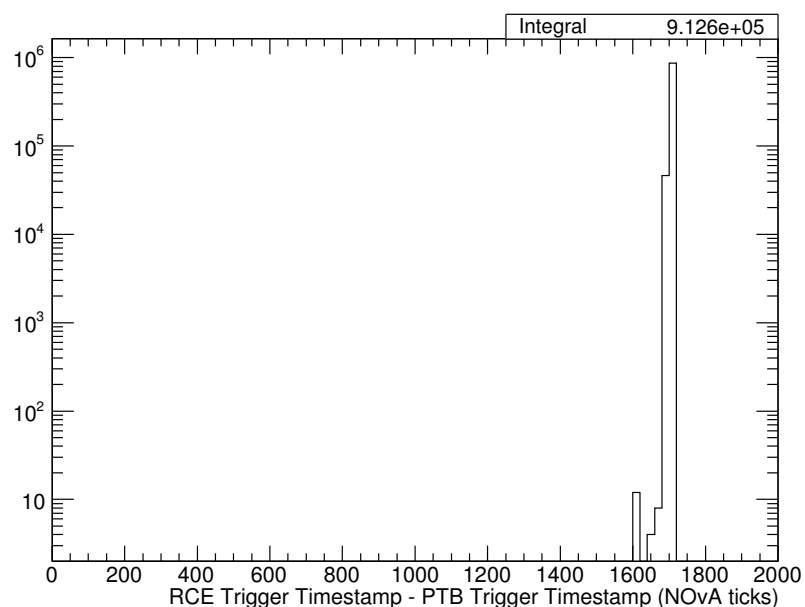


Fig. 7.32 The difference between the timestamps recorded by the PTB and the RCEs upon receiving a trigger. The absolute timing for the DAQ system is given, along with most experiments at FNAL, by ‘NOvA time’: a 64 MHz clock starting on 1st January, 2010 (with one NOvA tick therefore being 15.625 ns). The distribution peaks sharply at 1705 NOvA ticks, or 26.6 μ s.

7.4.1.3 Combined Offset Analysis

The discussion in Section 7.4.1.2 hints strongly at an intrinsic timing offset present in the data. However, as already shown in Section 7.3, it is understood there are geometrical offsets in the positions of the APAs in the x - and z -dimensions. Attempting to measure all these offsets simultaneously presents challenges since they all affect each other. It is possible the tension between the measurements of the timing offset may be resolved by combining the results from each of the offset calculations.

The timing offset will not influence the determination of the geometrical APA gaps (found in Section 7.3) unless the track segments used to measure the gaps cross through the APA frames; the timing is consistent for each drift region. A simple cut was used to exclude such events when making these measurements. However, the geometrical offsets will have an impact on the APA crossover analysis. For example, the drift times measured for each hit will be affected by the physical positions of the APAs. Figure 7.33 shows the distribution of the drift times for all track hits corrected for the offsets implied by the x -gap measurements. It can be seen this accounts for the disparity between the previous measurements. It does not appear to agree completely with the offsets found between the timestamps but serves to demonstrate differences from the assumed positions of the APAs have a very sizeable effect on distributions such as these.

Correcting for this timing offset, along with those in the x - and z -positions of the APAs, does not entirely account for the initial inconsistency observed in Figure 7.23. A similar evaluation to that undertaken in Section 7.4.1.2, namely considering the required disparities in various quantities to account for this, may be used to facilitate a complete understanding. After correcting for the three aforementioned offsets, Figure 7.34 demonstrates the necessary misunderstandings in the collection plane spacing and the z -positions of the collection wires to account for the remaining discrepancy. It seems highly likely that the offsets between the APA gaps left unresolved in the short drift region, incalculable in the 35 ton data, can account for the outstanding misalignment between the track segments. Nothing conclusive can be extracted from Figure 7.34b with regards to the values of these uncertainties since this considers differences between all short drift region TPCs and long drift region TPCs together but implies further offsets at a similar scale to those measured in the long drift region may still be present. With corrected APA gaps in the short drift region, it is reasonable to argue the track segment misalignment between drift regions would be completely resolved.

This is the first time tracks crossing the readout planes have been used in a LArTPC experiment and have proven to be a valuable way of calibrating inter-detector components and finding other inconsistencies in the data. Without studying this data set, the timing offset between the TPC and the external counters would not have been discovered and all

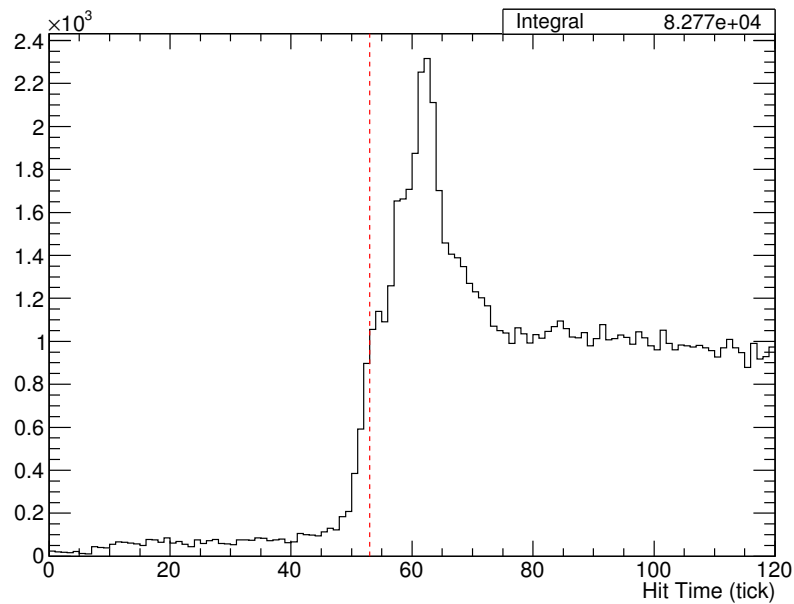
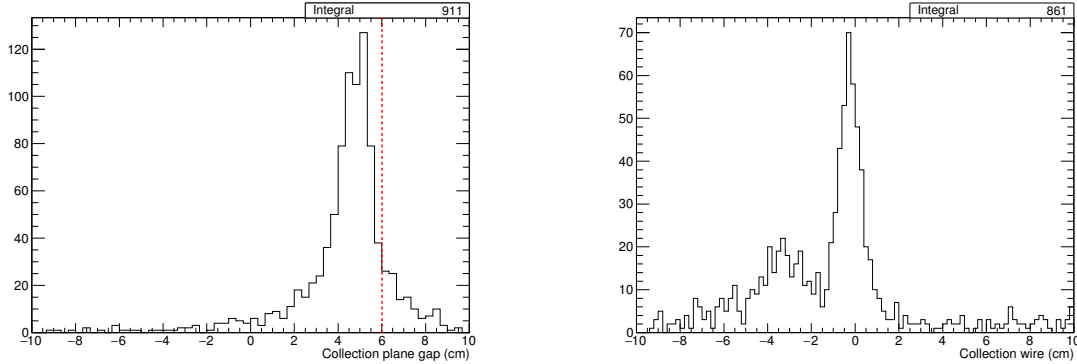


Fig. 7.33 The distribution of the drift times of all hits on APA-crossing tracks after correcting for the APA offsets along the direction parallel to the drift direction, found in Section 7.3. The red line represents a T0 of 53 ticks, representing the difference observed between the trigger timestamps between the scintillation counter and TPC readout systems. The hit time distribution appears to agree with this value to a greater extent than previously (Figure 7.30b).



(a) Assuming a misunderstanding in the spacing between the collection planes, a value of 4.74 ± 0.04 cm is measured. This is a difference of 1.27 ± 0.04 cm from the assumed spacing, a discrepancy which is highly unlikely.

(b) Assuming a misunderstanding in the alignment of the collection planes in z between the two drift regions, an offset of -0.24 ± 0.03 cm is found. Given the scale of the corrections determined in Section 7.3.1.2, and the incapability to measure the gaps in the short drift regions, this is emminently credible.

Fig. 7.34 Accounting for the extra discrepancy in track alignment after fixing for all the measured offsets by assuming a misunderstanding in the collection plane spacing (Figure 7.34a) and the z -positions of the collection wires (Figure 7.34b).

analyses would naively use the incorrect T_0 . The experience in characterising the offsets in the 35 ton, in time, x and z , will be crucial when understanding the eventual DUNE far detector. Based on experience here, it is imperative these misunderstandings are mitigated as much as possible at the far detectors, with each module containing 150 APAs and four drift regions.

7.4.2 Charge Deposited by APA Crossing Tracks

The intriguing distribution of the T_0 -corrected hit times observed in the data, shown in Figure 7.30a, hints at some aspect of the detector response that needs to be understood. In the DUNE far detector, a large number of events will contain particles which pass through the APA frames so characterising resulting effects is critical. The equivalent plot for simulated data is shown in Figure 7.35. Comparing these distributions, there is a very obvious difference around the interaction time. It appears there is an effect present in the data, not currently being simulated, which manifests in around twice the amount of hits occurring at T_0 on the collection planes for APA-crossing tracks. This is described in Section 7.4.2.1 and the phenomenon is visible on event displays presented in Section 7.4.2.2.

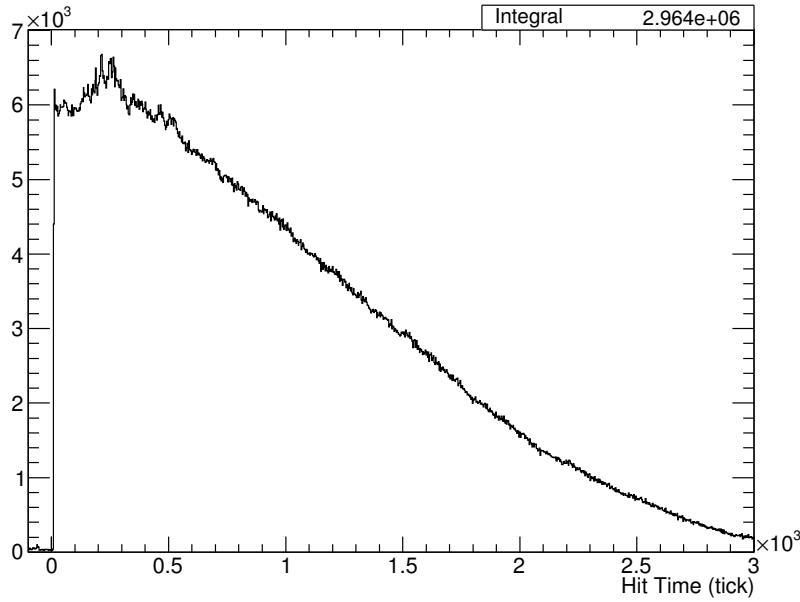


Fig. 7.35 The T0-corrected drift time for all hits on an APA-crossing track in simulation. The equivalent plot for 35 ton data is shown in Figure 7.30a.

7.4.2.1 Interaction Time Hits

The excess of hits at the interaction time is due to the use of a grounded ‘mesh’ at the centre of the APAs. The purpose of such a design choice is to ensure a uniform electric field across the face of the APA; without it the field would be ill-defined given the presence of the grounded, rectangular APA frames with positively biased planes on either side. It is plausible therefore to consider a ‘backward-facing’ field being set up between the grounded mesh and the positively biased collection planes which would lead to hits drifting the ‘wrong’ way when produced in this region; APA-crossing tracks would hence leave twice as many hits on the collection plane as the other planes. This is demonstrated schematically in Figure 7.36.

A convenient way of confirming whether or not the mesh can explain this excess of hits at the interaction time is possible since one of the four APAs in the 35 ton was constructed without the mesh, precisely for this purpose. Unfortunately, this was the APA which was more plagued by noise issues so very little good data is available from channels on this APAs. It is however possible to make a crude comparison; this is shown in Figure 7.37. The appears to confirm the shark peak of hits occurring at the interaction time comes from the APAs which use a mesh.

Using the 35 ton dataset, it is also possible to confirm that the mesh is functioning as expected. Without a mesh, one may expect a difference between the hits deposited on wires

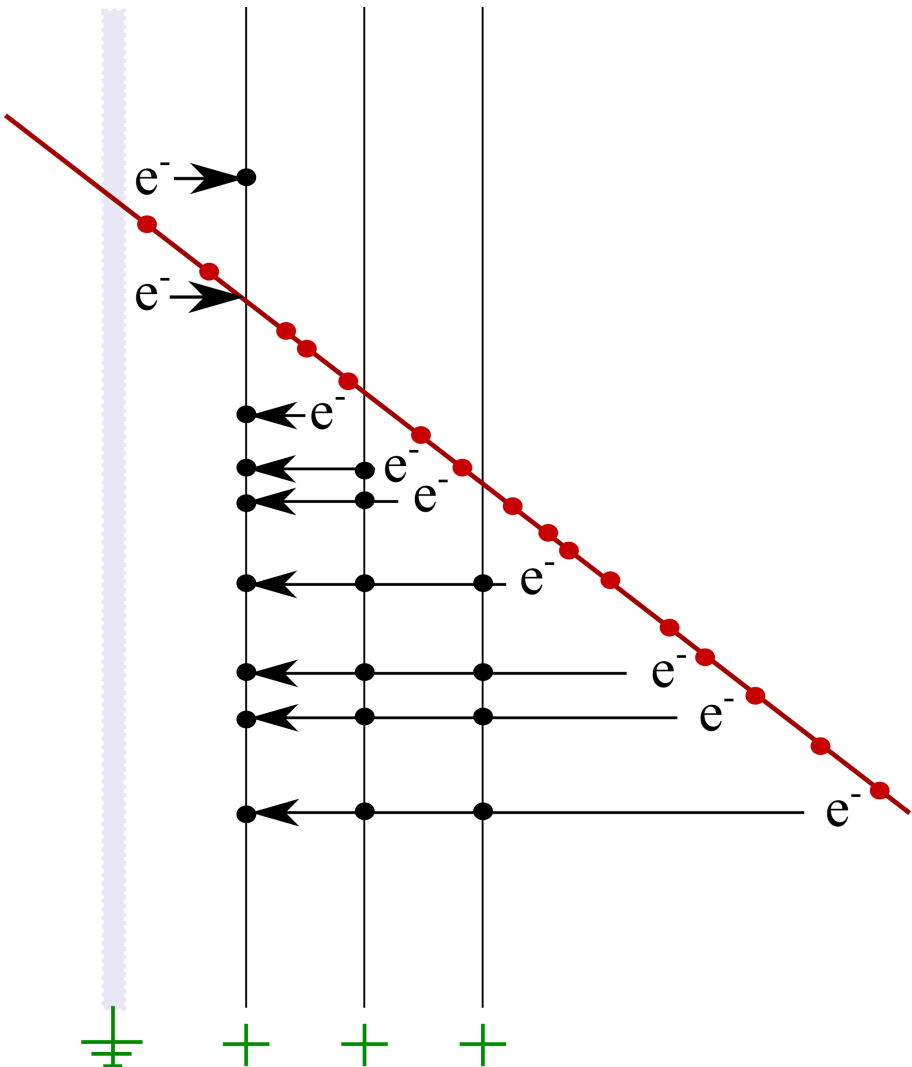
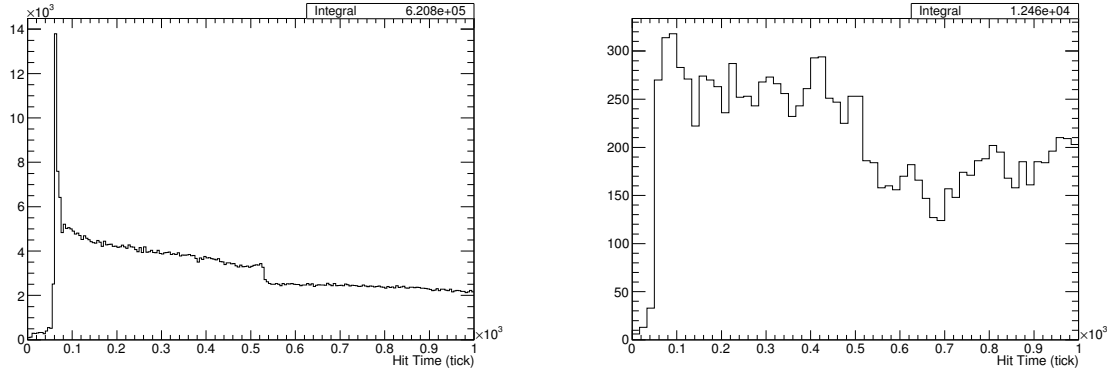


Fig. 7.36 Demonstration of the ionisation and hit collection for APA-crossing tracks. The red line represents a track passing through the anode planes, shown in black. The grey region is the centre of the APA frame on which the grounded mesh is afixed. The red dots correspond to the ionisation of electrons which then drift, depositing charge (black dots) on the readout wires. The three planes shown are, from left to right, the collection plane and the two induction planes. The biasing of each of the planes and mesh sets up field lines which all terminate on the collection wires, resulting in charge collected from before the track passes through and after.



(a) Hit times for all hits on APAs 0, 2 and 3; these are the three APAs containing the grounded mesh at the centre.

(b) Hit times for all hits on APA 1, the APA without a grounded mesh at its centre.

Fig. 7.37 Comparison between the T0-corrected hit time distributions on APAs with and without the grounded mesh. Even given the very low stats in Figure 7.37b, there is a noticeable difference in the distribution of hits around the interaction time.

towards the centre of an APA face and wires at the edges, in front of the grounded frame. The functionality of the grounded mesh ensures there is no difference between any wires on a given APA. Figure 7.38 confirms this is the case.

A natural question to pose at this point is to ask if these ‘extra’ hits deposited by APA-crossing tracks as a result of this ‘backwards’ field have similar properties to the ‘correct’ hits. The most important property to consider is the charge of the hits; Figure 7.39 shows the average charge per hit for hits occurring at the interaction time and all other hits. It is clear from this there is nothing different about these additional hits and they can be treated in the same way.

As alluded to earlier, the DUNE simulation software is simplistic and does not simulate any ionisations within the region of the APA planes; in the case of APA-crossing muons this results in no hits being created after the track passes through the first induction wires. Evidently, this is an important region and must be understood and well simulated in order to test reconstruction and analyses. When this is added to the software, the 35 ton data will be essential for validation purposes.

7.4.2.2 Event Displays of APA-Crossing Tracks

The effect investigated in Section 7.4.2.1 is directly observable in the raw data, as shown in Figure 7.40. The electrons ionised as the particle track passes between the collection

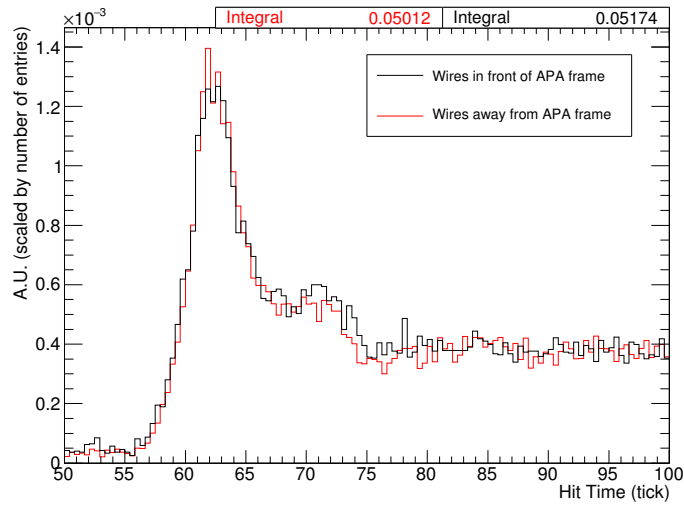
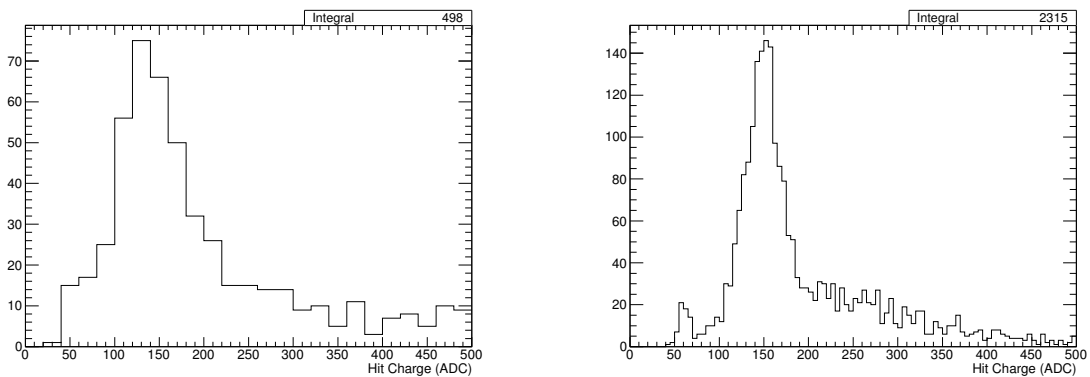


Fig. 7.38 Comparison between the distribution of T0-corrected hit times for hits on wires in front of the APA frame and away from the APA frame to validate the functionality of the mesh. Both distributions are normalised by the number of entries. There is no evidence of any differences between the two distributions so this suggests the mesh is working as intended.



(a) Hits occurring around the interaction time; $50 < \text{tick} < 70$. A fitted Gaussian of the peak yields a mean of 149 and width of 49.

(b) Hits occurring away from the interaction time; $\text{tick} < 50, \text{tick} > 70$. A fitted Gaussian of the peak yields a mean of 152 and a width of 28.

Fig. 7.39 Average lifetime-corrected charge per hit for hits on an APA-crossing track separated according to whether or not the hit was collected around the interaction time. There is no evidence to suggest the ‘extra’ hits collected around the interaction time have significantly more or less average charge than ‘regular’ hits.

plane and the mesh are observable as hits which appear to have drifted in the negative time direction. The outcome is a little ‘hook’ shape in the data.

7.4.3 Comparing Drift Regions with APA-Crossing Tracks

APA-crossing tracks may be utilised to make unique, specific measurements of the detector made possible since they originate from the same particle. For example, any drift velocity differences between the drift regions may be observed and the noise levels on the collection readouts on either side of the APA can be studied and compared.

The drift velocity is given by the angle of the track in wire/time space and any difference between this velocity in the two drift regions would be noticeable in a refraction-like effect. This is demonstrated in Figure 7.41a. A measure of the angle between the track segments in the different regions would therefore be a measure of the change in drift velocity; this is shown in Figure 7.41b.

The relative noise on the two collection planes can be evaluated by considering the number of hits present in the counter shadow, in each drift region, which were not reconstructed as part of the track associated with the triggering particle. The difference between each collection plane for a given event should peak at zero if similar levels of noise were observed in each drift region; this is confirmed in Figure 7.42.

7.5 Shower Reconstruction in 35 ton Data

The developments to the reconstruction in LArSoft, discussed in Chapter 5, were originally motivated by an interest in reconstructing and analysing π^0 mesons in the 35 ton data. Given the unfortunate eventual problems prevalent in the data, such analyses would be extremely challenging and likely impossible. Since it is still interesting and instructive to analyse how well the reconstruction performs on a sample of real data, this will be briefly explored in the present section.

Considerations relevant when applying the reconstruction developed on simulation to data are discussed in Section 7.5.1 before the necessary reanalysis of the calorimetry is presented in Section 7.5.2. The algorithms are applied to a shower and a π^0 candidate found in the data in Sections 7.5.3 and 7.5.4 respectively.

7.5.1 Data Specific Reconstruction

The BlurredCluster and EMShower algorithms, outlined in Sections 5.4.2 and 5.4.3 respectively, were applied to the data in an attempt to reconstruct particle objects. In general, the

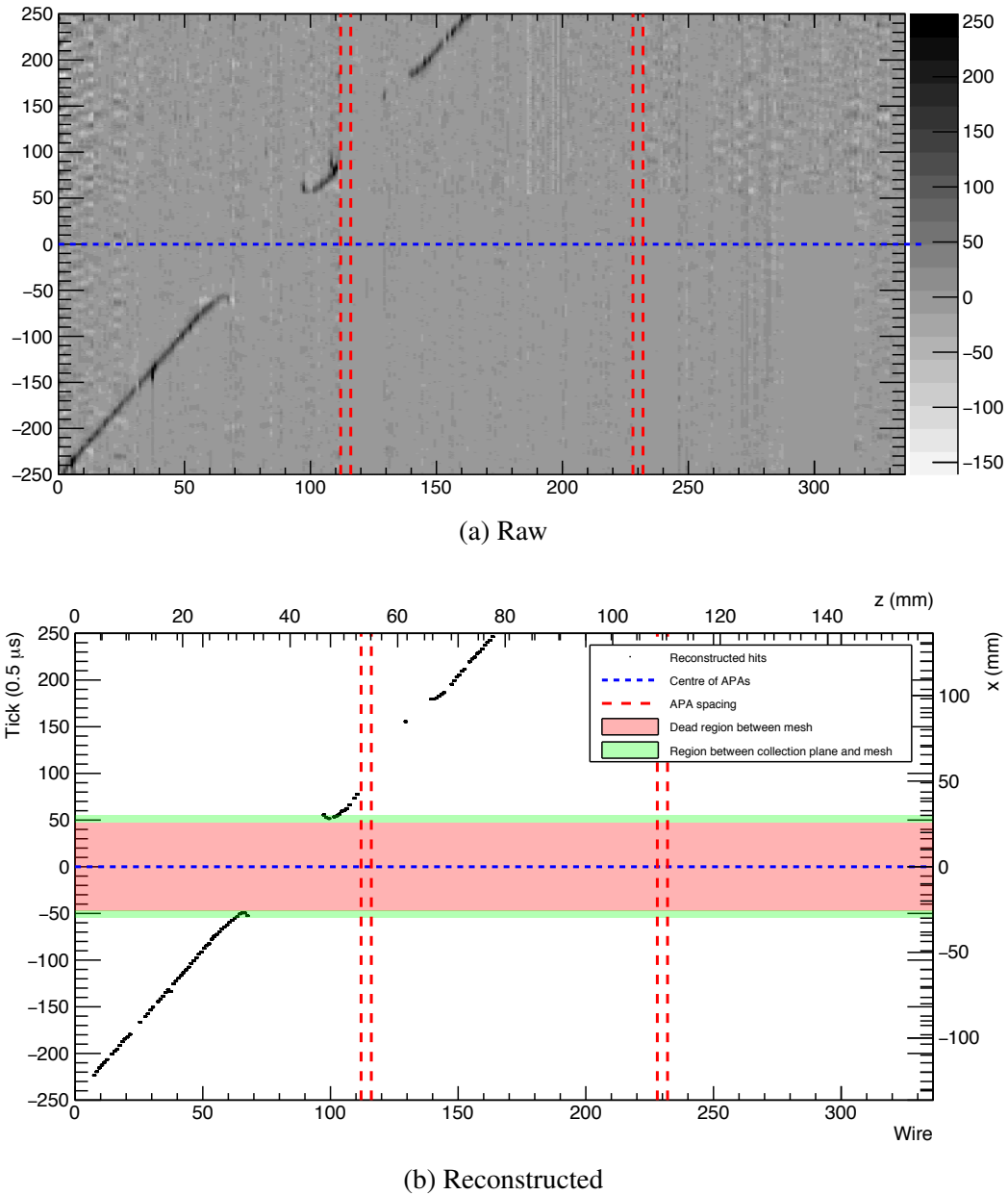
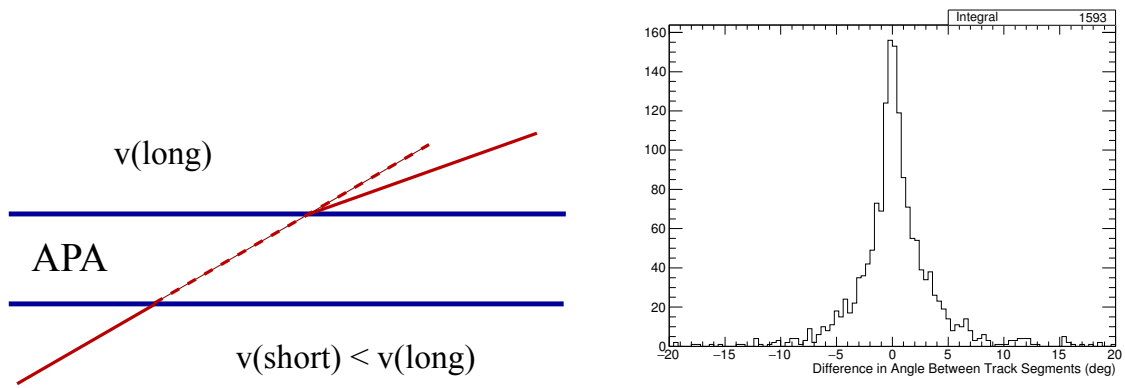


Fig. 7.40 Event display of an APA-crossing track with the charge deposited as it passes through the APAs evident. Figure 7.40a shows the raw charge and Figure 7.40b shows the reconstructed hits. The ‘hook’-like effect is visible, with hits at apparently negative drift time. The cm scale on Figure 7.40b is provided as a guide and is not completely correct due to the differing fields.



(a) Demonstration of how differing drift velocities between the drift regions would manifest in the data. A refraction-like effect would result in an angle between the two track segments.

(b) The angle between the track segments on either side of the APAs. The distribution peaks around zero, implying, as expected, the drift velocity is constant in both regions.

Fig. 7.41 Using APA-crossing tracks to confirm the drift velocity is consistent between the two drift regions.

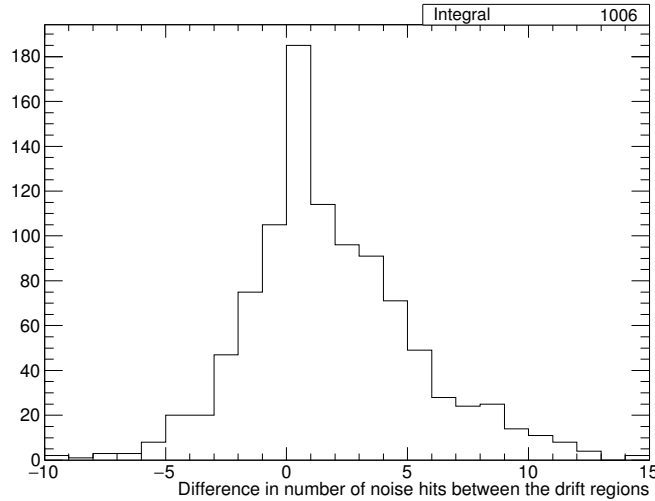


Fig. 7.42 Comparison of noise levels between the two drift regions using APA-crossing tracks. The number of noise hits in the counter shadow for each drift region was considered separately by neglecting all hits identified as track hits, all hits on noisy wires and all hits which have a large number of closely neighbouring hits (which could be symptomatic of unrelated particle tracks). The difference between the number of noise hits in each peaks around zero, implying similar levels of noise.

algorithms worked out the box and required no tuning. Since this requires real 3D reconstruction, as opposed to the subtle techniques developed to circumvent the issues with the induction planes (described in Section 7.1.3), the use of more than just the collection plane is necessitated. Reconstruction is therefore only possible for showers with large enough signals on induction planes, following the coherent noise removal, and following hit disambiguation.

As showering particles are unlikely to be associated with through-going muons, an unassociated method for obtaining the interaction time is required. In general, the photon detectors are designed for this purpose so the use of these seems natural.

Since it is highly unlikely the electronics models and detector responses used in the simulation are perfectly accurate, applying the calorimetric reconstruction to the data without modification would be inappropriate. The relevant calorimetric constants and functions must be determined from the data; this is essential for complete reconstruction and is discussed in Section 7.5.2.

7.5.2 Calorimetry Reconstruction

There are two relevant calorimetric conversions which are pertinent to shower reconstruction (both previously discussed in Section 5.3): the calorimetry constant and the shower energy conversion. The methods used to determine these for data will be discussed in this section.

It should be stressed that due to the large noise levels, accurate calorimetry will not be possible in the 35 ton data. This may be understood by considering the distribution of charge deposited by ionising particles; typically this is sampled from a Landau distribution with a most probable value dependent on the electron drift distance (due to lifetime effects). Since hit reconstruction tends to put cut on the hit ‘threshold’, the height of the peak above pedestal, this compromises lower energy hits populating the full charge distribution and biases the reconstruction toward higher energies. This is demonstrated in Figure 7.43. As far as possible, steps to mitigate these effects have been applied in the proceeding discussion. There will however be an inevitable bias so the following should not be treated as a full, rigorous assessment.

Calorimetric reconstruction is only attempted for the collection planes where the effects of noise are mitigated somewhat compared to the induction views. Since the data used were taken at a drift field of 250 V/cm (half the nominal voltage), the recombination factor used must take this into account. At 500 V/cm the value is 0.63 whilst at 250 V/cm a factor of 0.52 is used.

The procedure invoked to determine the calorimetry constant is largely identical to that used in simulation: the dE/dx of a through-going MIP is calculated and the constant varied until the expected distribution is obtained. The through-going muons used in the analyses

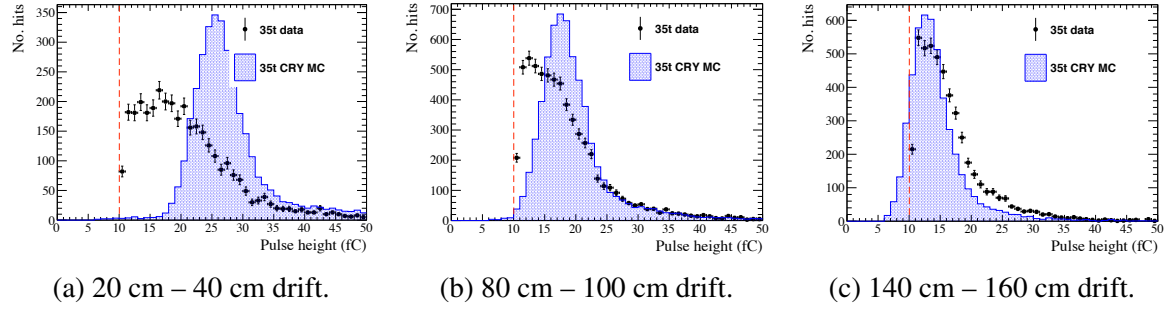


Fig. 7.43 The bias in the hit selection due to a high noise level in the 35 ton data. The charge distribution for through-going muons is shown for three different displacements along the drift direction, $20 \text{ cm} < x < 40 \text{ cm}$, $80 \text{ cm} < x < 100 \text{ cm}$ and $140 \text{ cm} < x < 160 \text{ cm}$. The red line represents a typical hit finding threshold. The most probable value of the distribution is close to this boundary in each of the cases, resulting in the lower charge hits being missed. This introduces a bias towards higher charge and has implications for the reliability of calorimetry in the 35 ton data sample.

described in Sections 7.4 and 7.3 were utilised to make these measurements. Additional necessary information, such as the interaction time (to correct the charge for lifetime) and the track angle (to correct the dE/dx for track pitch), is provided by the counters. In order to produce reliable results, an additional cut requiring at least 20 consecutive wires with a single hit on each was applied, with the dE/dx measurement obtained using just these hits. The eventual dE/dx distribution is demonstrated in Figure 7.44 and implies a calorimetry constant of 7.4×10^{-3} (for comparison, the value used for the collection plane in simulation is 5.4×10^{-3}).

In simulation, truth information was used to find a general charge to energy conversion used in, for example, the determination of total shower energy. This obviously is not possible in data so a similar technique to the calculation of the calorimetry constant described above was used. The lifetime-corrected charge and track pitch information can be utilised to find a value of dQ/dx (ADC/cm), which may then be converted into a measure of dE/dx (MeV/cm) using the calorimetry constant previously determined. This may in turn be used to find the total deposited energy by taking into account the distance travelled by the associated track in the collection view. As demonstrated in Figure ??, there exists a linear relationship between total deposited lifetime-corrected charge and the particle energy; this is also seen in data in Figure 7.45. This may then be used as a conversion in shower energy reconstruction.

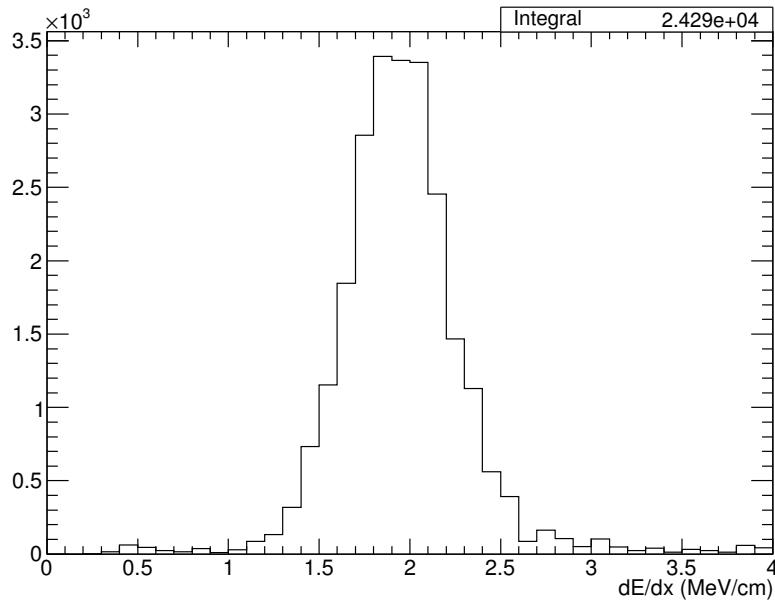


Fig. 7.44 The dE/dx distribution for MIPs passing through the 35 ton TPC. The calorimetry constant is chosen to ensure the peak of the distribution, which ideally follows a Landau, is around 1.8-1.9 MeV/cm.

7.5.3 Shower Reconstruction

Using the modifications discussed in Sections 7.5.1 and 7.5.2, the performance of the showering reconstruction on real data can be assessed by applying it to an electromagnetic shower. The result of applying the algorithms to the famous 35 ton shower depicted in Figure ?? is shown in Figure 7.46. The calorimetric reconstruction yields a dE/dx of 1.1 MeV/cm and a total shower energy of 188 MeV. These results appear feasible and are consistent with an electron shower, for which one would expect a dE/dx peaked around 2.1 MeV/cm; 1.1 MeV/cm is not an unreasonable value in the tail of this distribution. Given the electron energy, it is likely to have been produced by Compton scattering.

The T0 for this particle was determined to be 4740 ticks from reconstructing flash information collected by the photon detectors – this makes this shower the only fully automated reconstructed particle object in the 35 ton dataset.

7.5.4 π^0 Reconstruction

An important calorimetric test of particle detectors involves demonstrating a reasonable reconstructed π^0 mass peak. It was for this reason that the shower reconstruction discussed in Chapter 5 was developed. An analysis of a π^0 candidate event is briefly considered here.

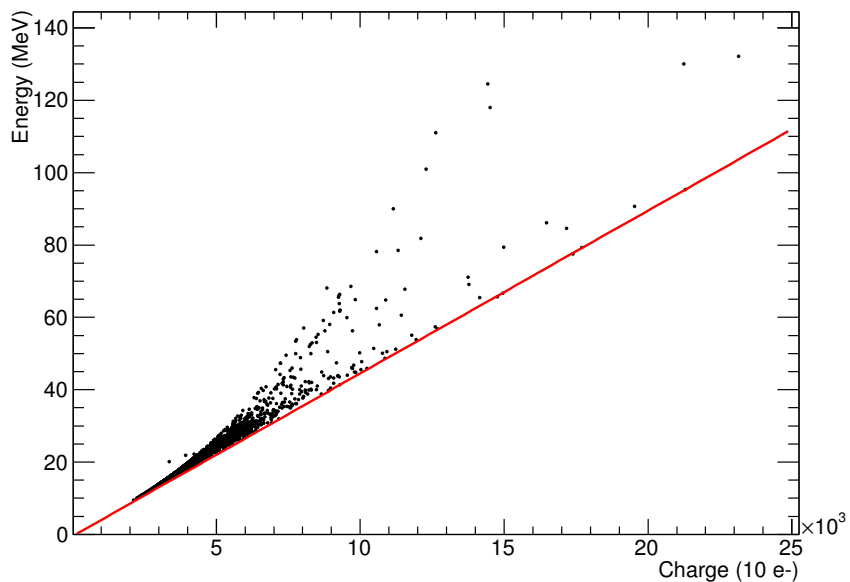


Fig. 7.45 Relationship between deposited charge and energy for 35 ton data, calculated using through-going MIPs. The lower edge of the distribution follows a linear pattern and it is this which the conversion is chosen to represent. Deviations from this linear fit observed above it are related to the fundamental issues with the 35 ton data and arise from missed charge due to the problems illustrated in Figure 7.43. This results in hits reconstructed with a lower charge for the implied energy deposited by the MIP. It should be noted there are no cases of extra charge deposited; this concurs with this interpretation and ensures confidence in the displayed line as the correct conversion may be assumed.

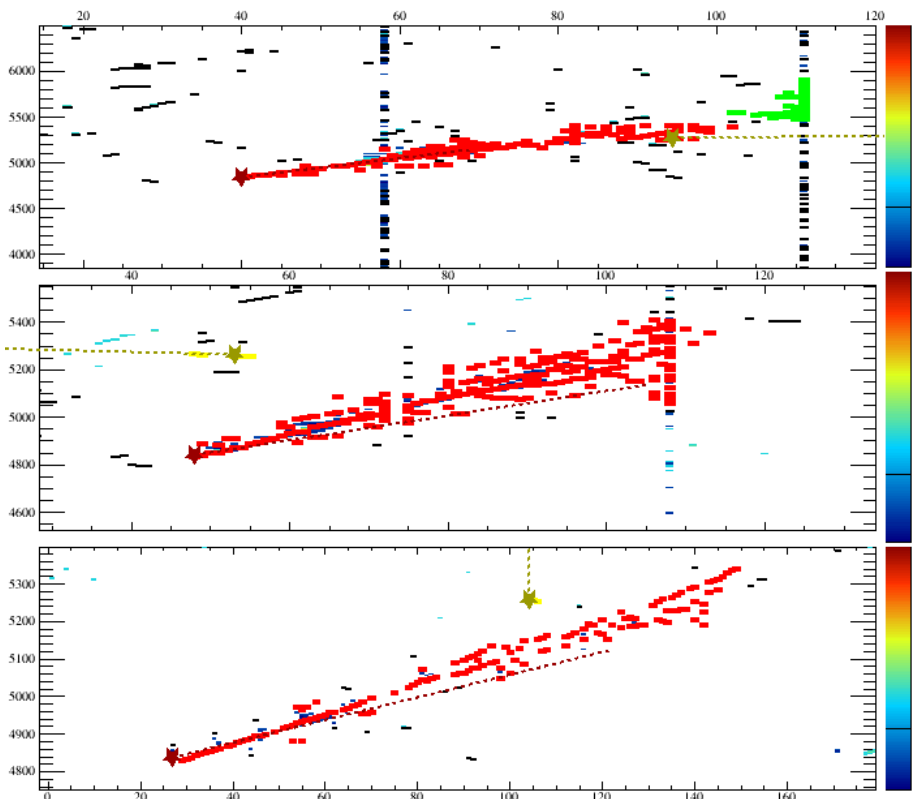


Fig. 7.46 Result of applying the shower reconstruction on a shower observed in the 35 ton data. Each small rectangle represents a reconstructed hit and the colour associated with each corresponds to a reconstructed shower object. The stars and dotted lines represent the reconstructed start point and direction for each shower.

Without full reconstruction and selection, identifying candidate events is very difficult. Such an event was observed in the online event display however and is shown in Figure 7.47. Unlike the shower discussed in Section 7.5.3, there is no associated photon detector informa-

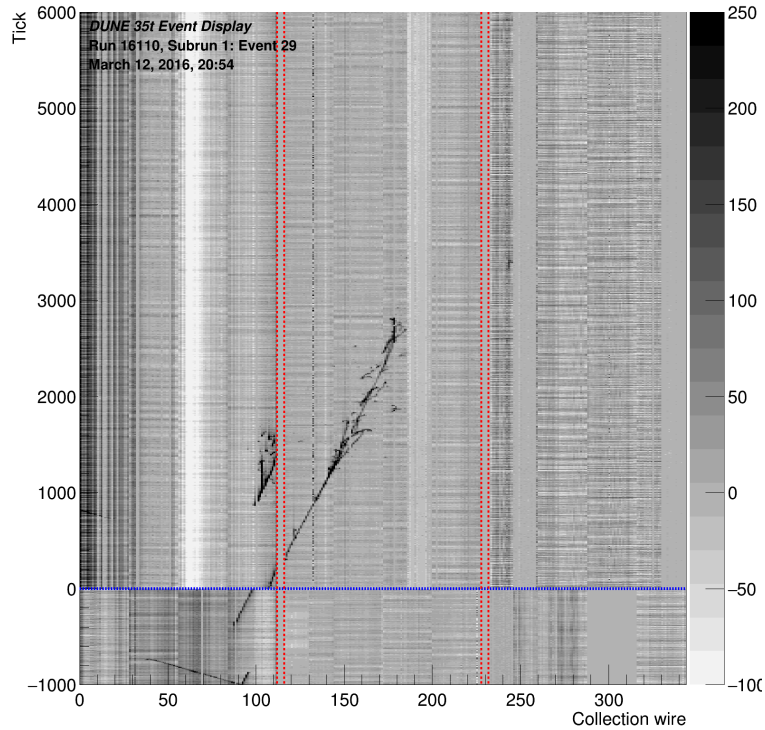


Fig. 7.47 A candidate π^0 event observed in the online event display during the run.

tion for this event; however, one of the candidate photons passes through the APA frames so techniques developed for the APA-crosser analysis (Section 7.4) may be employed to determine the relevant interaction time. Applying the calorimetry reconstruction, the dE/dx information associated with the high energy candidate photon (the one which crosses the APAs) gives a value of 4.75 MeV/cm, entirely consistent with the expectation for a photon of a distribution centred around 4.2 MeV/cm. The low energy candidate photon travels almost completely along the collection view direction resulting in unreliable dE/dx information. The total energy for each shower is determined to be 161.8 MeV and 500.5 MeV with an implied invariant mass of

$$m_{\pi^0?} = 156.6 \text{ MeV}, \quad (7.4)$$

comparable to the true π^0 mass of 140 MeV.

Without fully considering uncertainties and biases present, it is not possible to make a judgement as to the performance of the basic calorimetric reconstruction discussed in Section 7.5.2 or to confirm whether or not the event displayed in Figure 7.47 represents a π^0 decay. However, dE/dx values of 1.1 MeV/cm and 4.75 MeV/cm for different showers appear consistent with electron and photon particles respectively and, within the limits of the analysis presented here, it is believable the particle with invariant reconstructed mass of 156.6 MeV is indeed a π^0 .

7.6 35 ton Data Analysis Summary

Despite initial problems with the 35 ton good progress has been made in analyses, specifically focussing on understanding the detector. Techniques developed will be directly applicable to the data collected with the eventual far detector

References

- [1] Sheldon L Glashow. Partial-symmetries of weak interactions. *Nuclear Physics*, 22(4):579–588, 1961.
- [2] Steven Weinberg. A Model of Leptons. *Phys. Rev. Lett.*, 19(21):1264–1266, 1967.
- [3] G. Aad, et al. Observation of a new particle in the search for the Standard Model Higgs boson with the ATLAS detector at the LHC. *Physics Letters B*, 716(1):1–29, 2012.
- [4] S. Chatrchyan, et al. Observation of a new boson at a mass of 125 GeV with the CMS experiment at the LHC. *Physics Letters, Section B: Nuclear, Elementary Particle and High-Energy Physics*, 716(1):30–61, 2012.
- [5] Tara Shears. The Standard Model. *Phil. Trans. Roy. Soc. Lond.*, A370:805–817, 2012.
- [6] S M Bilenky. Neutrino in standard model and beyond. *Physics of Particles and Nuclei*, 46(4):475–496, 2015.
- [7] John Ellis. Outstanding questions: Physics beyond the Standard Model. *Phil. Trans. Roy. Soc. Lond.*, A370:818–830, 2012.
- [8] Y Fukuda, et al. Evidence for Oscillation of Atmospheric Neutrinos. *Phys. Rev. Lett.*, 81(8):1562–1567, 1998.
- [9] Q R Ahmad, et al. Direct Evidence for Neutrino Flavor Transformation from Neutral-Current Interactions in the Sudbury Neutrino Observatory. *Phys. Rev. Lett.*, 89(1):11301, 2002.
- [10] Wolfgang Pauli. Open letter to the participants of the conference in Tübingen, 1930.
- [11] E Fermi. Trends to a Theory of beta Radiation. (In Italian). *Nuovo Cim.*, 11:1–19, 1934.
- [12] E Fermi. Versuch einer Theorie der β -Strahlen. I. *Zeitschrift für Physik*, 88(3):161–177, 1934.
- [13] F. Wilson. Fermi’s Theory of Beta Decay. *American Journal of Physics*, 36(12):1150–1160, 1968.
- [14] G M Lewis. *Neutrinos*. Wykeham publications, London; Winchester, 1970.

- [15] C M G Lattes, et al. Processes Involving Charged Mesons. *Nature*, 159:694–697, 1947.
- [16] C M G Lattes, G P S Occhialini, and C F Powell. Observations on the Tracks of Slow Mesons in Photographic Emulsions. 1. *Nature*, 160:453–456,486–492, 1947.
- [17] R Brown, et al. Observations With Electron Sensitive Plates Exposed to Cosmic Radiation. *Nature*, 163:82, 1949.
- [18] C L Cowan, et al. Large Liquid Scintillation Detectors. *Phys. Rev.*, 90(3):493–494, 1953.
- [19] F. Reines and C. L. Cowan. A proposed experiment to detect the free neutrino, 1953.
- [20] F. Reines and C. L. Cowan. Detection of the free neutrino. *Physical Review*, 92(3):830–831, 1953.
- [21] C L Cowan, et al. Detection of the Free Neutrino: a Confirmation. *Science*, 124(3212):103–104, 1956.
- [22] Raymond Davis Jr. and Don S Harmer. Attempt to observe the $\text{Cl}^{37}(\bar{\nu}e^-)\text{Ar}^{37}$ reaction induced by reactor antineutrinos. *Bull. Am. Phys. Soc.*, 4:217, 1959.
- [23] G Danby, et al. Observation of High-Energy Neutrino Reactions and the Existence of Two Kinds of Neutrinos. *Phys. Rev. Lett.*, 9(1):36–44, 1962.
- [24] M. L. Perl, et al. Evidence for anomalous lepton production in e^+e^- annihilation. *Physical Review Letters*, 35(22):1489–1492, 1975.
- [25] G J Feldman, et al. Inclusive Anomalous Muon Production in e^+e^- Annihilation. *Phys. Rev. Lett.*, 38(3):117–120, 1977.
- [26] J Burmester, et al. Anomalous muon production in e^+e^- annihilations as evidence for heavy leptons. *Physics Letters B*, 68(3):297–300, 1977.
- [27] D. DeCamp, et al. Determination of the number of light neutrino species. *Physics Letters B*, 231(4):519–529, 1989.
- [28] B Adeva, et al. A determination of the properties of the neutral intermediate vector boson Z0. *Physics Letters B*, 231(4):509–518, 1989.
- [29] M Z Akrawy, et al. Measurement of the Z0 mass and width with the opal detector at LEP. *Physics Letters B*, 231(4):530–538, 1989.
- [30] P Aarnio, et al. Measurement of the mass and width of the Z0-particle from multi-hadronic final states produced in e^+e^- annihilations. *Physics Letters B*, 231(4):539–547, 1989.
- [31] S. Schael, et al. Precision electroweak measurements on the Z resonance. *Physics Reports*, 427(5-6):257–454, 2006.
- [32] K. Kodama, et al. Observation of tau neutrino interactions. *Physics Letters, Section B: Nuclear, Elementary Particle and High-Energy Physics*, 504(3):218–224, 2001.

- [33] H A Bethe. Energy Production in Stars. *Phys. Rev.*, 55(5):434–456, 1939.
- [34] John N Bahcall, Neta A Bahcall, and Giora Shaviv. Present Status of the Theoretical Predictions for the ^{37}Cl Solar-Neutrino Experiment. *Phys. Rev. Lett.*, 20(21):1209–1212, 1968.
- [35] John N. Bahcall, Aldo M. Serenelli, and Sarbani Basu. New Solar Opacities, Abundances, Helioseismology, and Neutrino Fluxes. *The Astrophysical Journal*, 621(1):L85–L88, 2005.
- [36] B. T. Cleveland, et al. Update on the measurement of the solar neutrino flux with the Homestake chlorine detector. *Nuclear Physics B (Proceedings Supplements)*, 38(1-3):47–53, 1995.
- [37] John N Bahcall, M H Pinsonneault, and G J Wasserburg. Solar models with helium and heavy-element diffusion. *Rev. Mod. Phys.*, 67(4):781–808, 1995.
- [38] J. N. Abdurashitov, et al. Results from SAGE (The Russian-American gallium solar neutrino experiment). *Physics Letters B*, 328(1-2):234–248, 1994.
- [39] P. Anselmann, et al. Solar neutrinos observed by GALLEX at Gran Sasso. *Physics Letters B*, 285(4):376–389, 1992.
- [40] W. Hampel, et al. GALLEX solar neutrino observations: Results for GALLEX IV. *Physics Letters, Section B: Nuclear, Elementary Particle and High-Energy Physics*, 447:127–133, 1999.
- [41] E. Gaisser, T. K.; Engel, R.; Resconi. *Cosmic Rays and Particle Physics*. Cambridge University Press, 1990.
- [42] T J Haines, et al. Calculation of Atmospheric Neutrino-Induced Backgrounds in a Nucleon-Decay Search. *Phys. Rev. Lett.*, 57(16):1986–1989, 1986.
- [43] K S Hirata, et al. Experimental study of the atmospheric neutrino flux. *Physics Letters B*, 205(2):416–420, 1988.
- [44] W Anthony Mann. Atmospheric neutrinos and the oscillations bonanza. *Int. J. Mod. Phys.*, A15S1:229–256, 2000.
- [45] B Pontecorvo. Neutrino Experiments and the Problem of Conservation of Leptonic Charge. *Sov. Phys. JETP*, 26:984–988, 1968.
- [46] V Gribov and B Pontecorvo. Neutrino astronomy and lepton charge. *Physics Letters B*, 28(7):493–496, 1969.
- [47] B Pontecorvo. Mesonium and anti-mesonium. *Sov. Phys. JETP*, 6:429, 1957.
- [48] D Casper, et al. Measurement of atmospheric neutrino composition with the IMB-3 detector. *Phys. Rev. Lett.*, 66(20):2561–2564, 1991.
- [49] R Becker-Szendy, et al. Electron- and muon-neutrino content of the atmospheric flux. *Phys. Rev. D*, 46(9):3720–3724, 1992.

- [50] Y Fukuda, et al. Atmospheric $\nu\mu/\nu e$ ratio in the multi-GeV energy range. *Physics Letters B*, 335(2):237–245, 1994.
- [51] J N Bahcall. Solar Models and Solar Neutrinos. *Physica Scripta*, 2005(T121):46, 2005.
- [52] Ziro Maki, Masami Nakagawa, and Shoichi Sakata. Remarks on the Unified Model of Elementary Particles. *Progress of Theoretical Physics*, 28(5):870, 1962.
- [53] John N Bahcall, Concepción M Gonzalez-Garcia, and Carlos Pena-Garay. Before and After: How has the SNO NC measurement changed things? *Journal of High Energy Physics*, 2002(07):54, 2002.
- [54] A Yu. Smirnov. The MSW effect and solar neutrinos. In *Neutrino telescopes. Proceedings, 10th International Workshop, Venice, Italy, March 11–14, 2003. Vol. 1+2*, pages 23–43, 2003.
- [55] L Wolfenstein. Neutrino oscillations in matter. *Phys. Rev. D*, 17(9):2369–2374, 1978.
- [56] S P Mikheev and A Yu. Smirnov. Resonance Amplification of Oscillations in Matter and Spectroscopy of Solar Neutrinos. *Sov. J. Nucl. Phys.*, 42:913–917, 1985.
- [57] S P Mikheev and A Yu. Smirnov. Resonant amplification of neutrino oscillations in matter and solar neutrino spectroscopy. *Nuovo Cim.*, C9:17–26, 1986.
- [58] K Eguchi, et al. First Results from KamLAND: Evidence for Reactor Antineutrino Disappearance. *Phys. Rev. Lett.*, 90(2):21802, 2003.
- [59] T Araki, et al. Measurement of Neutrino Oscillation with KamLAND: Evidence of Spectral Distortion. *Phys. Rev. Lett.*, 94(8):81801, 2005.
- [60] Abhijit Bandyopadhyay, et al. The Solar neutrino problem after the first results from KamLAND. *Phys. Lett.*, B559:121–130, 2003.
- [61] Pedro Cunha de Holanda and A Yu. Smirnov. LMA MSW solution of the solar neutrino problem and first KamLAND results. *JCAP*, 0302:1, 2003.
- [62] G L Fogli, et al. Evidence for Mikheyev-Smirnov-Wolfenstein effects in solar neutrino flavor transitions. *Phys. Lett.*, B583:149–156, 2004.
- [63] Thomas Mannel. Theory and Phenomenology of CP Violation. *Nuclear Physics B - Proceedings Supplements*, 167:115–119, 2007.
- [64] Tommy Ohlsson, He Zhang, and Shun Zhou. Radiative corrections to the leptonic Dirac CP-violating phase. *Phys. Rev. D*, 87(1):13012, 2013.
- [65] Tommy Ohlsson, He Zhang, and Shun Zhou. Probing the leptonic Dirac CP-violating phase in neutrino oscillation experiments. *Physical Review D - Particles, Fields, Gravitation and Cosmology*, 87(5):1–8, 2013.
- [66] DUNE Collaboration. Long-Baseline Neutrino Facility (LBNF) and Deep Underground Neutrino Experiment (DUNE): The LBNF and DUNE Projects. 1, 2016.

- [67] K Abe, et al. Physics potential of a long-baseline neutrino oscillation experiment using a J-PARC neutrino beam and Hyper-Kamiokande. *Progress of Theoretical and Experimental Physics*, 2015(5):053C02, 2015.
- [68] F Kaether, et al. Reanalysis of the Gallex solar neutrino flux and source experiments. *Physics Letters B*, 685(1):47–54, 2010.
- [69] J N Abdurashitov, et al. Measurement of the solar neutrino capture rate with gallium metal. III. Results for the 2002–2007 data-taking period. *Phys. Rev. C*, 80(1):15807, 2009.
- [70] B Aharmim, et al. Combined analysis of all three phases of solar neutrino data from the Sudbury Neutrino Observatory. *Phys. Rev. C*, 88(2):25501, 2013.
- [71] A Gando, et al. Reactor on-off antineutrino measurement with KamLAND. *Phys. Rev. D*, 88(3):33001, 2013.
- [72] R Wendell, et al. Atmospheric neutrino oscillation analysis with subleading effects in Super-Kamiokande I, II, and III. *Phys. Rev. D*, 81(9):92004, 2010.
- [73] M G Aartsen, et al. Determining neutrino oscillation parameters from atmospheric muon neutrino disappearance with three years of IceCube DeepCore data. *Phys. Rev. D*, 91(7):72004, 2015.
- [74] P Adamson, et al. Measurement of Neutrino and Antineutrino Oscillations Using Beam and Atmospheric Data in MINOS. *Phys. Rev. Lett.*, 110(25):251801, 2013.
- [75] P Adamson, et al. Electron Neutrino and Antineutrino Appearance in the Full MINOS Data Sample. *Phys. Rev. Lett.*, 110(17):171801, 2013.
- [76] K Abe, et al. Precise Measurement of the Neutrino Mixing Parameter θ_{23} from Muon Neutrino Disappearance in an Off-Axis Beam. *Phys. Rev. Lett.*, 112(18):181801, 2014.
- [77] P Adamson, et al. First measurement of muon-neutrino disappearance in NOvA. *Phys. Rev. D*, 93(5):51104, 2016.
- [78] M C Gonzalez-Garcia, Michele Maltoni, and Thomas Schwetz. Updated fit to three neutrino mixing: status of leptonic CP violation. *Journal of High Energy Physics*, 2014(11):52, 2014.
- [79] Ivan Esteban, et al. Updated fit to three neutrino mixing: exploring the accelerator-reactor complementarity. *Journal of High Energy Physics*, 2017(1):87, 2017.
- [80] F P An, et al. Observation of Electron-Antineutrino Disappearance at Daya Bay. *Phys. Rev. Lett.*, 108(17):171803, 2012.
- [81] J K Ahn, et al. Observation of Reactor Electron Antineutrinos Disappearance in the RENO Experiment. *Phys. Rev. Lett.*, 108(19):191802, 2012.
- [82] K Abe, et al. Observation of Electron Neutrino Appearance in a Muon Neutrino Beam. *Phys. Rev. Lett.*, 112(6):61802, 2014.

- [83] P Adamson, et al. First Measurement of Electron Neutrino Appearance in NOvA. *Phys. Rev. Lett.*, 116(15):151806, 2016.
- [84] K Abe, et al. Combined Analysis of Neutrino and Antineutrino Oscillations at T2K. *Phys. Rev. Lett.*, 118(15):151801, 2017.
- [85] V N Aseev, et al. Upper limit on the electron antineutrino mass from the Troitsk experiment. *Phys. Rev. D*, 84(11):112003, 2011.
- [86] Ch Kraus, et al. Final results from phase II of the Mainz neutrino mass search in tritium β -decay. *The European Physical Journal C - Particles and Fields*, 40(4):447–468, 2005.
- [87] Planck Collaboration, et al. Planck 2013 results. XVI. Cosmological parameters. *Astronomy & Astrophysics*, 571:A16, 2014.
- [88] DUNE Collaboration. Long-Baseline Neutrino Facility (LBNF) and Deep Underground Neutrino Experiment (DUNE): The Physics Program for DUNE at LBNF. 2, 2015.
- [89] DUNE Collaboration. Long-Baseline Neutrino Facility (LBNF) and Deep Underground Neutrino Experiment (DUNE): Long Baseline Neutrino Facility for DUNE. 3, 2016.
- [90] DUNE Collaboration. Long-Baseline Neutrino Facility (LBNF) and Deep Underground Neutrino Experiment (DUNE): The DUNE Detectors at LBNF. 4, 2016.
- [91] S. Amerio, et al. Design, construction and tests of the ICARUS T600 detector. *Nuclear Instruments and Methods in Physics Research, Section A: Accelerators, Spectrometers, Detectors and Associated Equipment*, 527(3):329–410, 2004.
- [92] C Anderson, et al. The ArgoNeuT detector in the NuMI low-energy beam line at Fermilab. *Journal of Instrumentation*, 7(10):P10019, 2012.
- [93] F Cavanna, et al. LArIAT: Liquid Argon In A Testbeam. 2014.
- [94] R Acciarri, et al. Design and construction of the MicroBooNE detector. *Journal of Instrumentation*, 12(02):P02017, 2017.
- [95] B Baller, et al. Liquid Argon Time Projection Chamber research and development in the United States. *Journal of Instrumentation*, 9(05):T05005, 2014.
- [96] David R Nygren. The Time Projection Chamber - A New 4pi Detector for Charged Particles. *eConf*, C740805(PEP-0144):58–78, 1974.
- [97] Carlo Rubbia. The Liquid Argon Time Projection Chamber: A New Concept For Neutrino Detectors.pdf, 1977.
- [98] Mitch Soderberg. The MicroBooNE Proposal, 2008.
- [99] V Chepel and H Araújo. Liquid noble gas detectors for low energy particle physics. *Journal of Instrumentation*, 8(04):R04001, 2013.

- [100] P. Derwent, et al. Proton Improvement Plan-II (PIP-II). Technical Report December, 2013.
- [101] Patrick Huber and Joachim Kopp. Two experiments for the price of one? The role of the second oscillation maximum in long baseline neutrino experiments. *Journal of High Energy Physics*, 2011(3):13, 2011.
- [102] LBNE Collaboration. Long-Baseline Neutrino Experiment (LBNE) Project: The LBNE Project. 1, 2012.
- [103] LBNE Collaboration. Long-Baseline Neutrino Experiment (LBNE) Project: Detectors At The Near Site. 3, 2012.
- [104] LBNE Collaboration. Long-Baseline Neutrino Experiment (LBNE) Project: Liquid Argon Detector At The Far Site. 4, 2012.
- [105] Margherita Buizza Avanzini. The LAGUNA-LBNO Project. *Physics Procedia*, 61:524–533, 2015.
- [106] HEPAP Subcommittee. Building for Discovery: Strategic Plan for U.S. Particle Physics in the Global Context. 2014.
- [107] T Kutter. Proposal for a Full-Scale Prototype Single-Phase Liquid Argon Time Projection Chamber and Detector Beam Test at CERN. Technical Report CERN-SPSC-2015-020. SPSC-P-351, CERN, Geneva, 2015.
- [108] I De Bonis and Others. LBNO-DEMO: Large-scale neutrino detector demonstrators for phased performance assessment in view of a long-baseline oscillation experiment. 2014.
- [109] CERN Courier. Neutrinos take centre stage.
- [110] Terry Tope, et al. Extreme argon purity in a large, non-evacuated cryostat. 1169(2014):1169–1175, 2014.
- [111] A. Curioni, et al. A regenerable filter for liquid argon purification. *Nuclear Instruments and Methods in Physics Research, Section A: Accelerators, Spectrometers, Detectors and Associated Equipment*, 605(3):306–311, 2009.
- [112] Alan Hahn, et al. The LBNE 35 Ton Prototype Cryostat. In *FERMILAB-CONF-14-420-PPD The*, 2014.
- [113] David Montanari, et al. First scientific application of the membrane cryostat technology. 1664(2014):1664–1671, 2014.
- [114] J. Freeman. Courtesy of John Freeman, Fermilab, 2014.